NASA CR-112147

Calspan

TECHNICAL REPORT

AN EXPERIMENTAL INVESTIGATION OF TURBULENT BOUNDARY LAYERS AT HIGH MACH NUMBER AND REYNOLDS NUMBERS

By: Michael S. Holden

CAL No. AB-5Ø72-A-1

Prepared for:

National Aeronautics and Space Administration
Langley Research Center
Langley Field, Virginia

FINAL REPORT
Contract No. NAS 1-11242
November 1972

CORNELL AERONAUTICAL LABORATORY, INC.
OF CORNELL UNIVERSITY, BUFFALO, N. Y. 14221

FOREWORD

This report was prepared for the National Aeronautics and Space Administration by Cornell Aeronautical Laboratory, Inc. (CAL), Buffalo, New York in partial fulfillment of Contract NAS 1-11242 "Experimental Investigation of Turbulent Boundary Layers at High Mach Numbers and Reynolds Numbers". The program was performed by the Aerodynamic Research Department of CAL under the sponsorship of the NASA Langley Research Center, Hampton, Virginia. Mr. Aubrey M. Cary, Jr. of NASA Langley was the technical monitor. This report is also being published as CAL Report No. AB-5072-A-1. The author would like to acknowledge the valuable discussions with Mr. Cary during the course of this program. The flat-plate model and instrumentation employed on this program was prepared and calibrated in conjunction with U.S. Air Force Contract F33615-70-C-1280. The performance period for this contract was 11/23/71 to 10/2/72.

ABSTRACT

Skin friction, heat transfer and pressure measurements were obtained in laminar, transitional and turbulent boundary layers on flat plates at Mach numbers from 7 to 13 at wall-to-free stream stagnation temperature ratios from 0.1 to 0.3. Measurements in laminar flows were in excellent agreement with the theory of Cheng. Correlations of the transition measurements with measurements on flight vehicles and in ballistic ranges show surprisingly good agreement. Our transition measurements do not correlate well with those of Pate and Schueler. Comparisons have been made between the skin friction and heat transfer measurements and the theories of VanDriest, Eckert and Spalding and Chi. These comparisons reveal in general that at the high end of our Mach number range (10-13) the theory of Van Driest is in best agreement with the data, whereas at lower Mach numbers (6.5-10) the Spalding Chi theory is in better agreement with the measurements. However, the relative agreement, between the theories and the data in the $F_c C_f$-$F_x R_{ex}$ plane is dependent upon the definition of the virtual origin of the turbulent boundary layer for the low Reynolds number high Mach number measurements.

TABLE OF CONTENTS

LIST OF ILLUSTRATIONS

LIST OF ILLUSTRATIONS (cont.)

NOMENCLATURE

a	-	Speed of sound
c	-	Specific heat $\frac{\text{ft lb}_f}{\text{slug}\,^\circ\text{F}}$
C_f	-	Local skin friction coefficient $\tau / \frac{1}{2} \rho_\infty u_\infty^2$
C_H	-	Stanton number $\dot{q} / \rho_\infty U_\infty (H_o - H_w)$
C_p	-	Pressure coefficient $p / \frac{1}{2} \rho_\infty u_\infty^2$
F_c	-	Compressibility transformation $\bar{C}_F / C_f$
F_x	-	Compressibility transformation $\bar{Re}_x / Re_x$
F_θ	-	Compressibility transformation $\bar{Re}_\theta / Re_\theta$
H	-	Total enthalpy
h	-	Static enthalpy $\frac{\text{ft lb}_f}{\text{slug}}$
M	-	Mach number
m	-	$(\frac{\gamma - 1}{2}) M^2$
P_r	-	Prandtl number
q_∞	-	Dynamic pressure (psia)
$\dot{q}$	-	Heat transfer rate BTU/ft^{2}sec.
Re_x	-	Reynolds number $(\frac{\rho u x}{\mu})$
T	-	Temperature (°R)
$T_{R,A}$	-	Reference temperatures
U	-	Velocity, ft/sec.
u'	-	Velocity fluctuation level ($u' = 0.02\, u_\infty$)
x	-	Distance along the surface of the flat plate
x_v	-	Distance from the virtual origin
γ	-	Specific heat ratio

δ - Boundary layer thickness

θ - Momentum thickness

λ - Turbulent macroscale $\simeq 8/10$

μ - Viscosity coefficient (slugs/ft sec)

ρ - Density slugs/ft^3

ν_{max} - Viscosity at point of maximum temperature in boundary layer

τ - Shear stress

Subscripts

o - Nozzle supply conditions

o' - Stagnation conditions behind a normal shock

1 - Initial driven gas condition

4 - Gas conditions behind reflected shock

i - Incident shock in driven gas

t_s - Test section initial conditions

w - Initial conditions at model surface

aw - Adiabatic wall conditions

∞ - Free stream or test section conditions

e - Local or edge conditions

v - Virtual origin

E - Eckert

SC - Spalding and Chi

VD - Van Driest

B - Beginning of transitions

E - End of transition

BE - Beginning to end of transition

I. INTRODUCTION

Methods of accurately predicting heat transfer and skin friction are a basic requirement in the design of vehicles, such as the space shuttle and the hypersonic transport, which are to be flown at hypersonic speeds. To maintain structural integrity for a sustained period of time at these speeds a vehicle would probably have to be cooled internally or by transpiration techniques. It is precisely in this hypersonic highly-cooled wall regime where the semi-empirical prediction methods are in question. There is a dearth of simultaneous measurements of both skin friction and heat transfer in turbulent boundary layers over highly cooled surfaces in high Reynolds number hypersonic airflows.

All the methods for predicting the skin friction and heat transfer to the surface beneath a turbulent boundary layer depend to some extent upon experimental measurement to determine semi-empirical constants contained in the formulation. Thus the accuracy of these methods depends both on the precision of the experimental measurements and the range of the basic parameter covered in the experiments. Recently, the theories of Spalding and Chi[1], Van Driest[2,3], Coles[4], and Sommers and Short[5] have been re-examined, with emphasis on their ability to predict skin friction and heat transfer to highly cooled surfaces in hypersonic flow. Whereas Bertram[6] and Cary[7] find best agreement between experimental measurements and the Spalding and Chi method, Hopkins and Inouye claim the "Van Driest II" theory is superior in predicting the properties of flat-plate turbulent boundary layers under highly cooled hypersonic conditions[8]. In part, the agreement, or lack of it, between theory and experiment results from the framework in which the experimental results have been evaluated and the assumptions made on the magnitude of the Reynolds analogy factor. This situation highlights the need for further detailed heat transfer and skin friction measurements in turbulent boundary layers over cooled surfaces in the hypersonic high Reynolds number regime.

In the experimental study described herein, heat transfer, skin friction and pressure measurements were made at Mach number from 7 to 13, Reynolds numbers from 6 to 180 x 10^6, and wall-to-freestream stagnation temperature ratios from 0.1 to 0.3. The test facilities, model and instrumentation together with details of the model configurations and freestream

conditions at which the measurements were made are described in the following section; the results of the experimental program are then presented. Comparisons between the measurements in laminar flow, the properties of transition and transitional flows, and the measurements in fully turbulent boundary layers are made with existing measurements and semi-empirical prediction methods. The conclusions from this study are then presented.

II. EXPERIMENTAL FACILITIES AND MEASUREMENT TECHNIQUES

2.1 Experimental Facilities

The experimental program was conducted in Cornell Aeronautical Laboratory's 48-inch and 96-inch Hypersonic Shock Tunnels.[9] The operation of these tunnels can be shown simply with the aid of the wave diagram shown in Fig. 1. The tunnel is started by rupturing a double diaphragm which permits the high-pressure air in the driver section to expand into the driven section, and in so doing generates a normal shock which propagates through the low-pressure air. A region of high-temperature, high-pressure air is produced between this normal shock front and the gas interface between the driver and driven gas, often referred to as the contact surface. When the primary or incident shock strikes the end of the driven section, it is reflected leaving a region of almost stationary high-pressure heated air. This air is then expanded through a nozzle to the desired freestream conditions in the test section.[9]

The duration of the flow in the test section is controlled by the interactions between the reflected shock, the interface, and the leading expansion wave generated by the nonstationary expansion process occurring in the driver section. The initial conditions of the gases in the driver and driven sections are controlled so that the gas interface becomes transparent to the reflected shock, as shown in Fig. 1 , thus there are no waves generated by interface-reflected shock interaction. This is known as operating under "Tailored-Interface" conditions. Under this condition, the test time is controlled by the time taken for the driver-driven interface to reach the throat, or the leading expansion wave to deplete the reservoir of pressure behind the reflected shock; the flow duration is said to be either driver-gas limited or expansion limited, respectively. Figure 2 shows the flow duration in the test section as a function of the Mach number of the incident shock. Here it can be seen that for operation at low M_i's, running times of over 25 milliseconds can be obtained with a long driver section. Measurements of heat transfer, skin friction and pressure were made on flat plate models at Mach numbers from 7 to 13; a complete list of the test conditions are given in Table I.

2.2 Model and Instrumentation

The flat-plate model used in this experimental program is shown in Fig. 3. The model, which was instrumented with heat transfer, skin friction and pressure gages, was equipped with two interchangeable leading-edge sections of 18 and 36 inches giving total model lengths of 39 and 52 inches, respectively. Heat transfer measurements were made on these two leading-edge segments to detect the position of transition as well as to provide information on the properties of the transitional regions. Both leading-edge sections had leading edges of less than 10^{-3} inches in thickness.

Skin Friction and Heat Transfer Instrumentation - A diagram of the skin friction transducer which we used in the present studies is shown in Fig. 4. The transducer[10] consists of a diaphragm which is supported flush with the model surface by two piezo-ceramic beams, which develop a charge when placed in bending by a surface shear on the diaphragm. A third beam is used to provide acceleration compensation; the beams are connected electrically to eliminate thermal, normal, and transverse pressure effects. An FET* impedance transform circuit is mounted internally to eliminate cable noise effects at low levels of skin friction. The gage, which has been refined and developed over the past 10 years, has been used to measure very low levels of skin friction encountered in separated regions in low Reynolds number hypersonic flow and more recently very high levels in regions of shock wave-turbulent boundary layer interactions in hypersonic flow. Because of the very severe heating conditions encountered in the latter studies, special care was taken to minimize the heat conduction through the flexures. The very large dynamic loads generated on the transducers during tunnel shutdown when run at the high dynamic pressure conditions used in our studies caused the diaphragms to be torn from the supporting beam. This problem was overcome by careful design of the flexure and by mounting the transducer in the seismic mass-rubber suspension system shown in Fig. 4.

Thin-film heat transfer gages were used in the present study. This technique is based on sensing the transient surface temperature of a nonconducting model by means of thin-film resistance thermometers. Because the thermal capacity of the gage is negligible, the instantaneous surface temperature of the backing material is related to the heat transfer rate by the

*Field Effects Transistor

classical semi-infinite slab theory.[9] Analog networks were used to convert the outputs of the gages, which are proportional to surface temperature, to a voltage directly proportional to heat transfer. The gages are fabricated on either small pyrex buttons or contoured inserts and mounted flush with the model surface.

Surface Pressure Measurements - We employed two types of surface pressure transducers in our earlier studies of shock wave-turbulent boundary layer interaction. The CAL-designed and constructed lead zirconium titanate piezoelectric pressure transducers[11] were used to obtain essentially the mean pressure distribution through the interaction region, though the transducer and orifice combination could follow fluctuations up to 15 kHz. A second flush-mounted transducer, especially designed for high frequency measurements by PCB in Buffalo, was used to obtain surface pressure fluctuation measurements from 200 Hz to 120 kHz. To prevent a resonance, a special mounting system was developed (as shown in Fig. 5) to lock the gage firmly into the model. A thin insulating barrier of aluminized mylar was attached to the diaphragm of the transducer to prevent thermal heating effects.

Gage Locations - The distance of each piece of instrumentation from the leading edge of the flat plate is given in Table II. Runs 1 through 11 were conducted with model configuration A while runs 12 through 19 were conducted with the model in configuration B.

2.3 Data Recording and Processing

The outputs from the transducers were recorded on a NAVCOR magnetic drum system and on a high frequency FM tape recorder, and also monitored on oscilloscopes. The NAVCOR system, which holds 48 channels in digital form, is essentially a low frequency system, whereas the 18 channel AMPEX FM recorder had a range of 0 to 1 MHz and was used to record the fluctuation data. The fluctuation measurements were recorded in analog form and subsequently processed by an analog-to-digital conversion/data storage system and digital computer program using a fast Fourier transform to yield the statistical properties of these measurements.

III. DISCUSSION OF EXPERIMENTAL MEASUREMENTS AND COMPARISON WITH PREDICTION METHODS

For each of the free stream conditions listed in Table I, the heat transfer, skin friction and pressure which were obtained on the flat-plate model are listed in Table III. In each case definitive measurements were made in the laminar, transitional and fully turbulent regions on the flat plate. A typical set of such measurements is shown in Fig. 6 . Figure 7d shows the particular schlieren photograph which corresponds to these measurements. Well-defined regions of laminar flow were observed upstream of transition and a correlation of the heat transfer measurements made in these regions is shown in Figure 8. Here we have compared the measurements with Cheng's theory including the effects (small) of boundary layer displacement. In its simplified form Cheng's theory gives

$$M^3 C_H = 0.332\, \bar{\chi} \left(\frac{1 + \beta \bar{\chi}}{\sqrt{1 + 2\beta \bar{\chi}}} \right)$$

where $$\beta = \frac{\gamma(\gamma-1)}{2} \left[\frac{T_w}{T_o} A(P_r) + 2B(P_r) \right]$$

and $$\bar{\chi} = M^3 \sqrt{\frac{C}{Re_\chi}} ,$$

C is Chapman-Rubesin constant and A = 0.968, B = 0.145. The measurements correlate well when plotted in this framework and are in good agreement with Cheng's zeroth to order theory.

3.1 Transition Correlation

Downstream of the region of laminar heating, transition was first indicated by a series of spikes in the heat transfer traces. These sharp increases in heating may be associated with turbulent bursts created at the edge of the viscous sublayer. This observation is supported by the records from adjacent gages which indicated that the disturbance responsible for the temporally increased heating was convected downstream at a fraction of the free stream velocity. At a short distance downstream of where the "spikes" were first

observed, the output of the gages exhibited strong fluctuations and the mean heating and skin friction level increased above that for laminar flow. In this region the outputs from the high frequency pressure transducers showed fluctuation levels considerably in excess of the levels subsequently observed downstream of transition. The heat transfer rises monotonically through the transition region to reach a maximum near the end of transition, decaying with downstream distance beyond this point to approach the one fifth power law at approximately 115% of the Reynolds number for maximum heating. These studies and earlier measurements on flat plates and cones have indicated that the beginning of the transition process occurs at approximately one half of the distance to the point of maximum heating, as indicated in Fig. 9 where we have plotted the ratio of the local Reynolds number based on the beginning and end of transition versus Mach number. The beginning of transition was defined in these studies as the point of departure of the heat transfer from the laminar value.

No satisfactory method has been found to correlate measurements of the position of transition made in the present studies. Because of the high Reynolds numbers and Mach numbers at which these tests were conducted, and the large scale of the tunnels involved, the radiated noise from the tunnel wall boundary layer was probably considerably smaller than in the studies of Pate and Schueler.[12] The latter study indicated that decreasing the size of the tunnel, for the same free stream conditions, should decrease the transition Reynolds number. The transition measurements shown in Fig. 10, made in the A and D nozzles, which have exit diameters of 24 and 48 inches respectively, do not exhibit this scale effect, even though a unit Reynolds number variation is evident in the correlation. Plotted in terms of Pate and Schueler's parameters, in Fig. 11, the data falls below their correlation. For agreement, our transition Reynolds numbers would have to have been over 200 million. In Fig. 12 we have compared our transition measurements on the flat plates with measurements on flight vehicles and in the ballistic range. The agreement between these measurements is surprisingly good. It is clear that in these tests the position of transition was influenced by factors which were different, and or more complex than those governing transition in the tests conducted by Pate and Schueler. Whether the fluctuating pressure level of the free stream is the main factor influencing transition, as indicated by the measurements of Stainback, Fischer and Wagner,[13] or whether this quantity merely follows more subtile parameters remains to be determined.

Looking at transition from another aspect, we can examine the lowest Reynolds number based on the turbulent macroscale at which fully turbulent flow can exist. Following a similar reasoning to that used by Bradshaw[14] in discussing transition reversal we can say a self-sustaining turbulent boundary layer can exist only when the energy or shear stress producing eddy size and dissipating range of eddy size just overlap, or where a viscosity independent region can be established. This criterion can be expressed as Re_λ = constant where $Re_\lambda = \left(\frac{u'\lambda}{\mu_{MAX}}\right)$ and where Bradshaw[14] and Finson[15] suggest that the constant is approximately 30. For a hypersonic turbulent flat plate boundary layer the measurements of Demetriades[16] indicate that $u' = 0.02\, u_\infty$, $\lambda = \frac{\delta}{10}$ Then evaluating μ_{MAX} at the edge of the sublayer for turbulent boundary layers with momentum thicknesses equal to those at the beginning and end of transition (see later) where θ and δ are related through Fig. 13 we obtain the correlation shown in Fig. 14. Here we see that for our measurements transition is complete for Re_λ's of approximately 50, with transition beginning at Reynolds numbers of approximately one half this value. These correlations suggest the hypersonic boundary layer will remain fully turbulent only after a certain Reynolds number based on a turbulent macroscale is exceeded. This idea is supported by experimental studies conducted at CAL and Langley[17] where attempts have been made to cause premature transition in flows above Mach 8. Although roughness was found to disturb the structure of the laminar boundary layer, causing an increase in the local skin friction and heat transfer, the Reynolds number (based on distance to the end of transition) at which the boundary layer exhibited the characteristics of a fully developed turbulent boundary layer was only slightly less than if "natural transition" had been allowed to occur. Our studies indicate that Re_λ must be in excess of 50 for a fully developed turbulent flow to be maintained at hypersonic speeds.

3.2 Comparisions of Heat and Skin Friction Measurements with Turbulent Theories

To make a comparison between the measurements beneath the turbulent portion of the boundary layer and the theories of Eckert, Van Driest, and Spalding and Chi, it is necessary to calculate the momentum thickness. In Figs. 15 and 16 the measured Reynolds analogy factor ($2St/C_f$) is shown for both transition and turbulent flows and from this correlation we have concluded

that $2\,St/C_f = 1$ best represents the measurements on hypersonic highly-cooled flows. We have calculated the momentum thickness from the heat transfer distribution using the relationship $\theta = \int_o^x C_H \, d x'$.

We have chosen to perform the comparison between the measurments and the three theories within the framework of the Spalding-Chi method, where the local skin friction coefficient C_f is related to the skin friction coefficient in an equivalent incompressible flow C_{f_i} through the relationship

$$C_{f_i} = F_c \, (M_e, \, T_w / T_o) \, C_f$$

and the local Reynolds number based on momentum thickness θ or distance from a virtual origin x_v. R_{e_θ} and R_{e_x} respectively are related to the equivalent quantities through the relationships

$$R_{e_{\theta_i}} = F_\theta \, R_{e_\theta}$$

and

$$R_{e_{x_i}} = F_x \, R_{e_x}$$

We have assumed that the Karman-Schoenherr relationship

$$\log_{10} (R_{e_{x_i}} C_{F_i}) = \log_{10} (2 R_{e_\theta}) = 0.242 \, (C_{F_i})^{-1/2}$$

where the average skin friction C_{F_i} is related to the local skin friction C_{f_i} by

$$C_{f_i} = 0.242 \, C_{F_i} \left[0.242 + 0.8686 \, (C_{F_i})^{1/2} \right]^{-1}$$

accurately describes the skin friction distribution in the incompressible plane.

In Spalding-Chi analysis the transformation factors F_c, F_θ and F_x were determined from Van Driest's analysis and correlations of experimental measurements. For this analysis the transformation factors are

$$(F_c)_{sc} = r \, m_e \, (\sin^{-1}\alpha + \sin^{-1}\beta)^{-2}$$

$$(F_\theta)_{sc} = (T_w / T_e)^{-0.702} \, (T_w / T_{Aw})^{-0.772}$$

and $$F_x = F_\theta \, F_c^{-1}$$

where $$\alpha = (2A^2 - B)(4A^2 + B^2)^{-1/2} \text{ and } \beta = B (4A^2 + B^2)^{-1/2}$$

and $$A = \left[r \, m_e \left(\frac{T_w}{T_e} \right)^{-1} \right]^{1/2} \quad \text{and} \quad B = \left(1 + r \, m_e - \frac{T_w}{T_e} \right) \left(\frac{T_w}{T_e} \right)^{-1}$$

where a recovery factor (r) of 0.89 was used.

The Van Driest analysis used Prandtl-Karman mixing length theory to describe the compressible turbulent boundary layer over a flat plate. The transformation factors which can be derived from this analysis are

$$(F_c)_{VD} = r\, m_e \left(\sin^{-1}\alpha + \sin^{-1}\beta\right)^2$$

$$(F_\theta)_{VD} = \mu_e / \mu_w$$

and

$$F_\chi = F_\theta\, F_c^{-1}$$

The function F_c is identical in the Van Driest and Spalding-Chi analyses.

From Eckert's reference enthalpy method we can deduce the transformation factors

$$(F_c)_E = T^* / T_e$$

$$(F_\theta)_E = \mu_e / \mu^*$$

and

$$F_\chi = F_\theta\, F_c^{-1}$$

where we have evaluated these expressions for two definitions of the reference temperature T*

$$T_E^* = 0.5\, T_w + 0.22\, T_{AW} + 0.28\, T_e$$

$$T_A^* = 0.5\, T_w + 0.1667\, T_r + 0.333\, T_e$$

The viscosity for the transformations was calculated from the Sutherland relationship for temperature above 500°R with the Hirschfelder, Curtiss and Bird[19] values used below this temperature.

In order to compare the experimental measurements with the theories in the $F_c\ C_f - F_{R_x} Re_x$ plane it is necessary to define a virtual origin from which the turbulent boundary layer is assumed to grow. We assumed that the momentum thickness of the turbulent boundary layer at the end of transition (θ_v) was given by

(i) $$\theta_v = \int_0^{\chi_B} C_H\, d\chi + \int_{\chi_B}^{\chi_E} C_H\, d\chi \equiv \theta_B + \theta_{BE}$$

(ii) $$\theta_v = \theta_B + (\theta_{BE}/2)$$

(iii) $$\theta_v = \theta_B + \int_{\chi_B}^{\chi_E} C_{H_{LAM}}\, d\chi$$

(iv) $$\theta_v = \theta_B$$

The first assumption gives a comparison in the $F_c C_f - F_{R_x} R_{e_x}$ plane which is directly equivalent to the $F_c C_f - F_\theta R_{e_\theta}$ correlation. We make the second assumption for a direct comparison with the method for determining the virtual origin suggested by Bertram and Carry to be discussed later. The third and fourth assumptions are based on pragmatic situations where no measurements exist of transitional heating and the momentum thickness is calculated by assuming the boundary layer is laminar to the end and beginning of transition respectively. In all cases the distance from the virtual origin to the end of transition was calculated using the respective theories of each of assumption for momentum thickness. Finally we have used the method suggested by Bertram and Carry who based on the best correlation of their data with the Spalding-Chi theory place the virtual origin at the point where $R_{e_\theta} = R_{\theta_B} + \left(\frac{R_{\theta_{BE}}}{2}\right)$

Comparison between the three prediction methods and the heat transfer and skin friction measurements in the $F_e C_f - F_x R_{e_x}$ framework are contained in Figs. 19 through 26. Using our first assumption ($\theta_v = \theta_B + \theta_{BE}$) we obtain equivalent correlations on the $F_x R_{e_x}$ plane (Figs. 19 and 20) to the $F_\theta R_{e_\theta}$ described in the previous two figures. We again observe that Van Driest theory is in closer agreement with the measurements than the Spalding-Chi analysis which consistently underpredicts the heat transfer and skin friction. With decreasing θ_v the agreement between the measurements and the Spalding-Chi theory improved however even for $\theta_v = \theta_B$ Spalding-Chi under predicts the measurements at the highest Mach numbers whereas causing the Van Driest method to underpredict in this region. Employing Bertram and Carry's approach to calculating the virtual origin we obtain good agreement between the measurements and the Spalding-Chi method for Mach numbers below 10. This approach underpredicts the measurements above Mach 10. Van Driest's theory overpredicts the measurement below Mach 10 using the later method for specifying the virtual origin.

IV. SUMMARY AND CONCLUSIONS

Heat transfer, skin friction and pressure measurements have been obtained in laminar, transitional and turbulent boundary layers over flat plate models at Mach numbers from 7 to 13, Reynolds numbers from 6×10^6 to 200×10^6 and wall-to-free stream stagnation temperature ratios from 0.1 to 0.3. The measurements of heat transfer beneath the laminar boundary layers were in good agreement with the zeroth order theory of Cheng. Transition was first observed as "spikes" in the heat transfer records; and records from adjacent gages suggest that these "spikes" result from turbulent bursts which grow in size as they accelerate downstream. Surprisingly, our measurements of the Reynolds number based on momentum thickness at transition were in good agreement with results from ballistic and down range tests. These measurements did not correlate within the framework of Pate and Schueler's studies which suggest that in these high Mach numbers, high Reynolds number flows, noise radiated from the tunnel walls is not the dominant factor influencing transition. It was found that the end of transition did not occur (or a turbulent boundary layer could not be supported) until the eddy Reynolds number $R_{e_\lambda} = \frac{u'\lambda}{\nu_{MAX}}$ exceeded a value of 50; and, in fact, the end of transition was correlated well with $R_{e_\lambda} = 50$. The beginning of transition occurred at approximately one half this value, and, in fact, the transition region had approximately the same length as the laminar run.

The Reynolds analogy factor was found to be close to unity in the turbulent and transitional boundary layers we studied and this value has been used in the data reduction and correlation. Plotted in the $F_c C_f - F_\theta R_{e_\theta}$ plane, the skin friction and heat transfer measurements were in best overall agreement with the theories of Van Driest and Eckert, though both of these theories tended to overpredict the levels in the Mach 7 to 10 range. Plotted in the $F_c C_f - F_x R_{e_x}$ plane we see the same general result whether the virtual origin is defined from the momentum defect at the beginning or end of transition. While the theory of Van Driest is in best overall agreement, it overpredicts the heat transfer and skin friction in the low hypersonic Mach number regime, where the agreement between the measurements and the Spalding-Chi theory is best. Because only

surface measurements were made, there remains a question on the magnitude of the distance downstream of the maximum heating point, where all the remnants of the transition process are dissipated. While this is unimportant in our studies at the lower Mach numbers, where we have measurements at many hundreds of boundary layer thicknesses downstream of the point of maximum heating, at Mach 11 and 13 one is forced to ask the question: Is the disagreement between the measurements and the Spalding-Chi theory results from the persistence of turbulent remnants in the flow a low Reynolds number effect or an inadequacy of the theory? Only boundary layer surveys will provide a complete answer on the relaxation distance of a transitional boundary layer from the maximum heating point to the point where the boundary layer is fully turbulent.

V. REFERENCES

1. Spalding, D.B. and Chi, S.W., The Drag of a Compressible Turbulent Boundary Layer on a Smooth Flat Plate with and without Heat Transfer, Journal of Fluid Mechanics, January 1964, pp. 117-143.

2. Van Driest, E.R., Turbulent Boundary Layer in Compressible Fluids, J. Aero. Sci., 1951, 18, No. 3, 145-160.

3. Van Driest, E.R., Problem of Aerodynamic Heating, Aeronautical Engineering Review, Vol. 15, No. 10, October 1956.

4. Coles, D.E., The Turbulent Boundary Layer in a Compressible Fluid, The Physics of Fluids, Vol. 7, No. 9, September 1964, pp. 1403-1423; also Report R-403-PR, 1962, Rand Corp.

5. Sommer, S.C. and Short, B.J., Free-Flight Measurements of Turbulent Boundary-Layer Skin Friction in the Presence of Severe Aerodynamic Heating at Mach Numbers from 2.8 to 7.0, TN 3391, 1955, NACA; also Journal of the Aeronautical Sciences, Vol. 23, No. 6, June 1956, pp. 536-542.

6. Bertram, M.H., Cary, A.M., Jr., and Whitehead, A.H., Jr., Experiments with Hypersonic Turbulent Boundary Layers on Flat Plates and Delta Wings, AGARD Specialists Meeting on Hypersonic Boundary Layers and Flow Fields, London, England, May 1-3, 1968.

7. Cary, A.M., Jr., Turbulent Boundary-Layer Heat Transfer and Transition Measurements for Cold-Wall Conditions at Mach 6, AIAA Journal, Vol. 6, No. 5, May 1968, pp. 958-959.

8. Hopkins, E.J. and Inouye, M., An Evaluation of Theories for Predicting Turbulent Skin Friction and Heat Transfer on Flat Plates at Supersonic and Hypersonic Mach Numbers, AIAA Journal, Vol. 9, No. 6, June 1971, pp. 993-1003.

9. "Description and Capabilities of the CAL 48-Inch Hypersonic Shock Tunnel," Cornell Aeronautical Laboratory, Inc., Buffalo, New York (April 1968).

10. MacArthur, R.C., Contoured Skin Friction Transducer, CAL Report No. AN-2403-Y-1 (August 1967).

11. Martin, J.F., Duryea, G.R., and Stevenson, L.M., Instrumentation for Force and Pressure Measurements in a Hypersonic Shock Tunnel, Advances in Hypervelocity Techniques, CAL Report No. 113 (Plenum Press 1962).

12. Pate, S.R., Schueler, C.J., An Investigation of Radiated Aerodynamic Noise Effects on Boundary-Layer Transition in Supersonic and Hypersonic Wind Tunnels, AIAA Paper 68-375, April 1968.

13. Stainback, P.C., Fischer, M.C. and Wagner, R.D., Effects of Wind Tunnel Disturbances on Hypersonic Boundary Layer Transition, AIAA Paper 72-181, January 1972.

14. Bradshaw, P., A Note on Reverse Transition, JFM (1969), Vol. 35, Part 2, pp. 387-390.

15. Finson, M., Private Communication

16. Demetriades, A. and Laderman, A.J., Measurements of the Mean and Turbulent Flow in a Cooled Wall Boundary Layer at Mach 9.37, AIAA Paper 72-73, January 1972.

17. Morrisette, E.L., Stone, D.R., and Cary, A.M., Downstream Effects of Boundary Layer Trips in Hypersonic Flow, Langley Syposium on Compressible Turbulent Boundary Layers, NASA SP 216, Dec. 1968.

18. Eckert, E.R.G., Engineering Relations for Friction and Heat Transfer to Surfaces in High Velocity Flow, J. Aeronautical Sciences, 1956, 23 (8), 585-587.

19. Hirschfelder, J.O.; Curtiss, C.F.; and Bird, R.B., Molecular Theory of Gases and Liquids, J. Wiley & Sons, 1954.

20. Cheng, H.K., Hall, J.G., Golian, T.C., and Hertzberg, A., Boundary Layer Displacement and Leading-Edge Bluntness Effects in High-Temperature Hypersonic Flow, J. Aero/Space Sci., Vol. 28, No. 5, pp. 353-381 (1961).

Table I TEST CONDITIONS

RUN NO.	5	6	7	8	9	10	11	12
ATTACK	0.0	0.0	0.0	0.0	0.0	0.0	0.0	0.0
YAW	0.0	0.0	0.0	0.0	0.0	0.0	0.0	0.0
ROLL	0.0	0.0	0.0	0.0	0.0	0.0	0.0	0.0
M(I)	3.725E 00	3.615E 00	3.325E 00	3.136E 00	3.279E 00	3.215E 00	3.586E 00	3.280E 00
P(0)	1.149E 04	2.060E 04	1.843E 04	7.759E 03	1.935E 04	1.460E 04	9.123E 03	1.968E 04
H(0)	2.149E 07	2.225E 07	1.783E 07	1.611E 07	1.740E 07	1.681E 07	2.068E 07	1.773E 07
T(0)	3.237E 03	3.368E 03	2.759E 03	2.509E 03	2.748E 03	2.649E 03	3.135E 03	2.796E 03
M	1.040E 01	1.204E 01	1.109E 01	1.053E 01	1.072E 01	1.057E 01	1.018E 01	1.073E 01
U	6.412E 03	6.562E 03	5.856E 03	5.555E 03	5.777E 03	5.676E 03	6.285E 03	5.833E 03
T	1.580E 02	1.236E 02	1.158E 02	1.157E 02	1.208E 02	1.198E 02	1.584E 02	1.229E 02
P	2.022E-01	1.469E-01	2.534E-01	1.369E-01	3.446E-01	2.673E-01	1.839E-01	3.456E-01
Q	1.533E 01	1.491E 01	2.186E 01	1.064E 01	2.774E 01	2.094E 01	1.336E 01	2.788E 01
RHO	1.074E-04	9.975E-05	1.836E-04	9.929E-05	2.394E-04	1.872E-04	9.741E-05	2.360E-04
MU	1.324E-07	1.039E-07	9.742E-08	9.729E-08	1.015E-07	1.008E-07	1.326E-07	1.033E-07
RE/FT.	5.202E 06	6.302E 06	1.104E 07	5.669E 06	1.362E 07	1.055E 07	4.616E 06	1.333E 07
PITOT	2.049E 01	2.773E 01	4.050E 01	1.968E 01	5.138E 01	3.877E 01	2.482E 01	5.165E 01
T0	9.736E 02	9.856E 02	8.504E 02	7.962E 02	8.388E 02	8.201E 02	9.531E 02	8.524E 02
RU0	5.883E-07	5.931E-07	5.367E-07	5.126E-07	5.316E-07	5.233E-07	5.799E-07	5.375E-07
SQRT.C0	8.494E-01	8.462E-01	8.663E-01	8.750E-01	8.682E-01	8.712E-01	8.524E-01	8.661E-01
H(W)	3.177E 06	3.171E 06	3.207E 06	3.189E 06	3.207E 06	3.201E 06	3.225E 06	3.237E 06
T(W)	5.290E 02	5.280E 02	5.340E 02	5.310E 02	5.340E 02	5.330E 02	5.370E 02	5.390E 02
P(TS)	3.868E-04	4.835E-04	7.736E-04	3.868E-04	3.868E-04	4.446E-04	4.642E-04	4.448E-04
RE(STAG)	4.586E 04	4.226E 04	7.730E 04	4.266E 04	1.005E 05	7.969E 04	4.139E 04	9.905E 04

RUN NO.	13	14	15	16	17	18	19
ATTACK	0.0	0.0	0.0	0.0	0.0	0.0	0.0
YAW	0.0	0.0	0.0	0.0	0.0	0.0	0.0
ROLL	0.0	0.0	0.0	0.0	0.0	0.0	0.0
M(I)	2.488E 00	3.668E 00	3.178E 00	2.594E 00	3.599E 00	2.547E 00	3.199E 00
P(0)	5.223E 03	1.433E 04	1.048E 04	1.838E 04	1.072E 04	1.315E 04	8.771E 03
H(0)	1.069E 07	2.073E 07	1.613E 07	1.147E 07	2.031E 07	1.127E 07	1.699E 07
T(0)	1.707E 03	3.151E 03	2.529E 03	1.899E 03	3.083E 03	1.850E 03	2.642E 03
M	7.970E 00	7.738E 00	7.982E 00	8.324E 00	7.367E 00	7.712E 00	7.441E 00
U	4.447E 03	6.178E 03	5.472E 03	4.627E 03	6.102E 03	4.561E 03	5.586E 03
T	1.296E 02	2.651E 02	1.954E 02	1.285E 02	2.853E 02	1.455E 02	2.344E 02
P	6.072E-01	1.816E 00	1.194E 00	2.088E 00	1.846E 00	2.203E 00	1.501E 00
Q	2.703E 01	7.620E 01	5.329E 01	1.014E 02	7.019E 01	9.180E 01	5.822E 01
RHO	3.937E-04	5.750E-04	5.126E-04	1.364E-03	5.429E-04	1.271E-03	5.374E-04
MU	1.087E-07	2.161E-07	1.625E-07	1.080E-07	2.308E-07	1.220E-07	1.929E-07
RE/FT.	1.610E 07	1.644E 07	1.726E 07	5.846E 07	1.435E 07	4.750E 07	1.556E 07
PITOT	4.974E 01	1.415E 02	9.858E 01	1.867E 02	1.317E 02	1.690E 02	1.089E 02
T0	6.302E 02	9.809E 02	8.195E 02	6.573E 02	9.781E 02	6.580E 02	8.638E 02
RU0	4.333E-07	5.912E-07	5.231E-07	4.469E-07	5.901E-07	4.473E-07	5.425E-07
SQRT.C0	9.046E-01	8.599E-01	8.760E-01	8.996E-01	8.635E-01	9.002E-01	8.734E-01
H(W)	3.153E 06	3.165E 06	3.159E 06	3.183E 06	3.183E 06	3.201E 06	3.225E 06
T(W)	5.250E 02	5.270E 02	5.260E 02	5.300E 02	5.300E 02	5.330E 02	5.370E 02
P(TS)	5.802E-04	5.415E-04	5.802E-04	4.835E-04	4.835E-04	4.835E-04	3.868E-04
RE(STAG)	1.736E 05	2.406E 05	2.159E 05	5.674E 05	2.269E 05	5.352E 05	2.254E 05

Table II HEAT TRANSFER

RUN	N	CH(N)	RUN	N	CH(N)	RUN	N	CH(N)	RUN	N	CH(N)	RUN	N	CH(N)
5	R01	3.471E-04	6	R01	3.266E-04	7	R01	2.332E-04	8	R01	3.176E-04	9	R01	2.167E-04
5	R02	2.394E-04	6	R02	2.258E-04	7	R02	1.640E-04	8	R02	2.341E-04	9	R02	1.681E-04
5	R03	2.309E-04	6	R03	2.058E-04	7	R03	1.554E-04	8	R03	2.126E-04	9	R03	1.516E-04
5	R04	1.792E-04	6	R04	1.744E-04	7	R04	1.337E-04	8	R04	1.885E-04	9	R04	1.122E-04
5	R05	1.820E-04	6	R05	1.637E-04	7	R05	1.366E-04	8	R05	1.771E-04	9	R05	1.132E-04
5	R06	1.757E-04	6	R06	1.551E-04	7	R06	1.440E-04	8	R06	1.645E-04	9	R06	1.553E-04
5	R07	1.445E-04	6	R07	1.286E-04	7	R07	1.726E-04	8	R07	1.670E-04	9	R07	3.088E-04
5	R08	1.346E-04	6	R08	1.136E-04	7	R08	2.046E-04	8	R08	1.809E-04	9	R08	4.311E-04
5	R09	1.403E-04	6	R09	1.193E-04	7	R09	2.755E-04	8	R09	2.328E-04	9	R09	4.856E-04
5	R10	1.551E-04	6	R10	1.165E-04	7	R10	3.698E-04	8	R10	2.568E-04	9	R10	5.131E-04
5	R11	1.870E-04	6	R11	1.065E-04	7	R11	3.875E-04	8	R11	2.834E-04	9	R11	4.581E-04
5	R12	2.564E-04	6	R12	1.058E-04	7	R12	4.195E-04	8	R12	3.492E-04	9	R12	4.146E-04
5	R13	3.273E-04	6	R13	1.136E-04	7	R13	4.138E-04	8	R13	3.834E-04	9	R13	3.990E-04
5	R14	3.719E-04	6	R14	1.265E-04	7	R14	4.195E-04	8	R14	4.213E-04	9	R14	4.302E-04
5	R15	4.179E-04	6	R15	1.429E-04	7	R15	3.892E-04	8	R15	4.567E-04	9	R15	3.546E-04
5	R16	4.951E-04	6	R16	1.651E-04	7	R17	3.640E-04	8	R16	5.086E-04	9	R16	3.560E-04
5	R17	4.838E-04	6	R17	2.015E-04	7	R18	3.166E-04	8	R17	4.390E-04	9	R17	3.244E-04
5	R19	4.356E-04	6	R18	1.922E-04	7	R19	3.372E-04	8	R19	3.846E-04	9	R19	3.381E-04
5	R20	3.917E-04	6	R19	2.601E-04	7	R20	3.378E-04	8	R20	4.023E-04	9	R20	3.312E-04
5	R21	3.705E-04	6	R20	2.759E-04	7	R21	3.458E-04	8	R21	3.846E-04	9	R21	3.198E-04
5	Q03	3.152E-04	6	R21	2.816E-04	7	Q03	2.692E-04	8	Q03	2.796E-04	9	Q03	2.552E-04
5	Q05	3.046E-04	6	Q03	3.230E-04	7	Q05	2.657E-04	8	Q05	3.264E-04	9	Q05	2.662E-04
5	Q06	3.039E-04	6	Q05	3.259E-04	7	Q06	2.726E-04	8	Q06	3.100E-04	9	Q06	2.703E-04
5	Q07	2.996E-04	6	Q06	3.173E-04	7	Q07	2.497E-04	8	Q07	3.024E-04	9	Q07	2.579E-04
5	Q09	3.910E-04	6	Q07	2.930E-04	7	Q09	2.612E-04	8	Q09	3.264E-04	9	Q09	3.060E-04
5	Q11	3.060E-04	6	Q09	3.159E-04	7	Q11	2.537E-04	8	Q11	3.264E-04	9	Q11	2.689E-04
5	Q15	3.287E-04	6	Q11	3.080E-04	7	Q15	2.543E-04	8	Q15	3.150E-04	9	Q15	2.570E-04
5	Q19	3.719E-04	6	Q15	3.002E-04	7	Q19	3.018E-04	8	Q19	3.505E-04	9	Q19	2.960E-04
5	Q21	3.620E-04	6	Q19	3.716E-04	7	Q21	2.760E-04	8	Q21	3.517E-04	9	Q21	2.840E-04
5	T02	3.010E-04	6	Q21	3.573E-04	7	T02	2.600E-04	8	T02	3.150E-04	9	T02	2.648E-04
5	T04	3.152E-04	6	T02	3.137E-04	7	T04	2.715E-04	8	T04	3.112E-04	9	T04	2.666E-04
5	T06	3.166E-04	6	T04	3.102E-04	7	T06	2.800E-04	8	T06	3.011E-04	9	T06	2.602E-04
5	T08	2.848E-04	6	T06	3.130E-04	7	T08	2.635E-04	8	T08	3.150E-04	9	T08	2.630E-04
5	T10	3.166E-04	6	T08	2.894E-04	7	T10	2.760E-04	8	T10	3.239E-04	9	T10	2.708E-04
5	T11	3.131E-04	6	T10	3.044E-04	7	T11	2.595E-04	8	T11	3.163E-04	9	T11	2.611E-04
5	T13	2.911E-04	6	T11	3.037E-04	7	T13	2.497E-04	8	T16	3.163E-04	9	T16	2.621E-04
5	T16	3.124E-04	6	T16	2.851E-04	7	T16	2.526E-04	8	T18	2.897E-04	9	T18	2.575E-04
5	T18	2.777E-04	6	T18	2.859E-04	7	T18	2.463E-04	8	T20	2.986E-04	9	T20	2.446E-04
5	T20	2.798E-04	6	T20	2.830E-04	7	T20	2.520E-04	8	T22	2.948E-04	9	T22	2.570E-04
5	T22	2.911E-04	6	T22	2.766E-04	7	T22	2.566E-04						

Table II HEAT TRANSFER (Continued)

RUN	N	CH(N)	RUN	N	CH(N)	RUN	N	CH(N)	RUN	N	CH(N)	RUN	N	CH(N)
10	R01	2.447E-04	11	R01	3.516E-04	12	R01	2.767E-04	13	R01	2.606E-04	14	R01	2.192E-04
10	R02	1.743E-04	11	R02	2.470E-04	12	R02	1.874E-04	13	R02	1.942E-04	14	R02	1.490E-04
10	R03	1.731E-04	11	R03	2.377E-04	12	R03	1.667E-04	13	R03	1.865E-04	14	R03	1.330E-04
10	R04	1.233E-04	11	R04	1.817E-04	12	R04	1.275E-04	13	R04	1.523E-04	14	R04	1.234E-04
10	R05	1.413E-04	11	R05	1.766E-04	12	R05	1.163E-04	13	R05	1.327E-04	14	R05	1.305E-04
10	R06	1.301E-04	11	R06	1.683E-04	12	R06	1.135E-04	13	R06	1.160E-04	14	R06	1.132E-04
10	R07	2.117E-04	11	R07	1.624E-04	12	R07	9.508E-05	13	R07	1.132E-04	14	R07	1.376E-04
10	R08	3.082E-04	11	R08	1.314E-04	12	R08	8.561E-05	13	R08	1.048E-04	14	R08	1.762E-04
10	R09	4.215E-04	11	R09	1.490E-04	12	R09	7.525E-05	13	R09	1.048E-04	14	R09	2.551E-04
10	R10	5.330E-04	11	R10	2.051E-04	12	R10	8.111E-05	13	R10	1.285E-04	14	R10	3.639E-04
10	R11	4.769E-04	11	R11	2.093E-04	12	R11	7.435E-05	13	R11	2.214E-04	14	R11	4.299E-04
10	R12	4.514E-04	11	R12	2.227E-04	12	R12	7.074E-05	13	R12	2.976E-04	14	R12	4.284E-04
10	R13	4.327E-04	11	R13	2.922E-04	12	R13	7.840E-05	13	R13	4.408E-04	14	R13	4.542E-04
10	R14	4.277E-04	11	R14	4.437E-04	12	Q03	8.651E-05	13	Q02	4.534E-04	[illegible]	[illegible]	3.969E-04
10	R15	4.253E-04	11	R15	4.587E-04	12	Q05	9.778E-05	13	Q03	4.205E-04	[illegible]	[illegible]	3.754E-04
10	R16	4.48[illegible]-04	11	R16	5.927E-04	12	Q06	1.000E-04	13	Q05	4.136E-04	[illegible]	[illegible]	3.582E-04
10	R17	3.705E-04	11	R17	5.048E-04	12	Q07	8.516E-05	13	Q07	4.101E-04	[illegible]	[illegible]	3.897E-04
10	R19	3.493E-04	11	R19	4.713E-04	12	Q09	9.508E-05	13	Q11	4.038E-04	[illegible]	[illegible]	4.026E-04
10	R20	3.281E-04	11	R20	4.805E-04	12	Q11	7.795E-05	13	Q15	4.115E-04	14	Q[illegible]	[illegible]
10	R21	3.400E-04	11	R21	4.822E-04	12	Q15	8.471E-05	13	Q20	4.988E-04	14	Q21	[illegible]
10	Q03	2.777E-04	11	Q03	3.767E-04	12	Q21	7.975E-05	13	Q21	4.722E-04	14	T01	[illegible]
10	Q05	2.845E-04	11	Q05	3.767E-04	12	T02	1.068E-04	13	T01	3.793E-04	14	T02	3.[illegible]
10	Q06	2.764E-04	11	Q06	3.734E-04	12	T04	1.203E-04	13	T02	4.261E-04	14	T03	3.912E-04
10	Q07	2.727E-04	11	Q07	3.399E-04	12	T06	1.433E-04	13	T03	3.989E-04	14	T04	4.041E-04
10	Q09	3.244E-04	11	Q09	3.851E-04	12	T08	1.672E-04	13	T04	4.268E-04	14	T05	4.069E-04
10	Q11	3.113E-04	11	Q11	3.784E-04	12	T10	2.343E-04	13	T05	3.905E-04	14	T06	4.184E-04
10	Q15	2.677E-04	11	Q15	3.809E-04	12	T11	2.406E-04	13	T06	4.212E-04	14	T07	4.041E-04
10	Q19	3.194E-04	11	Q21	4.060E-04	12	T16	2.974E-04	13	T07	4.254E-04	14	T08	3.940E-04
10	Q21	2.908E-04	11	T02	3.708E-04	12	T18	2.938E-04	13	T08	3.940E-04	14	T09	4.528E-04
10	T02	2.677E-04	11	T04	3.625E-04	12	T20	2.938E-04	13	T09	4.485E-04	14	T10	4.170E-04
10	T04	2.758E-04	11	T06	3.616E-04	12	T22	3.064E-04	13	T10	4.492E-04	14	T11	4.127E-04
10	T06	2.802E-04	11	T08	3.415E-04				13	T11	4.024E-04	14	T14	4.256E-04
10	T08	2.640E-04	11	T10	3.591E-04				13	T14	4.359E-04	14	T15	4.256E-04
10	T10	2.596E-04	11	T11	3.642E-04				13	T15	4.499E-04	14	T16	4.227E-04
10	T11	2.590E-04	11	T16	3.499E-04				13	T16	4.457E-04	14	T18	4.112E-04
10	T16	2.640E-04	11	T18	3.365E-04				13	T18	4.331E-04	14	T20	3.983E-04
10	T18	2.515E-04	11	T20	3.173E-04				13	T20	4.548E-04	14	T22	4.055E-04
10	T20	2.459E-04	11	T22	3.374E-04				13	T22	4.534E-04			
10	T22	2.565E-04												

Table II HEAT TRANSFER (Concluded)

RUN	N	CH(N)	RUN	N	CH(N)	RUN	N	CH(N)	RUN	N	CH(N)	RUN	N	CH(N)
15	R01	2.150E-04	16	R01	1.012E-04	17	R01	2.823E-04	18	R01	1.142E-04	19	R01	2.571E-04
15	R02	1.516E-04	16	R02	8.668E-05	17	R02	1.881E-04	18	R02	1.012E-04	19	R02	1.728E-04
15	R03	1.387E-04	16	R03	1.363E-04	17	R03	1.537E-04	18	R03	1.132E-04	19	R03	1.414E-04
15	R04	1.392E-04	16	R04	2.281E-04	17	R04	1.072E-04	18	R04	2.653E-04	19	R04	1.176E-04
15	R05	1.432E-04	16	R05	3.720E-04	17	R05	1.020E-04	18	R05	3.203E-04	19	R05	8.954E-05
15	R06	1.271E-04	16	R06	3.895E-04	17	R06	9.020E-05	18	R06	3.400E-04	19	R06	8.649E-05
15	R07	1.253E-04	16	R07	4.281E-04	17	R07	1.358E-04	18	R07	3.636E-04	19	R07	1.285E-04
15	R08	1.494E-04	16	R08	4.457E-04	17	R08	1.750E-04	18	R08	3.360E-04	19	R08	1.871E-04
15	R09	1.932E-04	16	R09	4.615E-04	17	R09	3.154E-04	18	R09	3.341E-04	19	R09	2.963E-04
15	R10	2.700E-04	16	R10	4.966E-04	17	R10	4.810E-04	18	R10	3.518E-04	19	R10	4.444E-04
15	R11	4.236E-04	16	R11	4.597E-04	17	R11	5.062E-04	18	R11	3.537E-04	19	R11	4.553E-04
15	R12	4.532E-04	16	R12	4.474E-04	17	R12	4.983E-04	18	R12	3.321E-04	19	R12	4.662E-04
15	R13	4.707E-04	16	R13	4.281E-04	17	R13	5.141E-04	18	R13	3.341E-04	19	R13	4.728E-04
15	Q02	3.864E-04	16	Q02	3.334E-04	17	Q02	3.911E-04	18	Q02	3.773E-04	19	Q02	3.638E-04
15	Q03	3.716E-04	16	Q03	3.194E-04	17	Q03	3.674E-04	18	Q03	3.360E-04	19	Q03	3.551E-04
15	Q05	3.567E-04	16	Q05	3.281E-04	17	Q05	3.848E-04	18	Q05	3.498E-04	19	Q05	3.616E-04
15	Q07	3.815E-04	16	Q07	3.316E-04	17	Q07	4.053E-04	18	Q07	3.596E-04	19	Q07	3.660E-04
15	Q11	3.988E-04	16	Q11	3.406E-04	17	Q11	4.337E-04	18	Q11	3.752E-04	19	Q09	3.943E-04
15	Q20	4.608E-04	16	T01	3.299E-04	17	Q15	4.273E-04	18	Q15	3.616E-04	19	Q11	3.987E-04
15	T01	3.939E-04	16	T02	3.264E-04	17	Q17	4.210E-04	18	Q17	3.636E-04	19	Q15	3.900E-04
15	T02	3.815E-04	16	T03	3.281E-04	17	Q19	4.210E-04	18	Q19	3.793E-04	19	Q17	3.900E-04
15	T03	3.889E-04	16	T04	3.474E-04	17	Q20	4.226E-04	18	Q20	3.655E-04	19	Q19	4.009E-04
15	T04	4.038E-04	16	T05	3.316E-04	17	Q21	4.494E-04	18	Q21	3.419E-04	19	Q20	3.878E-04
15	T05	3.741E-04	16	T06	3.457E-04	17	T01	3.832E-04	18	T01	3.616E-04	19	Q21	4.052E-04
15	T06	4.038E-04	16	T07	3.246E-04	17	T02	3.753E-04	18	T02	3.400E-04	19	T01	3.769E-04
15	T07	3.914E-04	16	T08	3.176E-04	17	T03	4.005E-04	18	T03	3.557E-04	19	T02	3.616E-04
15	T08	3.914E-04	16	T09	3.527E-04	17	T04	3.848E-04	18	T04	3.616E-04	19	T03	3.725E-04
15	T09	4.211E-04	16	T10	3.544E-04	17	T05	3.942E-04	18	T05	3.655E-04	19	T04	3.616E-04
15	T10	4.087E-04	16	T11	3.316E-04	17	T06	4.053E-04	18	T06	3.498E-04	19	T05	3.508E-04
15	T11	3.939E-04	16	T14	3.158E-04	17	T07	3.627E-04	18	T07	3.400E-04	19	T06	3.747E-04
15	T14	3.914E-04	16	T15	3.194E-04	17	T08	3.595E-04	18	T08	3.341E-04	19	T07	3.464E-04
15	T15	3.964E-04	16	T16	3.086E-04	17	T09	4.037E-04	18	T09	3.871E-04	19	T08	3.420E-04
15	T16	3.765E-04	16	T18	3.036E-04	17	T10	3.769E-04	18	T10	3.596E-04	19	T09	3.878E-04
15	T18	3.741E-04	16	T20	3.053E-04	17	T11	3.753E-04	18	T11	3.675E-04	19	T10	3.747E-04
15	T20	3.815E-04	16	T22	3.176E-04	17	T14	3.753E-04	18	T12	3.164E-04	19	T11	3.757E-04
15	T22	4.087E-04				17	T15	3.816E-04	18	T14	3.439E-04	19	T14	3.551E-04
						17	T16	3.785E-04	18	T15	3.459E-04	19	T15	3.595E-04
						17	T18	3.611E-04	18	T16	3.478E-04	19	T16	3.660E-04
						17	T20	3.769E-04	18	T18	3.459E-04	19	T18	3.496E-04
						17	T22	3.800E-04	18	T20	3.282E-04	19	T20	3.496E-04
									18	T22	3.439E-04	19	T22	3.660E-04

Table II SKIN FRICTION

RUN	N	CF(N)	RUN	N	CF(N)	RUN	N	CF(N)	RUN	N	CF(N)
5	S 1	8.23E-04	6	S 1	8.74E-04	7	S 1	6.39E-04	8	S 1	9.43E-04
5	S 3	8.71E-04	6	S 3	8.76E-04	7	S 3	5.53E-04	8	S 3	8.56E-04
5	S 4	8.18E-04	6	S 4	9.51E-04	7	S 4	6.02E-04	8	S 4	9.41E-04
5	S 5	8.29E-04	6	S 5	8.53E-04	7	S 5	5.19E-04	8	S 5	8.51E-04
5	S 6	8.27E-04	6	S 6	8.20E-04	7	S 6	5.38E-04	8	S 6	8.50E-04
5	S10	8.66E-04	6	S10	8.44E-04	7	S10	6.72E-04	8	S10	9.20E-04
5	K 1	7.72E-04	6	K 1	6.56E-04	7	K 2	5.90E-04	8	K 1	8.04E-04
5	K 2	6.97E-04	6	K 2	8.29E-04	7	K 3	5.67E-04	8	K 2	7.90E-04
5	K 3	7.82E-04	6	K 3	7.75E-04	7	K 4	5.49E-04	8	K 3	7.72E-04
5	K 4	6.94E-04	6	K 4	8.02E-04	7	K 5	6.33E-04	8	K 4	8.07E-04
5	K 5	6.85E-04	6	K 5	6.48E-04	7	K 6	5.59E-04	8	K 5	6.97E-04
5	K 6	6.76E-04	6	K 6	8.59E-04	7	K 8	5.54E-04	8	K 6	6.63E-04
5	K 8	7.81E-04	6	K 8	8.17E-04				8	K 8	7.78E-04

RUN	N	CF(N)	RUN	N	CF(N)	RUN	N	CF(N)	RUN	N	CF(N)
9	S 1	6.38E-04	10	S 1	6.13E-04	11	S 1	8.31E-04	12	S 1	2.29E-04
9	S 3	5.50E-04	10	S 3	6.30E-04	11	S 3	8.09E-04	12	S 3	2.11E-04
9	S 4	6.46E-04	10	S 4	5.25E-04	11	S 4	9.00E-04	12	S 4	1.77E-04
9	S 5	5.22E-04	10	S 5	6.20E-04	11	S 5	8.47E-04	12	S 5	1.55E-04
9	S 6	5.46E-04	10	S 6	5.77E-04	11	S 6	7.98E-04	12	S 6	1.46E-04
9	S10	6.63E-04	10	S10	6.63E-04	11	S10	8.39E-04	12	S10	2.41E-04
9	K 2	5.80E-04	10	K 1	5.87E-04	11	K 1	7.55E-04	12	K 1	2.76E-04
9	K 3	5.34E-04	10	K 2	5.98E-04	11	K 2	8.11E-04	12	K 2	2.87E-04
9	K 4	5.39E-04	10	K 3	5.61E-04	11	K 3	7.93E-04	12	K 3	3.11E-04
9	K 6	5.43E-04	10	K 4	5.73E-04	11	K 4	7.78E-04	12	K 4	3.12E-04
			10	K 5	6.52E-04	11	K 5	7.08E-04	12	K 5	5.41E-04
			10	K 6	5.58E-04	11	K 6	7.31E-04	12	K 6	4.93E-04
			10	K 8	5.68E-04	11	K 8	7.72E-04	12	K 8	5.85E-04

Table II SKIN FRICTION (Concluded)

RUN	N	CF(N)	RUN	N	CF(N)	RUN	N	CF(N)	RUN	N	CF(N)
13	S 1	7.45E-04	14	S 1	7.21E-04	15	S 1	6.06E-04	16	S 1	6.97E-04
13	S 3	8.09E-04	14	S 3	7.11E-04	15	S 3	7.97E-04	16	S 3	5.14E-04
13	S 4	6.52E-04	14	S 4	7.50E-04	15	S 4	7.55E-04	16	S 4	4.95E-04
13	S 5	8.33E-04	14	S 5	6.80E-04	15	S 5	7.84E-04	16	S 5	3.40E-04
13	S 6	8.09E-04	14	S 6	7.73E-04	15	S 6	7.67E-04	16	S 6	5.61E-04
13	S10	8.51E-04	14	S10	6.93E-04	15	S10	7.97E-04	16	S10	6.63E-04
13	K 1	7.31E-04	14	K 1	6.75E-04	15	K 1	7.53E-04	16	K 1	6.38E-04
13	K 2	7.38E-04	14	K 2	7.33E-04	15	K 2	7.91E-04	16	K 2	6.72E-04
13	K 3	7.88E-04	14	K 3	6.93E-04	15	K 3	7.30E-04	16	K 3	6.05E-04
13	K 4	7.52E-04	14	K 4	6.56E-04	15	K 4	7.66E-04	16	K 4	6.75E-04
13	K 5	1.04E-03	14	K 5	6.70E-04	15	K 5	7.44E-04	16	K 5	6.18E-04
13	K 6	7.32E-04	14	K 6	6.80E-04	15	K 6	7.95E-04	16	K 6	5.45E-04
13	K 8	7.45E-04	14	K 8	6.69E-04	15	K 8	7.25E-04	16	K 8	6.33E-04

RUN	N	CF(N)	RUN	N	CF(N)	RUN	N	CF(N)
17	S 1	8.80E-04	18	S 1	8.51E-04	19	S 1	8.53E-04
17	S 3	8.59E-04	18	S 3	6.40E-04	19	S 3	8.39E-04
17	S 4	8.44E-04	18	S 4	8.13E-04	19	S 4	5.96E-04
17	S 5	8.07E-04	18	S 5	7.20E-04	19	S 5	7.12E-04
17	S 6	8.18E-04	18	S 6	7.09E-04	19	S 6	8.09E-04
17	S10	8.56E-04	18	S10	7.28E-04	19	S10	8.86E-04
17	K 1	8.19E-04	18	K 1	6.85E-04	19	K 1	7.59E-04
17	K 2	8.56E-04	18	K 2	9.05E-04	19	K 2	8.33E-04
17	K 3	7.60E-04	18	K 3	6.33E-04	19	K 3	7.31E-04
17	K 4	9.03E-04	18	K 4	7.44E-04	19	K 4	7.85E-04
17	K 5	8.19E-04	18	K 5	7.37E-04	19	K 5	8.19E-04
17	K 6	7.89E-04	18	K 6	7.82E-04	19	K 6	7.28E-04
17	K 8	7.84E-04	18	K 8	6.18E-04	19	K 8	7.42E-04

Table II PRESSURE

RUN N	CP(N)	RUN N	CP(N)	RUN N	CP(N)	RUN N	CP(N)	RUN N	CP(N)
5 P 1	1.35E-02	6 P 1	1.01E-02	7 P 1	1.19E-02	8 P 1	1.29E-02	9 P 1	1.10E-02
5 P 2	1.26E-02	6 P 2	1.01E-02	7 P 2	1.15E-02	8 P 2	1.30E-02	9 P 2	1.35E-02
5 P 4	1.47E-02	6 P 4	1.03E-02	7 P 4	1.23E-02	8 P 4	1.34E-02	9 P 4	1.45E-02
5 P 8	1.38E-02	6 P 8	9.86E-03	7 P 8	1.18E-02	8 P 8	1.29E-02	9 P 8	1.40E-02
5 P10	1.29E-02	6 P10	1.04E-02	7 P10	1.18E-02	8 P10	1.34E-02	9 P10	1.37E-02
5PF 5	1.27E-02	6PF 5	1.05E-02	7PF 5	1.17E-02	8PF 5	1.28E-02	9PF 5	1.40E-02
5PF 7	1.21E-02	6PF 7	9.52E-03	7PF 7	1.13E-02	8PF 7	1.20E-02	9PF 7	1.31E-02
5PF 9	1.15E-02	6PF 9	9.46E-03	7PF 9	1.15E-02	8PF 9	1.17E-02	9PF 9	1.31E-02
5PF10	1.15E-02	6PF10	9.46E-03	7PF10	1.08E-02	8PF10	1.19E-02	9PF10	1.24E-02
5PF12	1.11E-02	6PF12	9.26E-03	7PF12	1.18E-02	8PF12	1.16E-02	9PF16	1.32E-02
5PF14	9.92E-03	6PF14	9.26E-03	7PF14	1.11E-02	8PF14	1.23E-02	9PF18	1.27E-02
5PF16	1.21E-02	6PF16	9.46E-03	7PF16	1.17E-02	8PF16	1.22E-02	9PF19	1.33E-02
5PF18	1.12E-02	6PF18	9.46E-03	7PF18	1.14E-02	8PF18	1.16E-02		
5PF19	1.23E-02	6PF19	9.46E-03	7PF19	1.15E-02	8PF19	1.23E-02		

RUN N	CP(N)	RUN N	CP(N)	RUN N	CP(N)	RUN N	CP(N)	RUN N	CP(N)
10 P 1	1.50E-02	11 P 1	1.69E-02	12 P 1	1.37E-02	13 P 1	2.94E-02	14 P 1	2.66E-02
10 P 2	1.40E-02	11 P 2	1.58E-02	12 P 2	1.32E-02	13 P 2	2.47E-02	14 P 2	2.27E-02
10 P 4	1.52E-02	11 P 4	1.70E-02	12 P 4	1.36E-02	13 P 4	2.72E-02	14 P 4	2.55E-02
10 P 8	1.44E-02	11 P 8	1.63E-02	12 P 8	1.30E-02	13 P 8	2.57E-02	14 P 8	2.51E-02
10 P10	1.54E-02	11 P10	1.62E-02	12 P10	1.30E-02	13 P10	2.51E-02	14 P10	2.14E-02
10PF 5	1.41E-02	11PF 5	1.62E-02	12PF 5	1.29E-02	13PF 5	2.80E-02	14PF 5	2.59E-02
10PF 7	1.34E-02	11PF 7	1.50E-02	12PF 7	1.23E-02	13PF 7	2.73E-02	14PF 7	2.60E-02
10PF 9	1.38E-02	11PF 9	1.53E-02	12PF 9	1.21E-02	13PF 9	2.78E-02	14PF 9	2.65E-02
10PF10	1.32E-02	11PF10	1.49E-02	12PF10	1.22E-02	13PF10	2.77E-02	14PF10	2.56E-02
10PF12	1.36E-02	11PF12	1.55E-02	12PF12	1.19E-02	13PF12	2.96E-02	14PF12	2.70E-02
10PF14	1.35E-02	11PF14	1.56E-02	12PF14	1.24E-02	13PF14	3.10E-02	14PF14	2.59E-02
10PF16	1.38E-02	11PF16	1.56E-02	12PF16	1.31E-02	13PF16	3.07E-02	14PF16	2.27E-02
10PF18	1.33E-02	11PF18	1.49E-02	12PF18	1.22E-02	13PF18	2.95E-02	14PF18	2.51E-02
10PF19	1.38E-02	11PF19	1.61E-02	12PF19	1.27E-02	13PF19	1.65E-02	14PF19	2.47E-02

RUN N	CP(N)	RUN N	CP(N)	RUN N	CP(N)	RUN N	CP(N)	RUN N	CP(N)
15 P 1	2.61E-02	16 P 1	2.92E-02	17 P 1	2.98E-02	18 P 1	3.52E-02	19 P 1	2.77E-02
15 P 2	2.25E-02	16 P 2	2.37E-02	17 P 2	2.69E-02	18 P 2	2.92E-02	19 P 2	2.61E-02
15 P 4	2.61E-02	16 P10	2.65E-02	17 P 4	3.13E-02	18 P 4	3.38E-02	19 P 4	2.89E-02
15 P 8	2.53E-02	16PF 5	2.38E-02	17 P 8	2.81E-02	18 P 8	3.28E-02	19 P 8	2.80E-02
15 P10	2.24E-02	16PF 7	2.28E-02	17 P10	2.68E-02	18 P10	2.75E-02	19 P10	2.66E-02
15PF 5	2.56E-02	16PF 9	2.19E-02	17PF 5	2.69E-02	18PF 5	3.03E-02	19PF 5	2.65E-02
15PF 7	2.44E-02	16PF10	2.11E-02	17PF 7	2.66E-02	18PF 7	2.89E-02	19PF 7	2.70E-02
15PF 9	2.45E-02	16PF12	2.23E-02	17PF 9	2.69E-02	18PF 9	2.51E-02	19PF 9	2.66E-02
15PF10	2.35E-02	16PF14	2.18E-02	17PF10	2.61E-02	18PF10	2.79E-02	19PF10	2.65E-02
15PF12	2.49E-02	16PF16	2.10E-02	17PF12	2.79E-02	18PF12	2.77E-02	19PF12	2.27E-02
15PF14	2.58E-02	16PF18	2.13E-02	17PF14	2.64E-02	18PF14	2.72E-02	19PF14	2.58E-02
15PF16	2.43E-02	16PF19	2.27E-02	17PF16	2.66E-02	18PF16	2.68E-02	19PF16	2.61E-02
15PF18	2.60E-02			17PF18	2.61E-02	18PF18	2.48E-02	19PF18	2.58E-02
15PF19	2.46E-02			17PF19	2.88E-02	18PF19	2.95E-02	19PF19	2.73E-02

Table III
GAGE POSITIONS ON FLAT PLATE

FLAT PLATE WITH 28" LEADING EDGE					
HEAT TRANSFER		SKIN FRICTION		PRESSURE	
GAGE	DIST. FROM L. E. (IN.)	GAGE	DIST. FROM L. E. (IN.)	GAGE	DIST. FROM L. E. (IN.)
R1	2	S1	39.56	P2	38.82
R2	4	S3	38.27	P4	37.75
R3	5	S4	37.75	P8	35.02
R4	6	S5	37.21	P10	32.53
R5	7	S6	36.72	Pf18	51.36
R6	8	S10	32.53	Pf5	43.02
R7	10	K1	40.48	Pf7	44.31
R8	11	K2	41.43	Pf9	45.59
R9	12	K3	42.39	Pf10	46.22
R10	13	K4	43.32	Pf12	47.50
R11	14	K5	44.31	Pf14	48.79
R12	16	K6	45.27	Pf16	50.07
R13	17	K8	47.19	Pf19	40.41
R14	18			P1	39.56
R15	19			P11	30.27
R16	20			Pf1	40.48
R17	22			Pf2	41.13
R18	23			Pf3	41.78
R19	25			Pf4	42.38
R20	26			Pf6	43.67
R21	27			FLUSH	39.56
Q1	39.89				
Q2	39.68				
Q3	39.59				
Q5	39.28				
Q6	39.13				
Q7	38.82				
Q9	38.29				
Q11	37.76				
Q15	36.69				
Q19	35.04				
Q21	32.52				
T2	40.56				
T4	41.21				
T6	41.85				
T8	42.50				
T10	43.67				
T11	44.31				
T12	44.94				
T13	45.59				
T16	47.50				
T18	48.79				
T20	50.07				
T22	51.36				

FLAT PLATE WITH 15" LEADING EDGE					
HEAT TRANSFER		SKIN FRICTION		PRESSURE	
GAGE	DIST. FROM L. E. (IN.)	GAGE	DIST. FROM L. E. (IN.)	GAGE	DIST. FROM L. E. (IN.)
R1	1	S1	26.56	P2	25.82
R2	2	S3	25.27	P4	24.75
R3	3	S4	24.75	P8	22.02
R4	4	S5	24.21	P10	19.53
R5	5	S6	23.72	Pf18	38.36
R6	6	S10	19.53	Pf5	30.02
R7	7	K1	27.48	Pf7	31.31
R8	8	K2	28.43	Pf9	32.59
R9	9	K3	29.39	Pf10	33.22
R10	10	K4	30.32	Pf12	34.50
R11	12	K5	31.31	Pf14	35.79
R12	13	K6	32.27	Pf16	37.07
R13	14	K8	34.19	Pf19	27.41
Q1	26.89			P1	26.56
Q2	26.68			P11	17.27
Q3	26.59			Pf1	27.48
Q5	26.28			Pf2	28.13
Q6	26.13			Pf3	28.78
Q7	25.82			Pf4	29.38
Q9	25.29			Pf6	30.67
Q11	24.76			FLUSH	26.56
Q15	23.69				
Q17	23.13				
Q19	22.04				
Q20	21.02				
Q21	19.52				
T1	27.36				
T2	27.56				
T3	28.01				
T4	28.21				
T5	28.66				
T6	28.85				
T7	29.30				
T8	29.50				
T9	30.02				
T10	30.67				
T11	31.31				
T12	31.94				
T13	32.59				
T14	33.22				
T15	33.87				
T16	34.50				
T18	35.79				
T20	37.07				
T22	38.36				

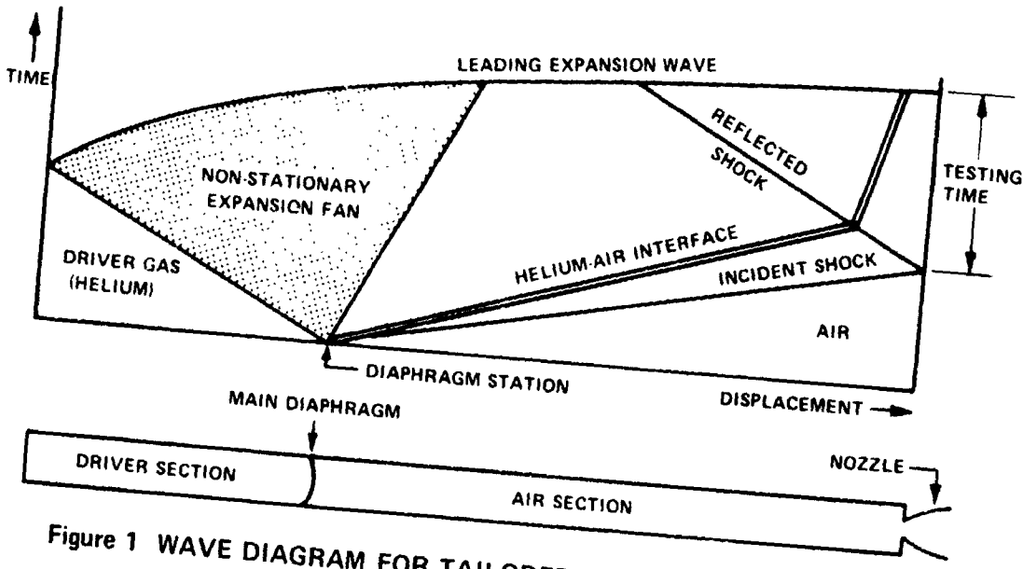

Figure 1 WAVE DIAGRAM FOR TAILORED–INTERFACE SHOCK TUBE

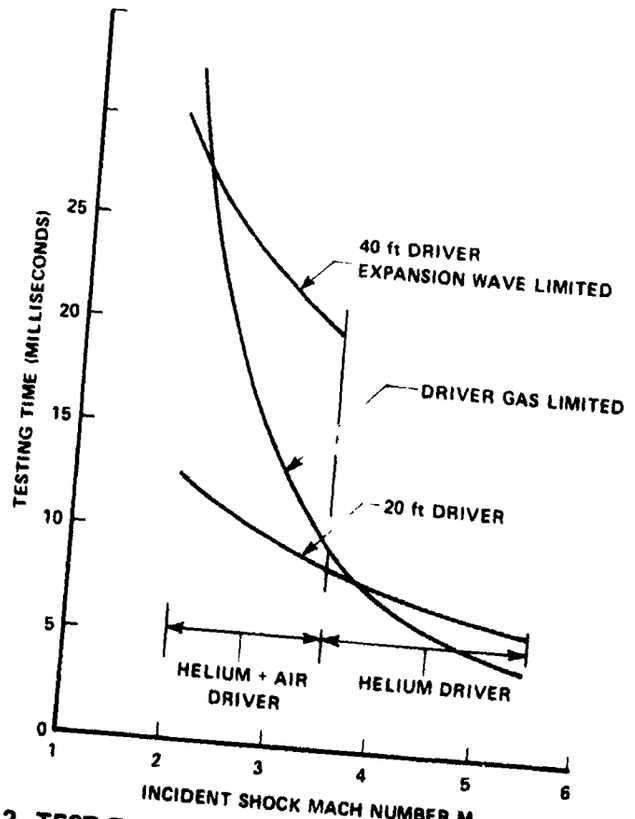

Figure 2 TEST TIME AVAILABLE FOR TAILORED INTERFACE OPERATION OF THE SHOCK TUNNEL

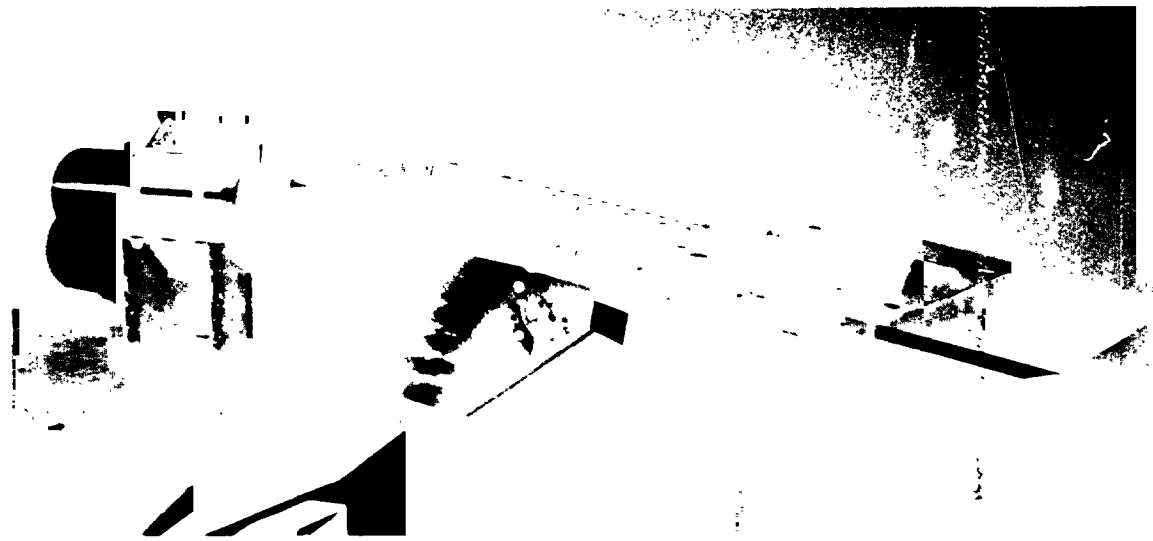

Figure 3 FLAT PLATE MODEL

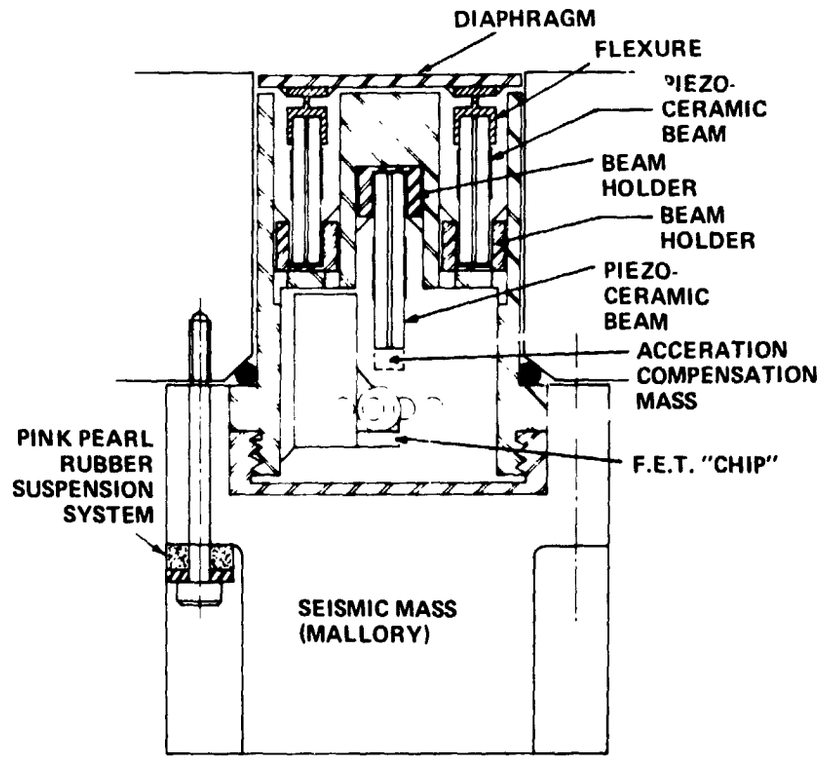

Figure 4 DRAWING OF SECTION THROUGH SKIN FRICTION TRANSDUCER

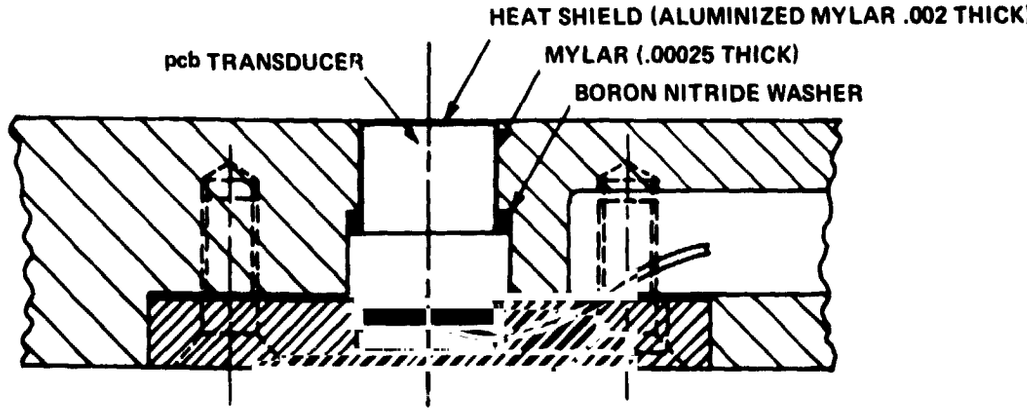

(a) TYPICAL MOUNTING TECHNIQUE USED IN MODEL

Figure 5 HIGH FREQUENCY PRESSURE MOUNTING

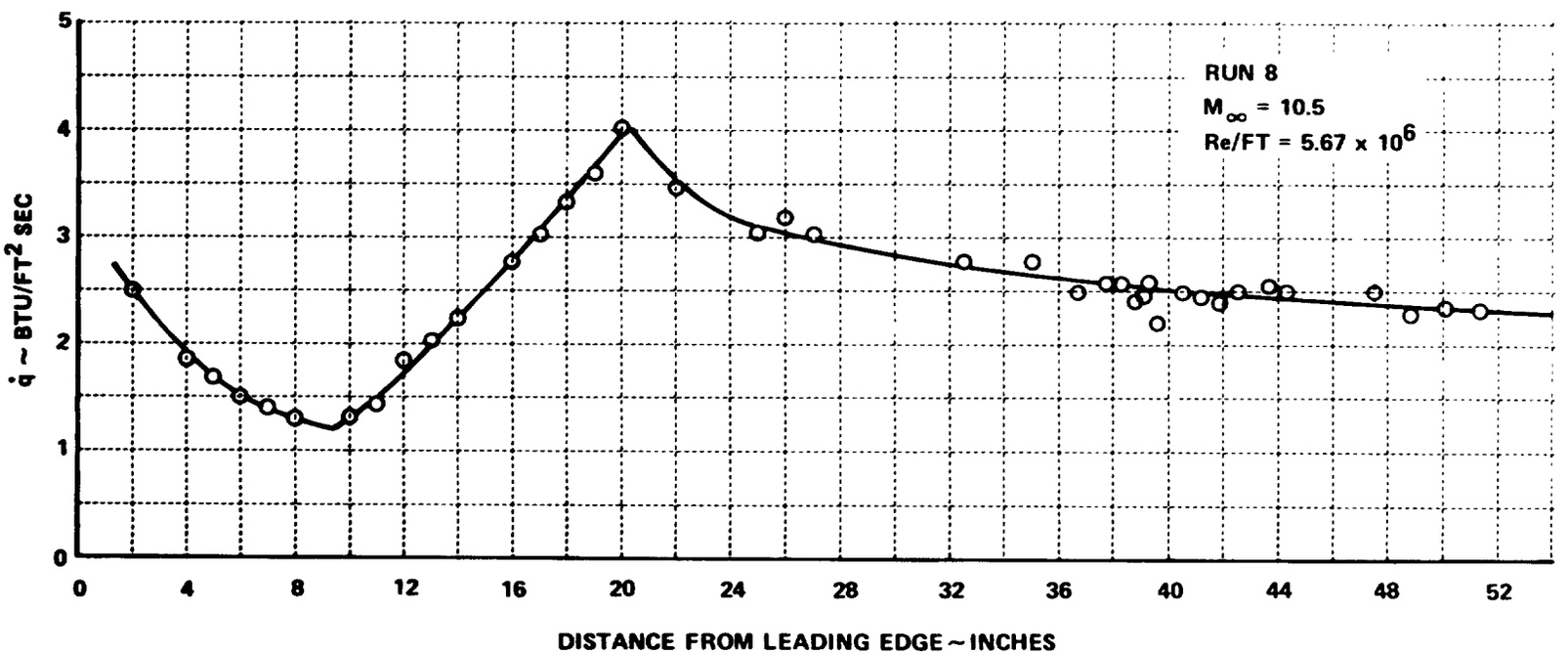

Figure 6 TYPICAL DISTRIBUTION OF HEAT TRANSFER ALONG THE FLAT PLATE MODEL

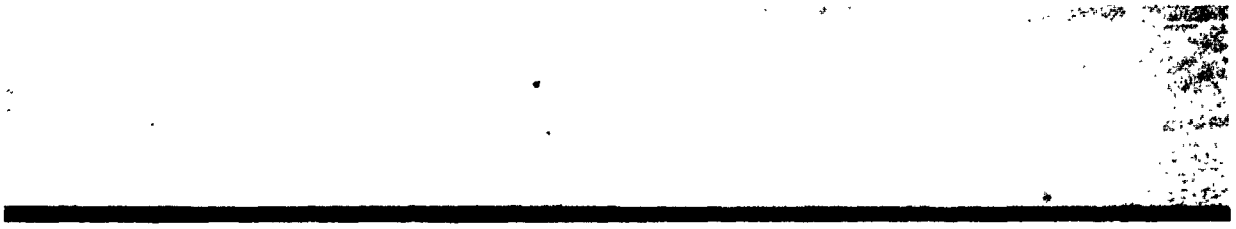

Figure 7a RUN 5 M = 10.4, Re/FT = 5.2×10^6, $T_W/T_0 = 0.16$

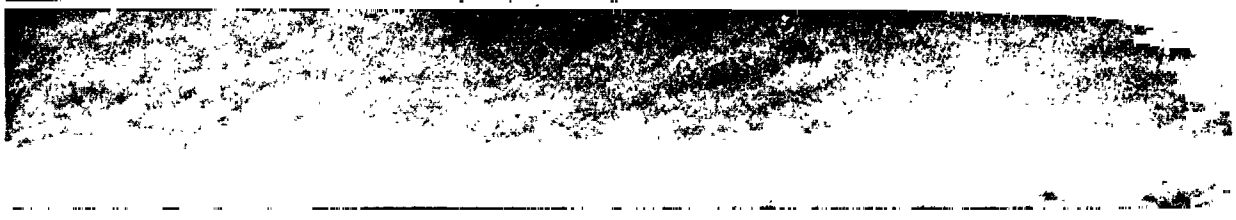

Figure 7b RUN 6 M = 12, Re/FT = 6.3×10^6, $T_W/T_0 = 0.16$

Figure 7c RUN 7 M = 11, Re/FT = 11×10^6, $T_W/T_0 = 0.19$

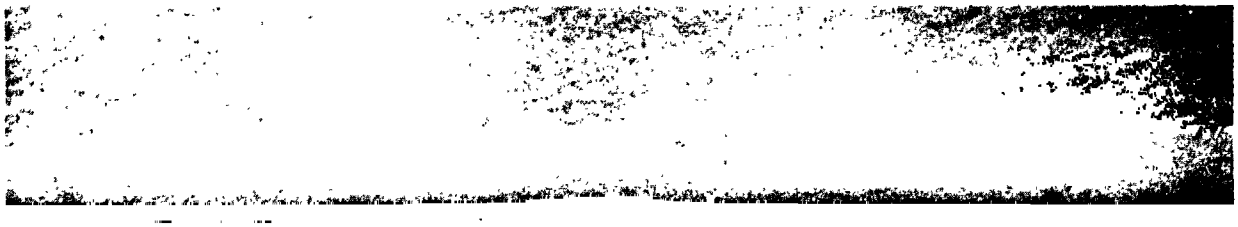

Figure 7d RUN 8 M = 10.5, Re/FT = 5.7×10^6, $T_W/T_0 = 0.21$

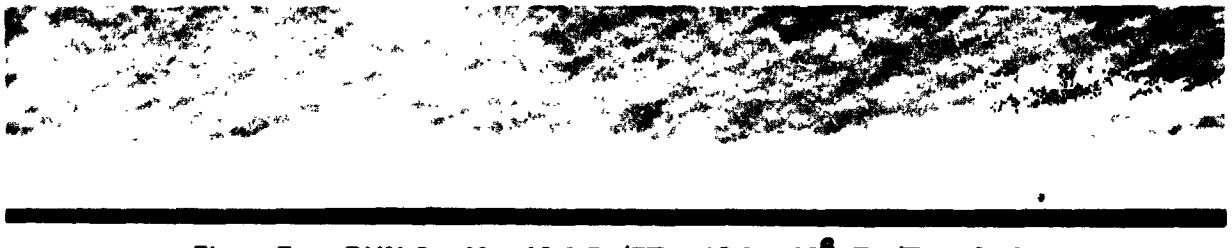

Figure 7e RUN 9 M = 10.6 Re/FT = 13.6×10^6, $T_W/T_0 = 0.19$

Figure 7f RUN 10 M = 10.6, Re/FT = 10.6 x 10^6, T_W/T_0 = 0.21

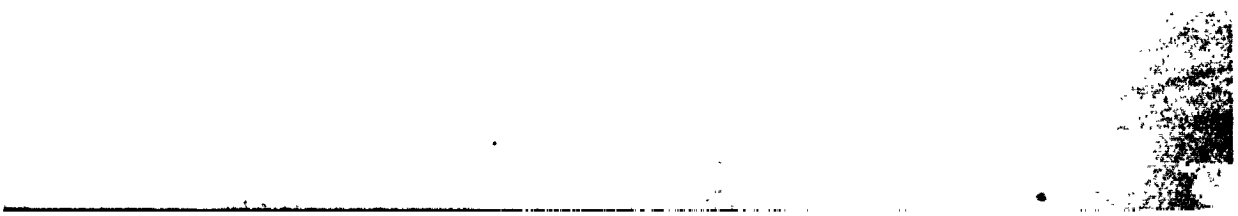

Figure 7g RUN 11 M = 10.6, Re/FT = 4.6 x 10^6, T_W/T_0 = 0.16

Figure 7h RUN 12 M = 10.6, Re/FT = 13.3 x 10^6, T_W/T_0 = 0.19

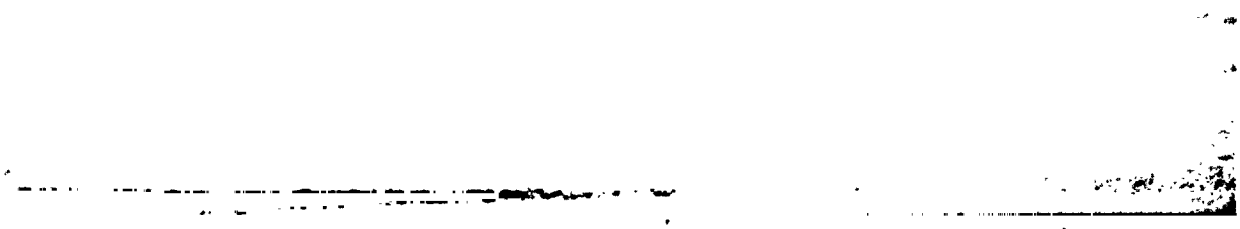

Figure 7i RUN 13 M = 8, Re/FT = 16.0 x 10^6, T_W/T_0 = 0.31

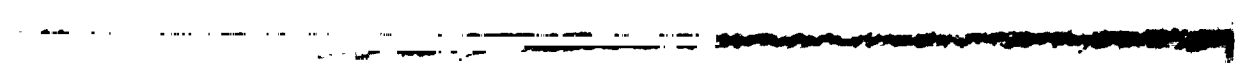

Figure 7j RUN 14 M = 8, Re/FT = 15.5 x 10^6, T_W/T_0 = 0.16

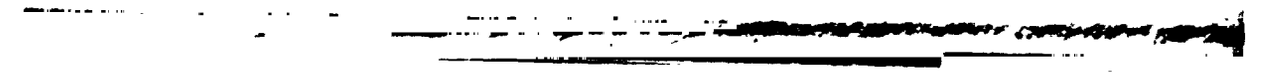

Figure 7k RUN 15 M = 8, Re/FT = 58.5 x 10^6, T_W/T_0 = 0.16

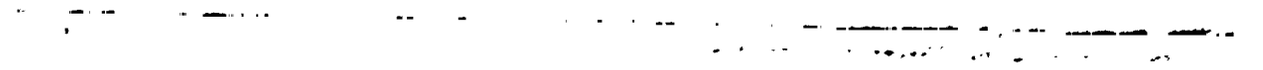

Figure 7l RUN 16 M = 8, Re/FT = 58.5 x 10^6, T_W/T_0 = 0.31

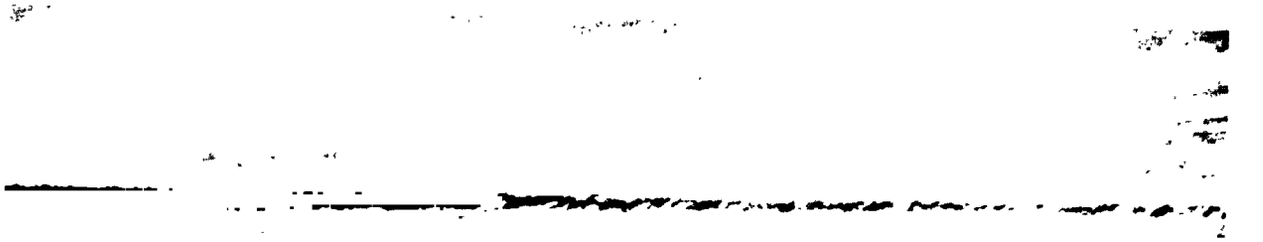

Figure 7m RUN 17 M = 7.5, Re/FT = 14.4 x 10^6, T_W/T_0 = 0.16

Figure 7n RUN 18 M = 7.5, Re/FT = 47.5 x 10^6, T_W/T_0 = 0.28

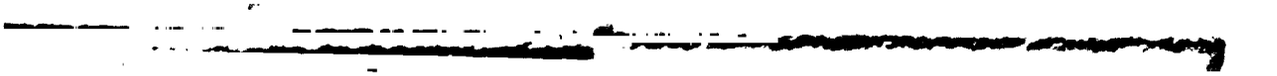

Figure 7o RUN 19 M = 7.5, Re/FT = 15.6 x 10^6, T_W/T_0 = 0.21

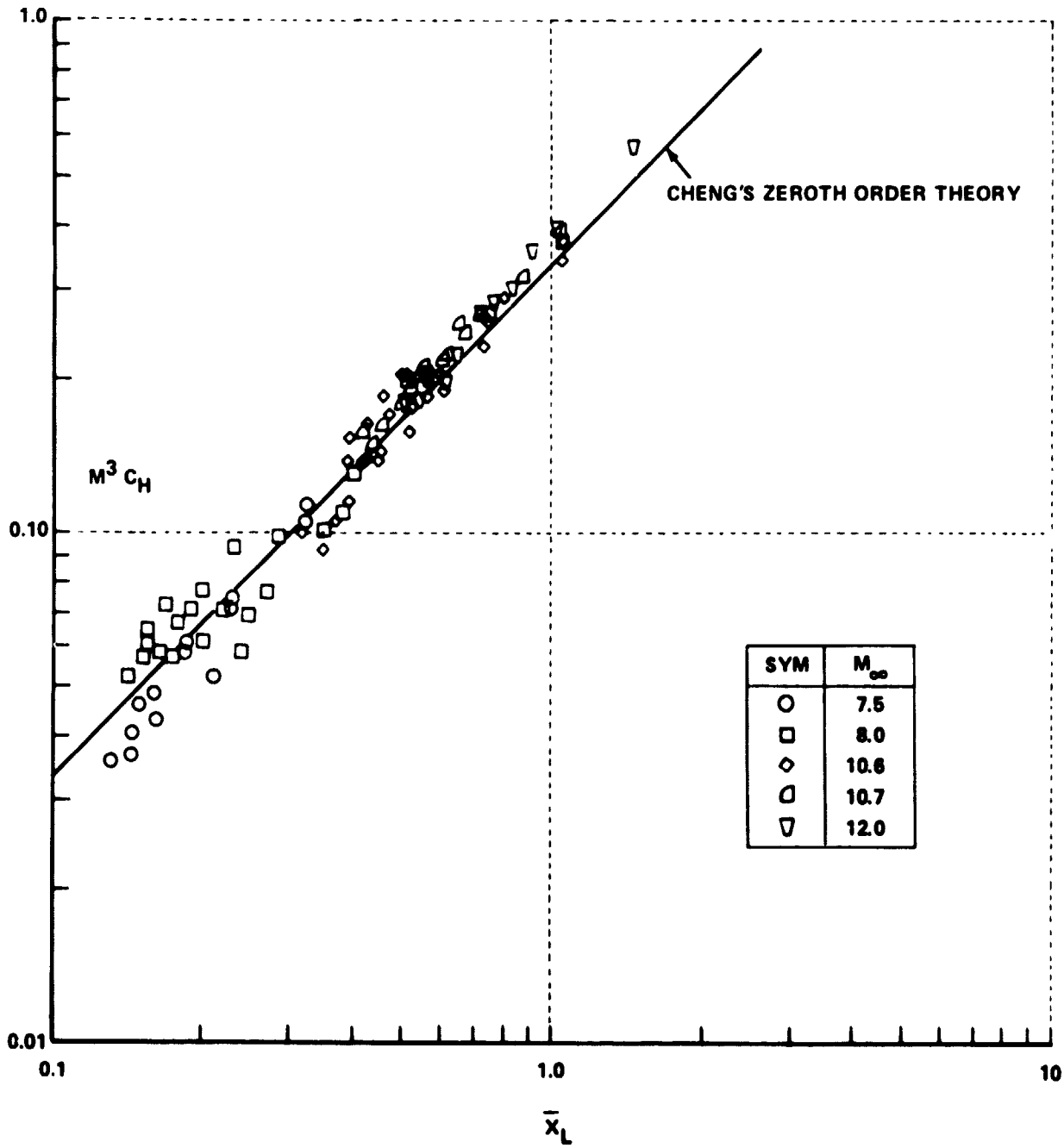

Figure 8 CORRELATION OF LAMINAR HEAT TRANSFER

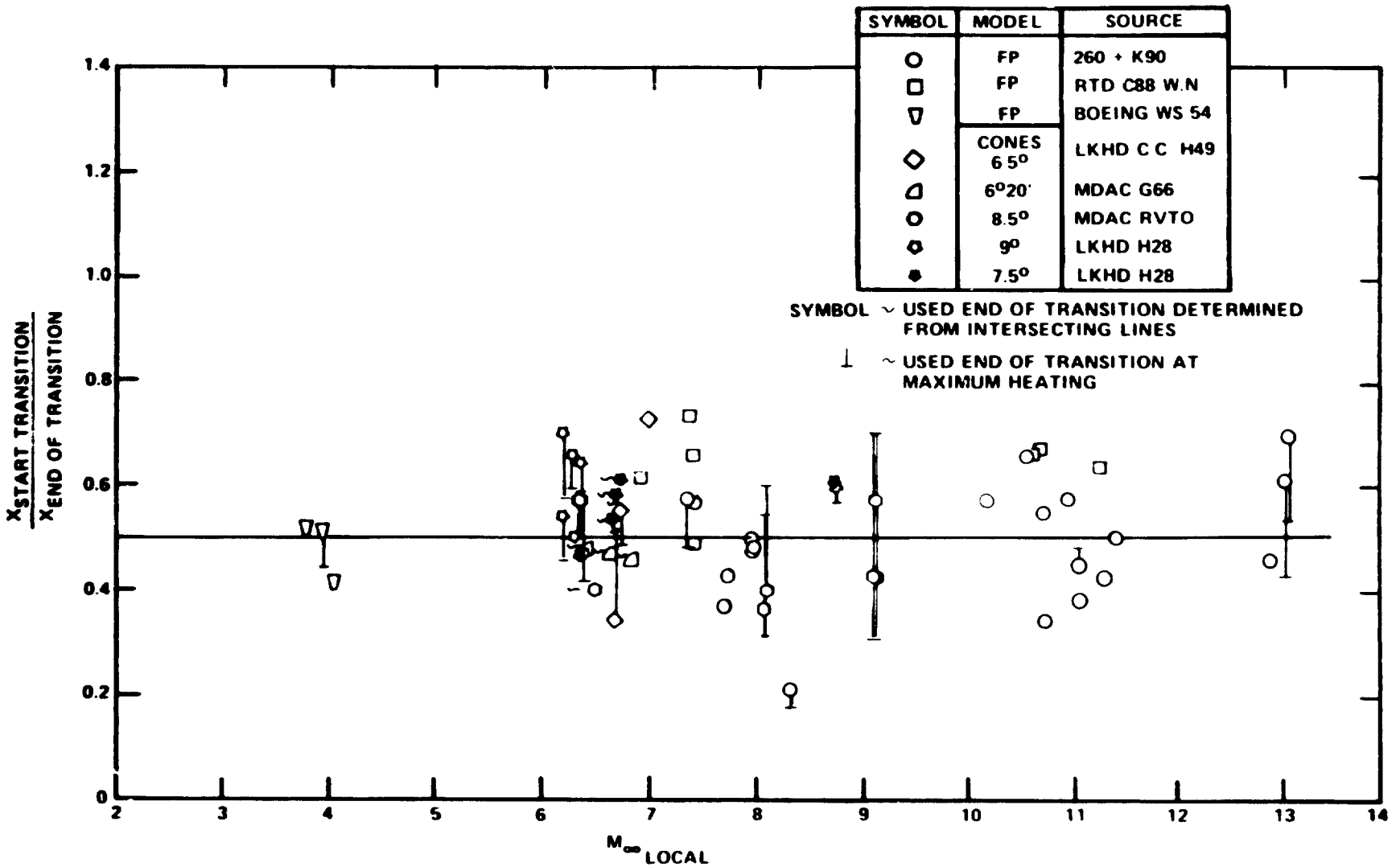

Figure 9 CORRELATION OF THE SCALE LENGTH OF THE TRANSITION ON FLAT PLATES AND CONES

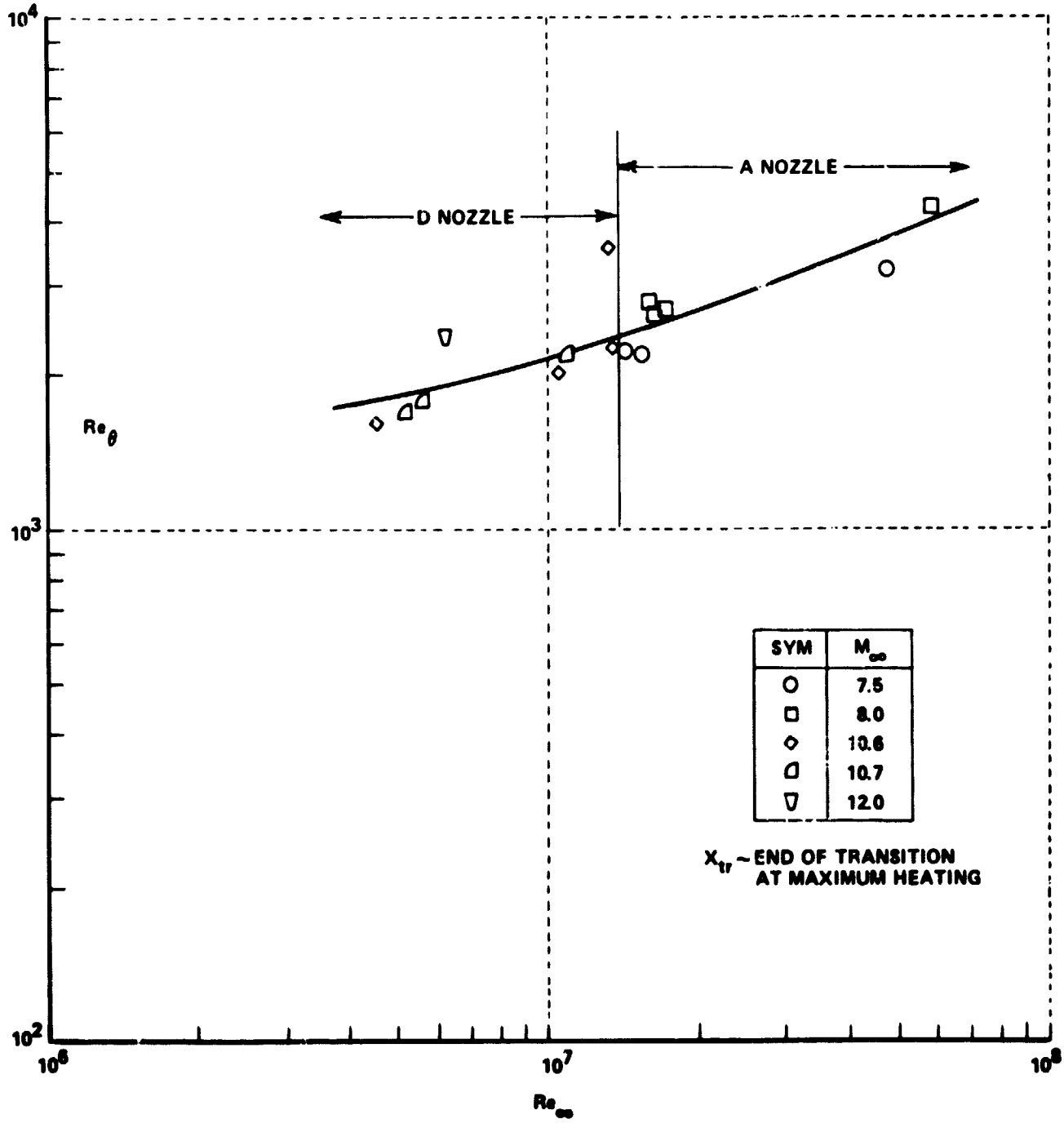

Figure 10 CORRELATION OF TRANSITION SHOWING THE EFFECTS OF TUNNEL SIZE

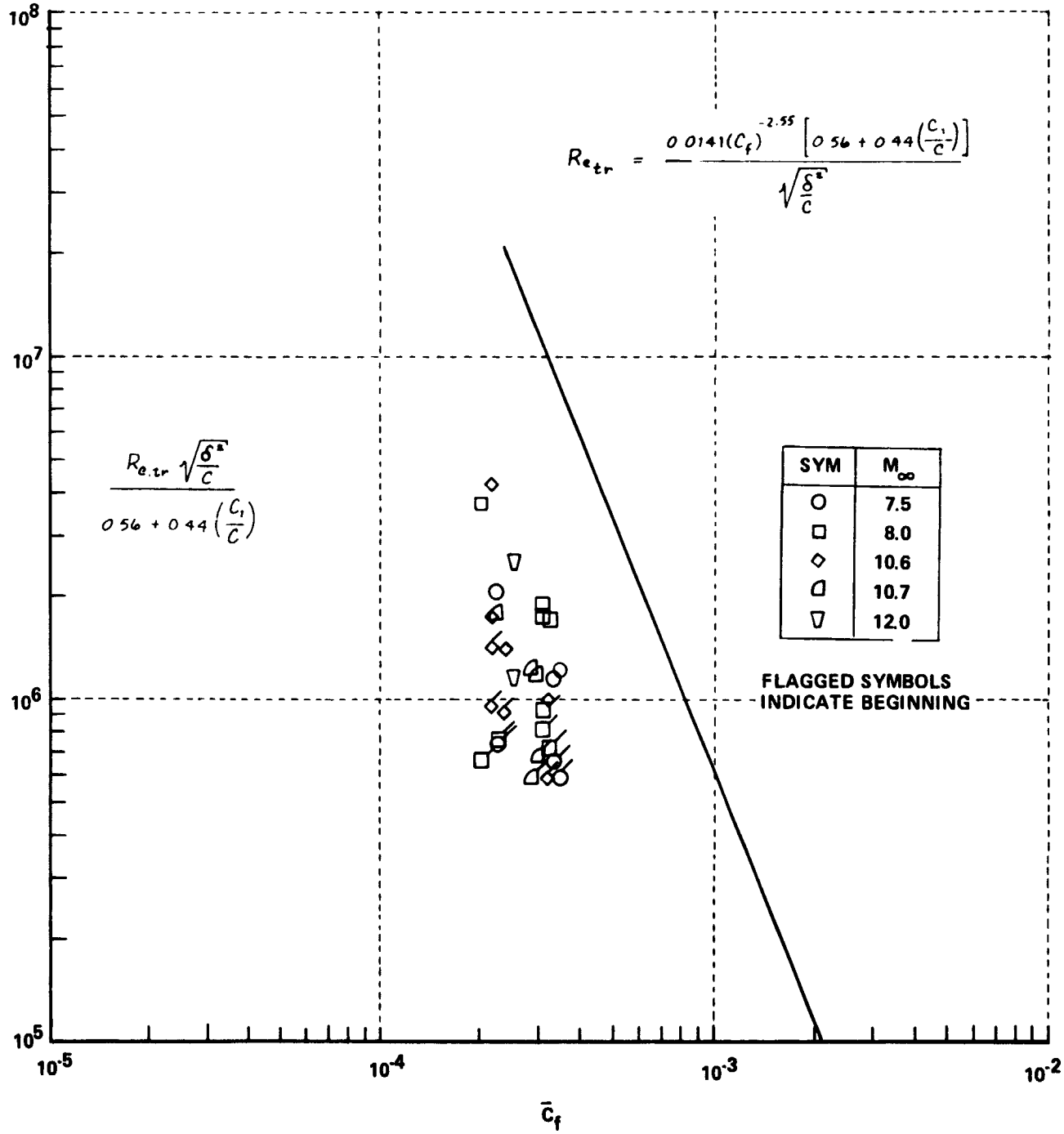

Figure 11 CORRELATION OF THE FLAT PLATE TRANSITION DATA IN TERMS OF THE PARAMETERS SUGGESTED BY PATE AND SCHUELERS

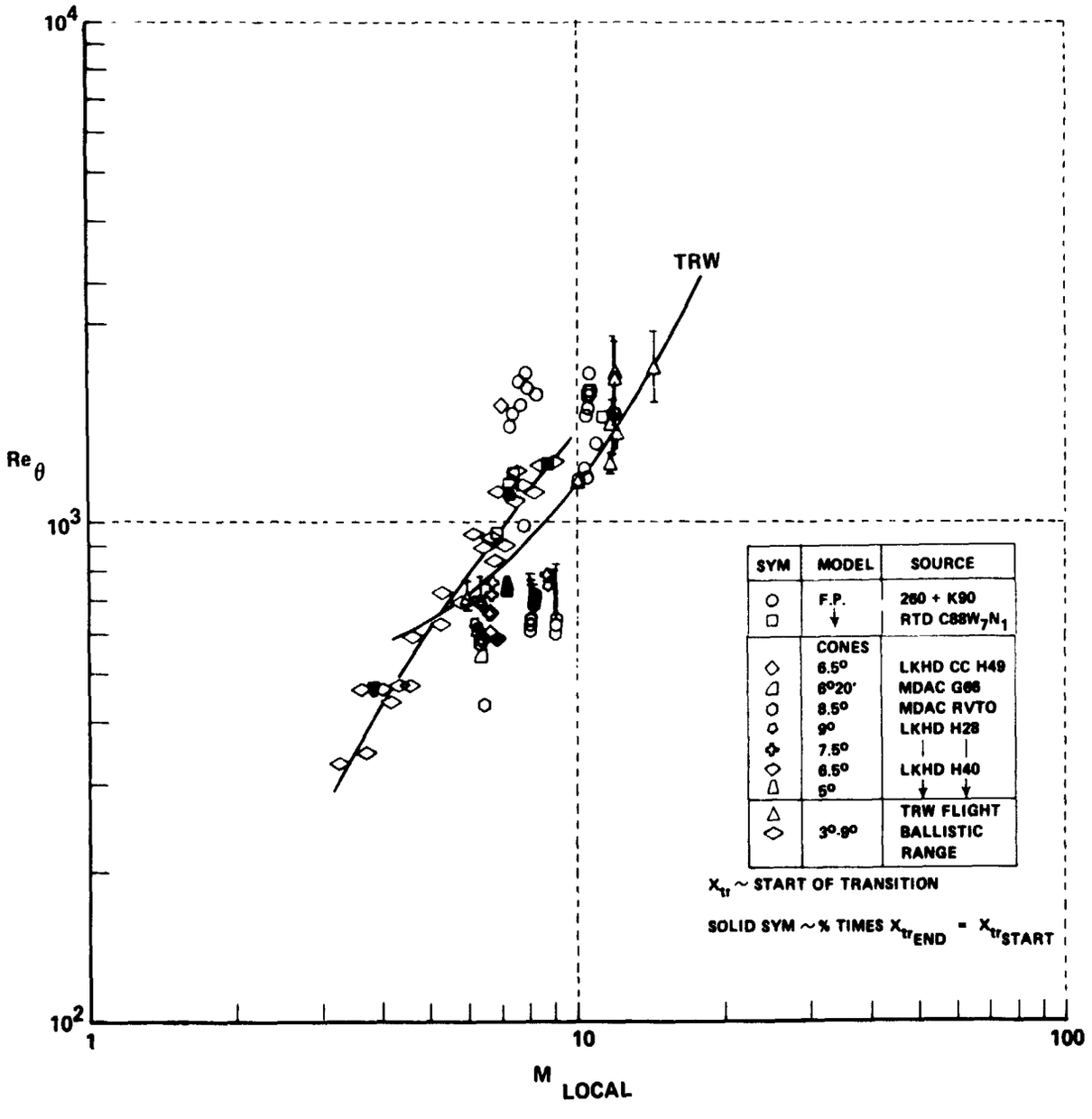

Figure 12 CORRELATION OF TRANSITION MEASUREMENTS IN THE CAL SHOCK TUNNELS WITH BALLISTIC AND DOWNRANGE MEASUREMENTS

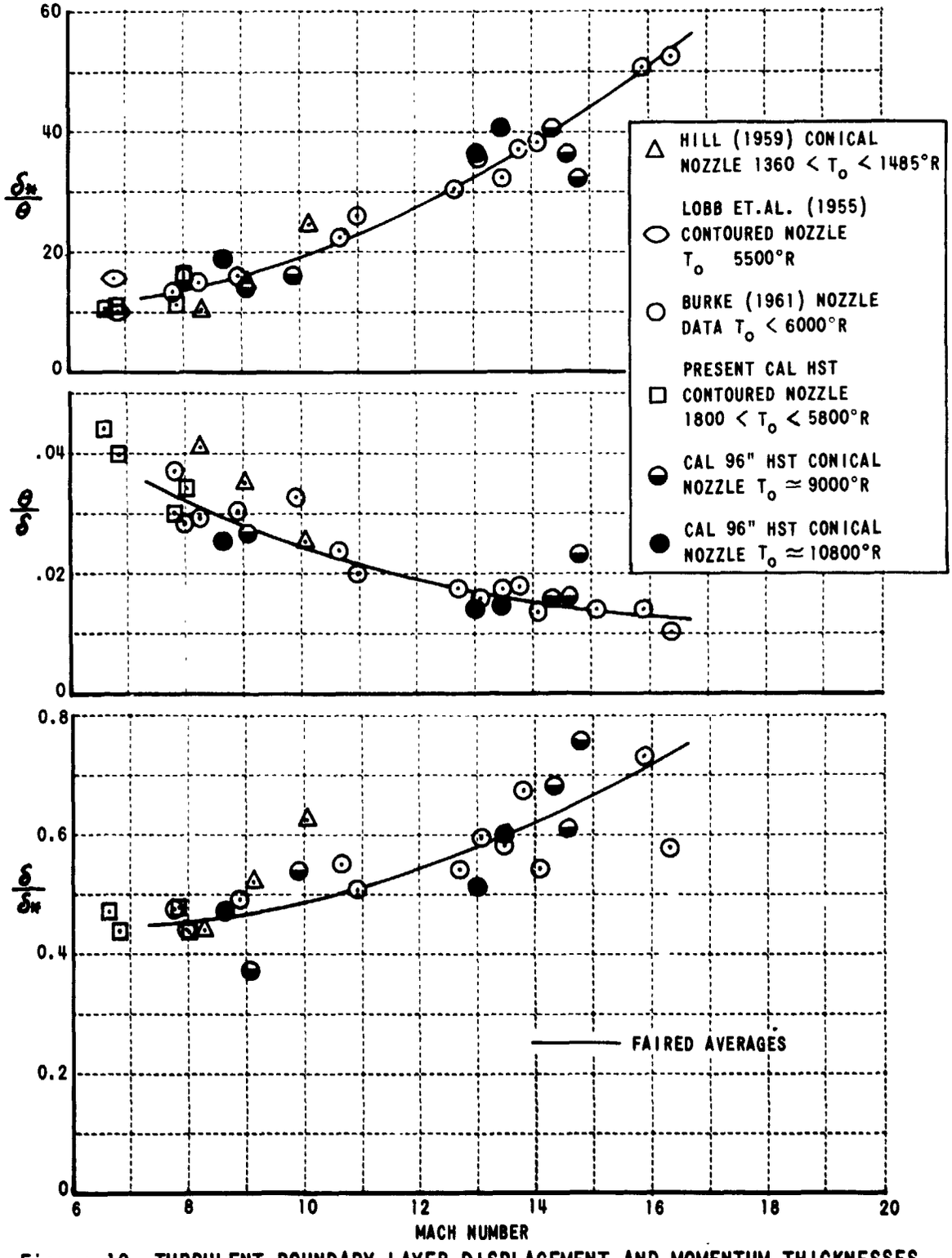

Figure 13 TURBULENT BOUNDARY LAYER DISPLACEMENT AND MOMENTUM THICKNESSES FROM SHOCK TUNNEL NOZZLE DATA

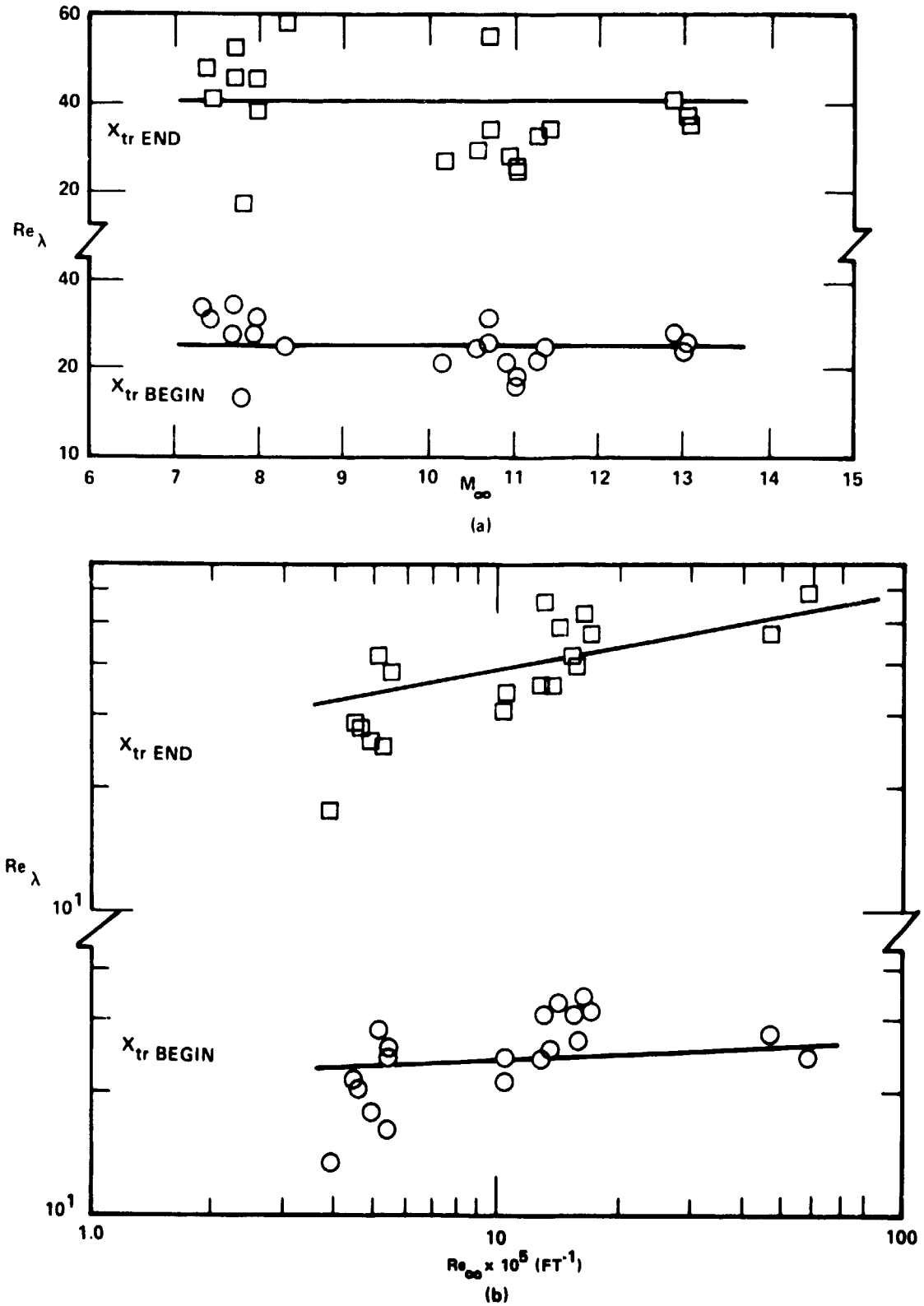

Figure 14 CORRELATION OF THE EDDY REYNOLDS NUMBER WITH TRANSITION MEASUREMENTS ON THE FLAT PLATES

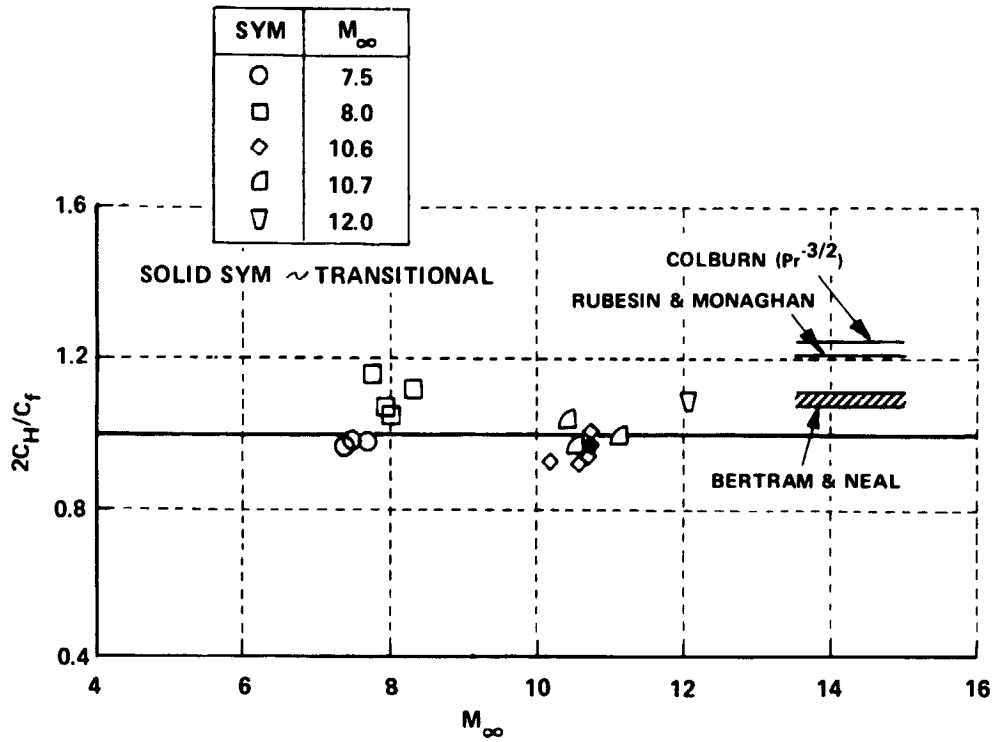

Figure 15 REYNOLDS ANALOGY FACTORS FOR TURBULENT HYPERSONIC BOUNDARY LAYERS

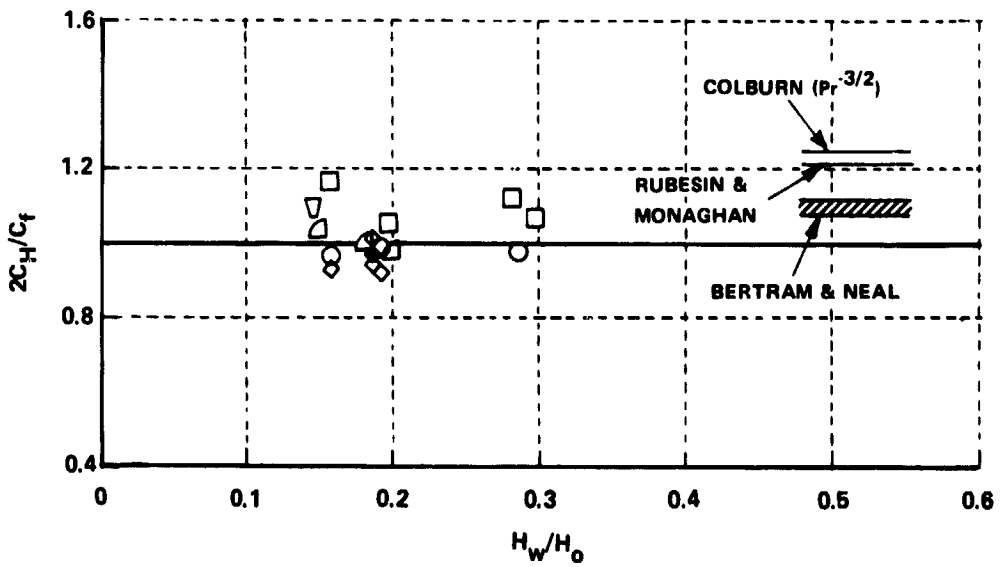

Figure 16 REYNOLDS ANALOGY FACTORS FOR TURBULENT HYPERSONIC BOUNDARY LAYERS

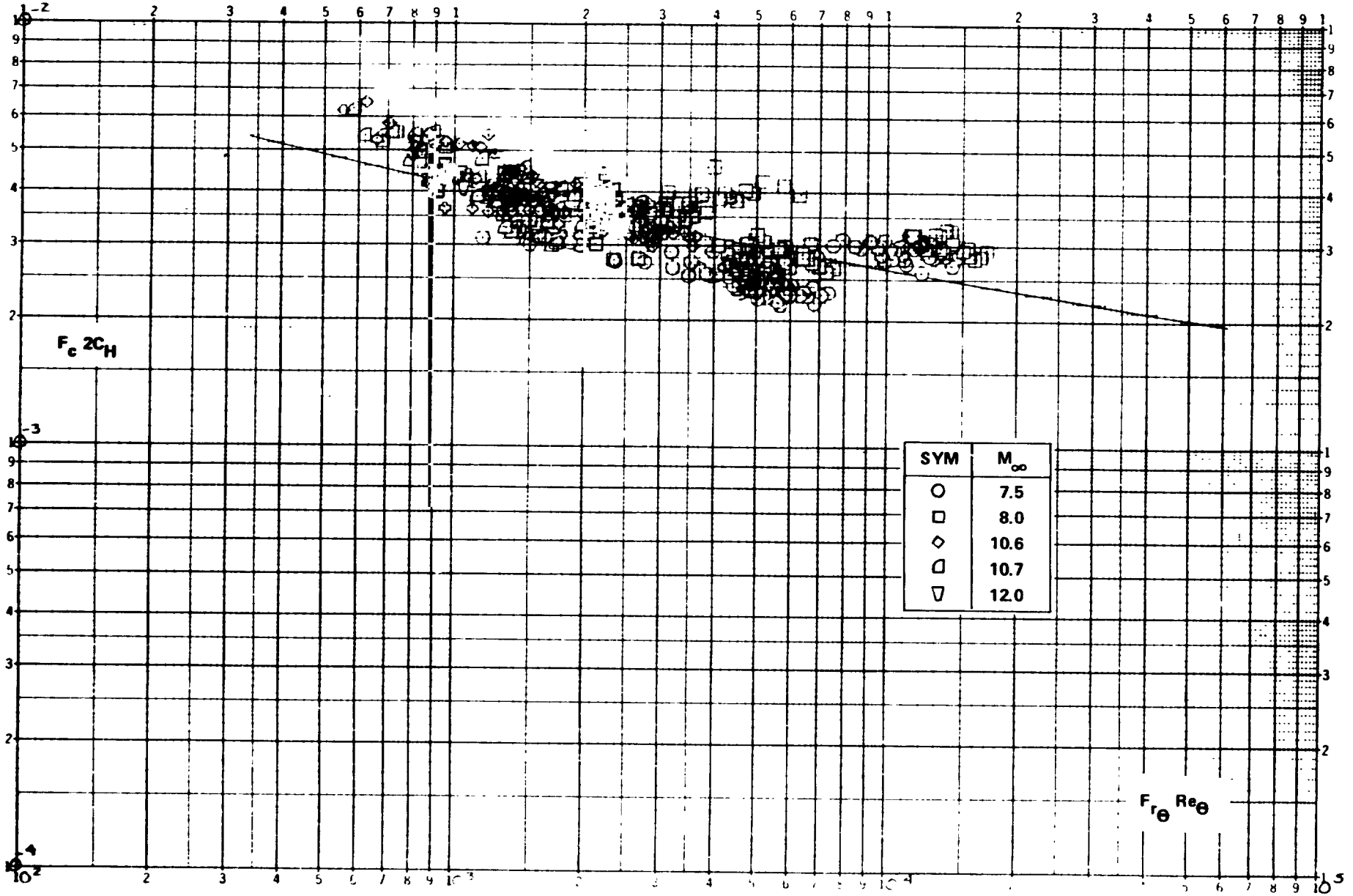

Figure 17a COMPARISON BETWEEN THE MEASURED HEAT TRANSFER AND THE THEORY OF ECKERT (T_A^*)

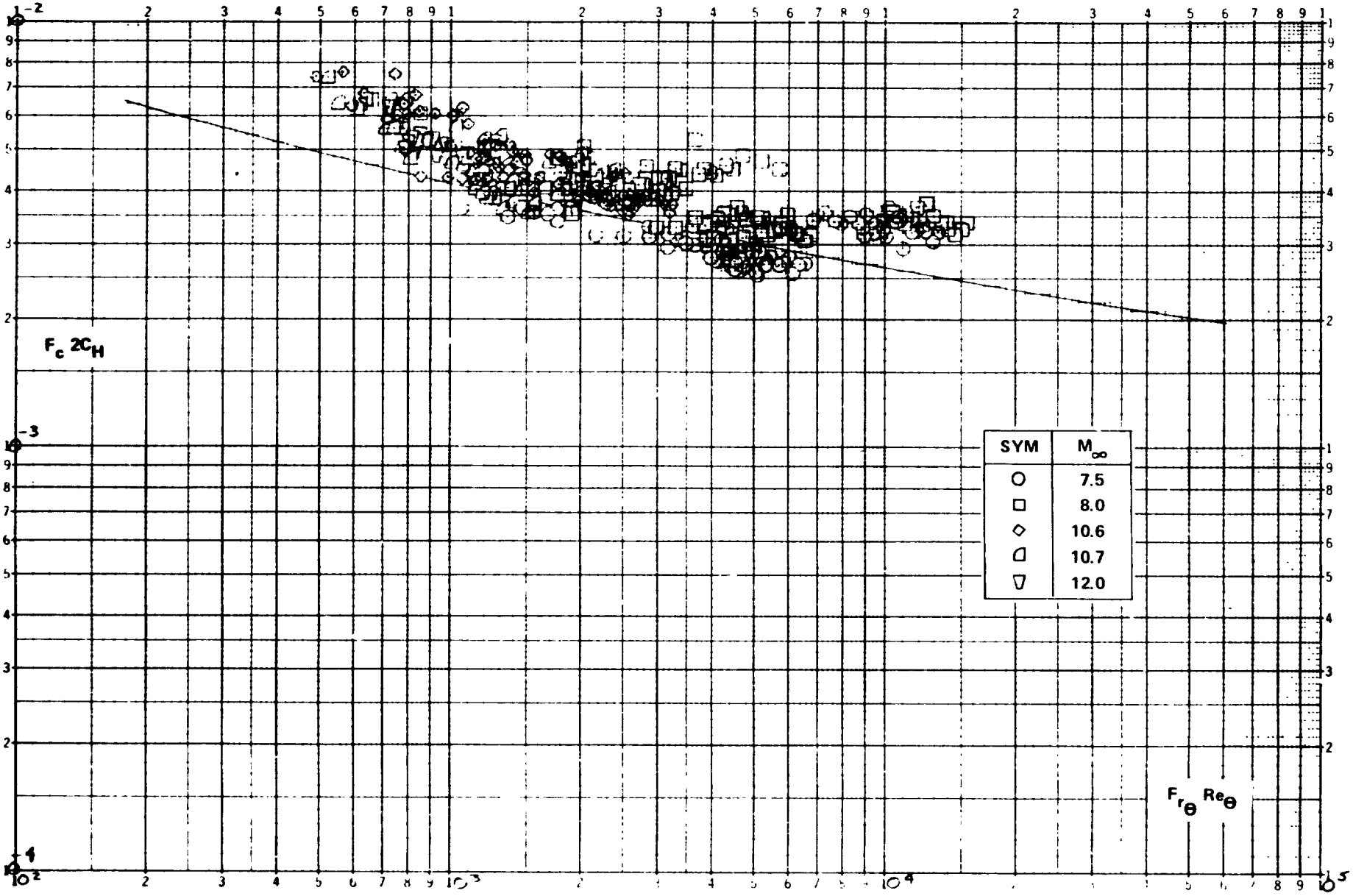

Figure 17b COMPARISON BETWEEN THE MEASURED HEAT TRANSFER AND THE THEORY OF ECKERT (T_E*)

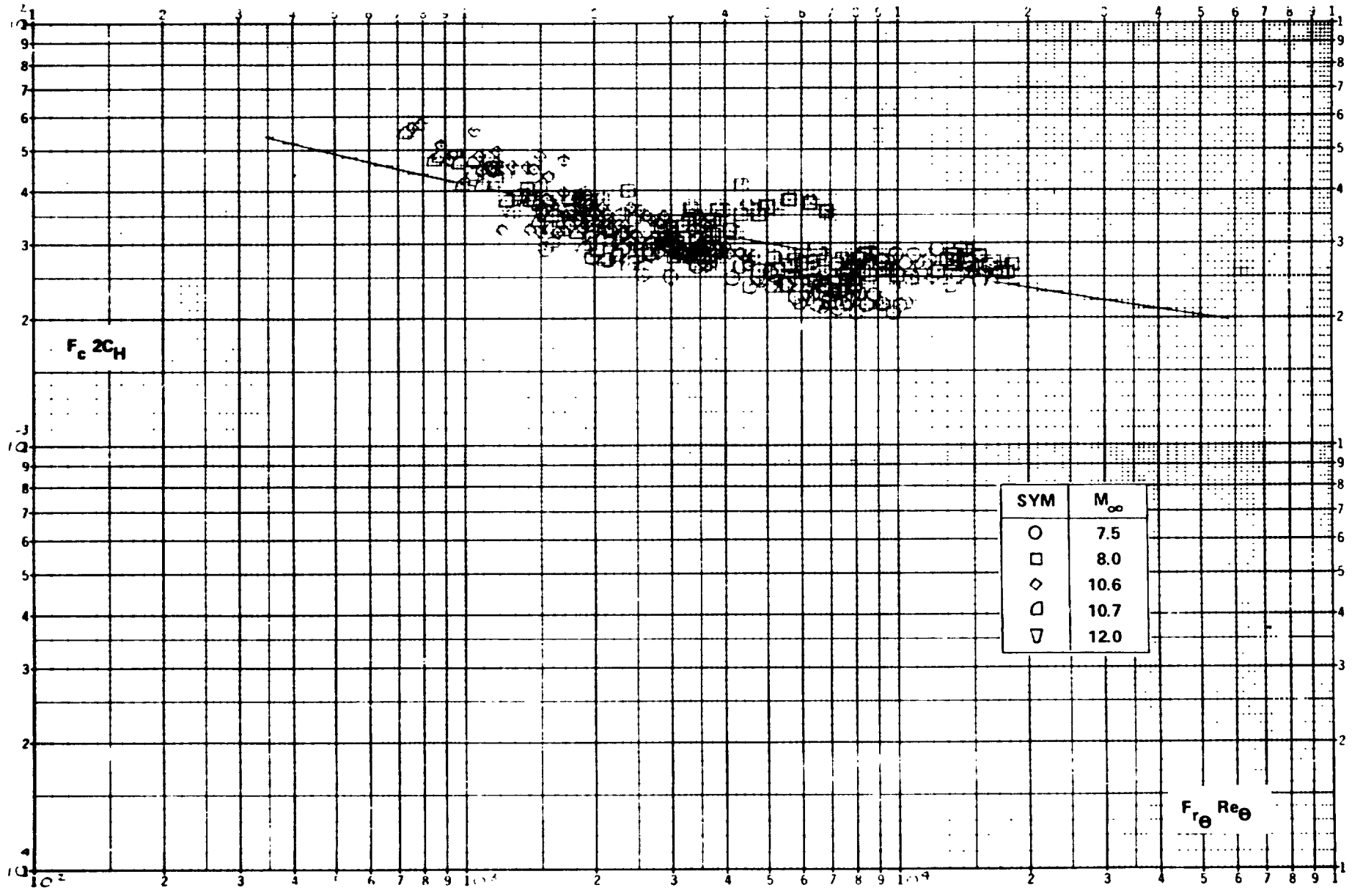

Figure 17c COMPARISON BETWEEN THE MEASURED HEAT TRANSFER AND THE THEORY OF VAN DRIEST

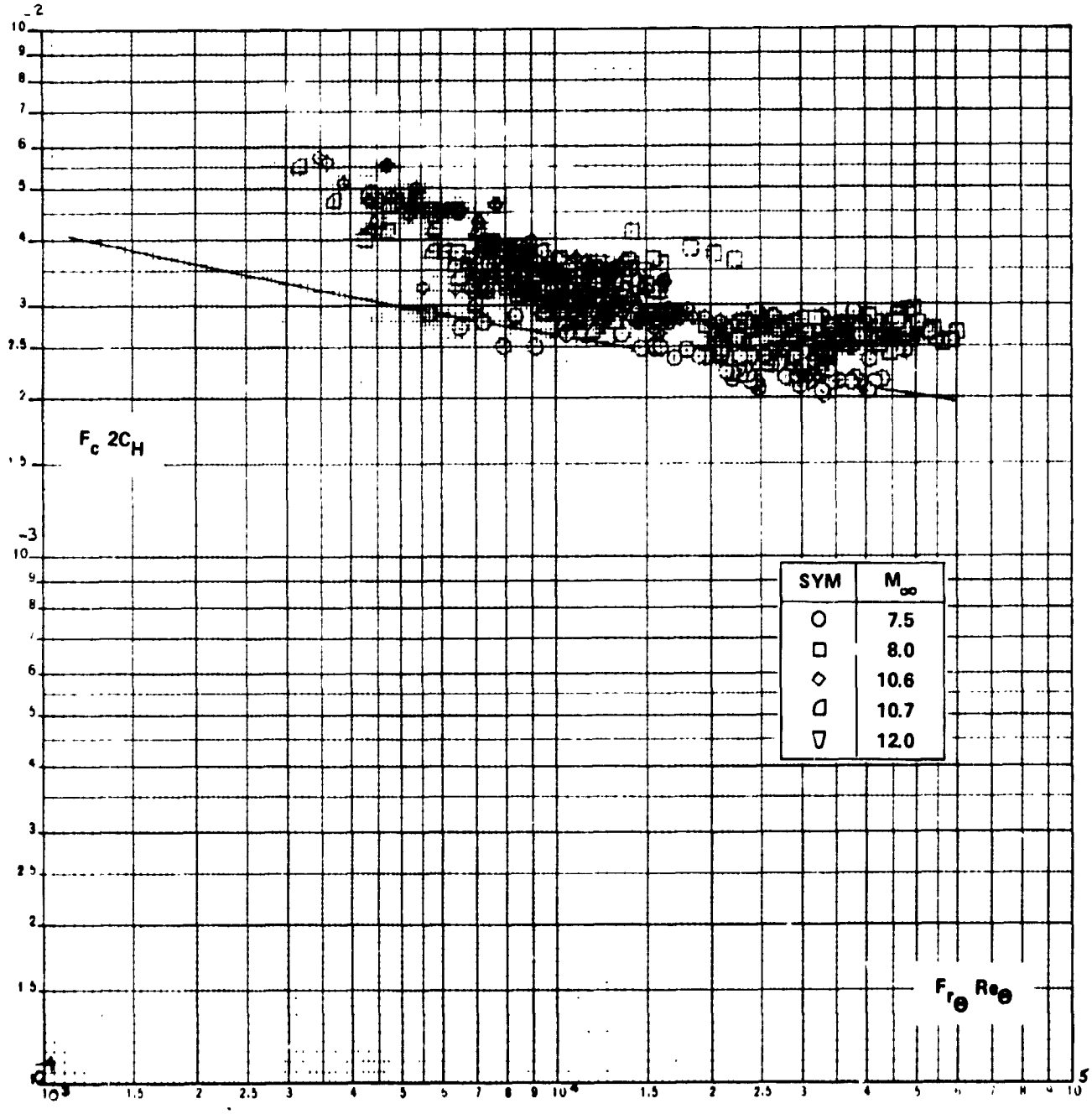

Figure 17d COMPARISON BETWEEN THE MEASURED HEAT TRANSFER AND THE SPALDING-CHI THEORY

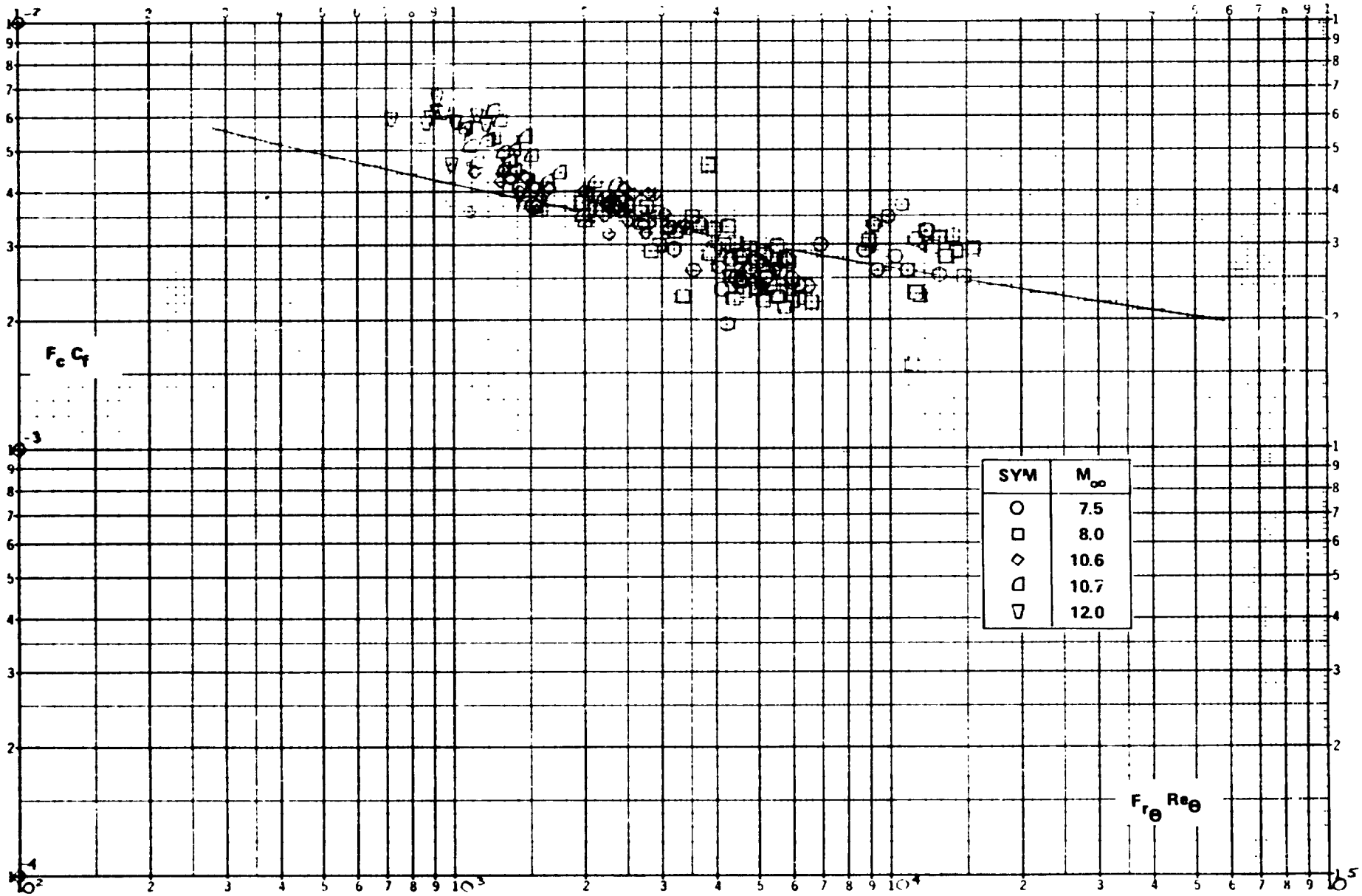

Figure 18a COMPARISON BETWEEN THE MEASURED SKIN FRICTION AND THE THEORY OF ECKERT (T_A^*)

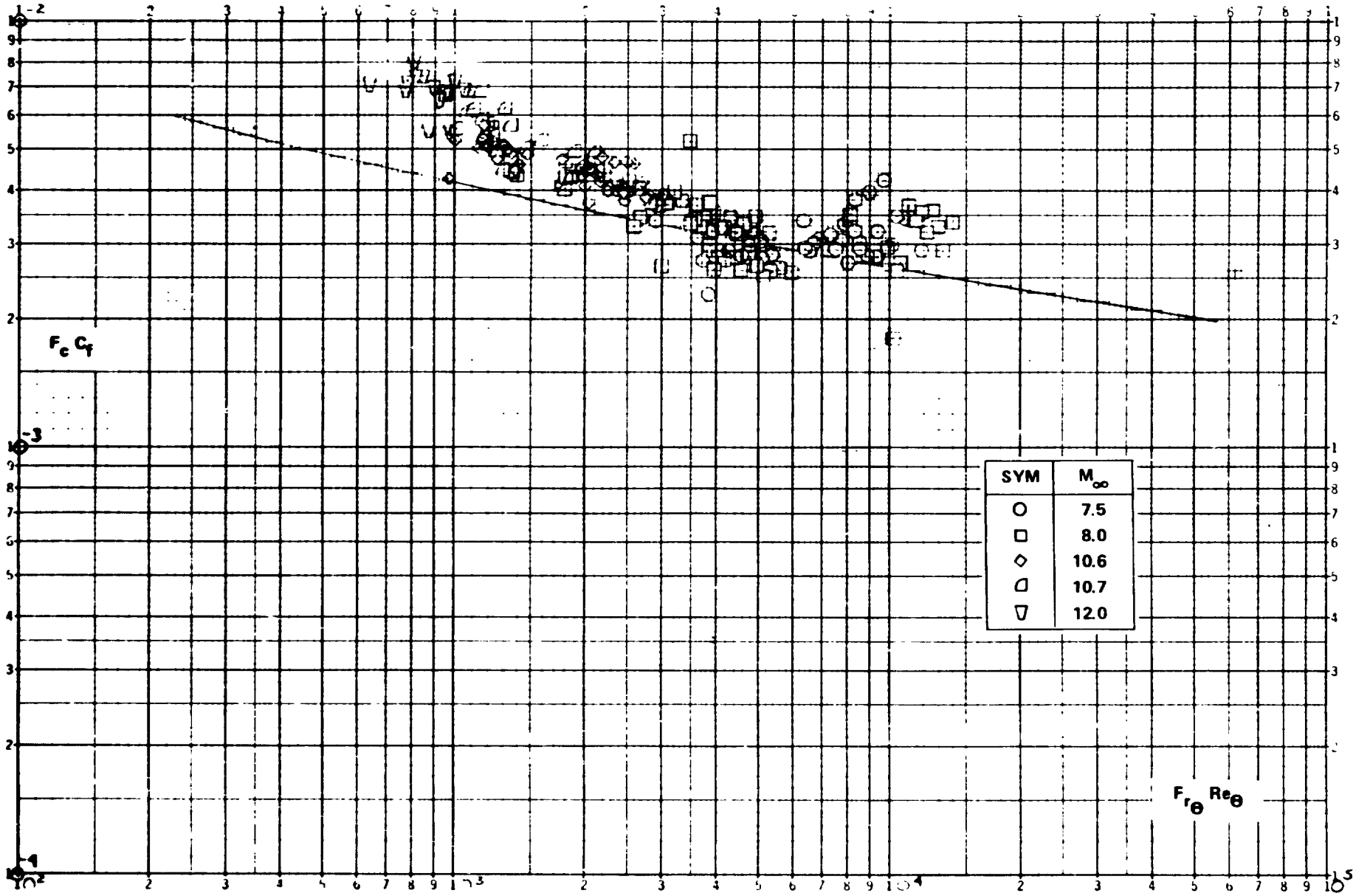

Figure 18b COMPARISON BETWEEN THE MEASURED SKIN FRICTION AND THE THEORY OF ECKERT (T_E^*)

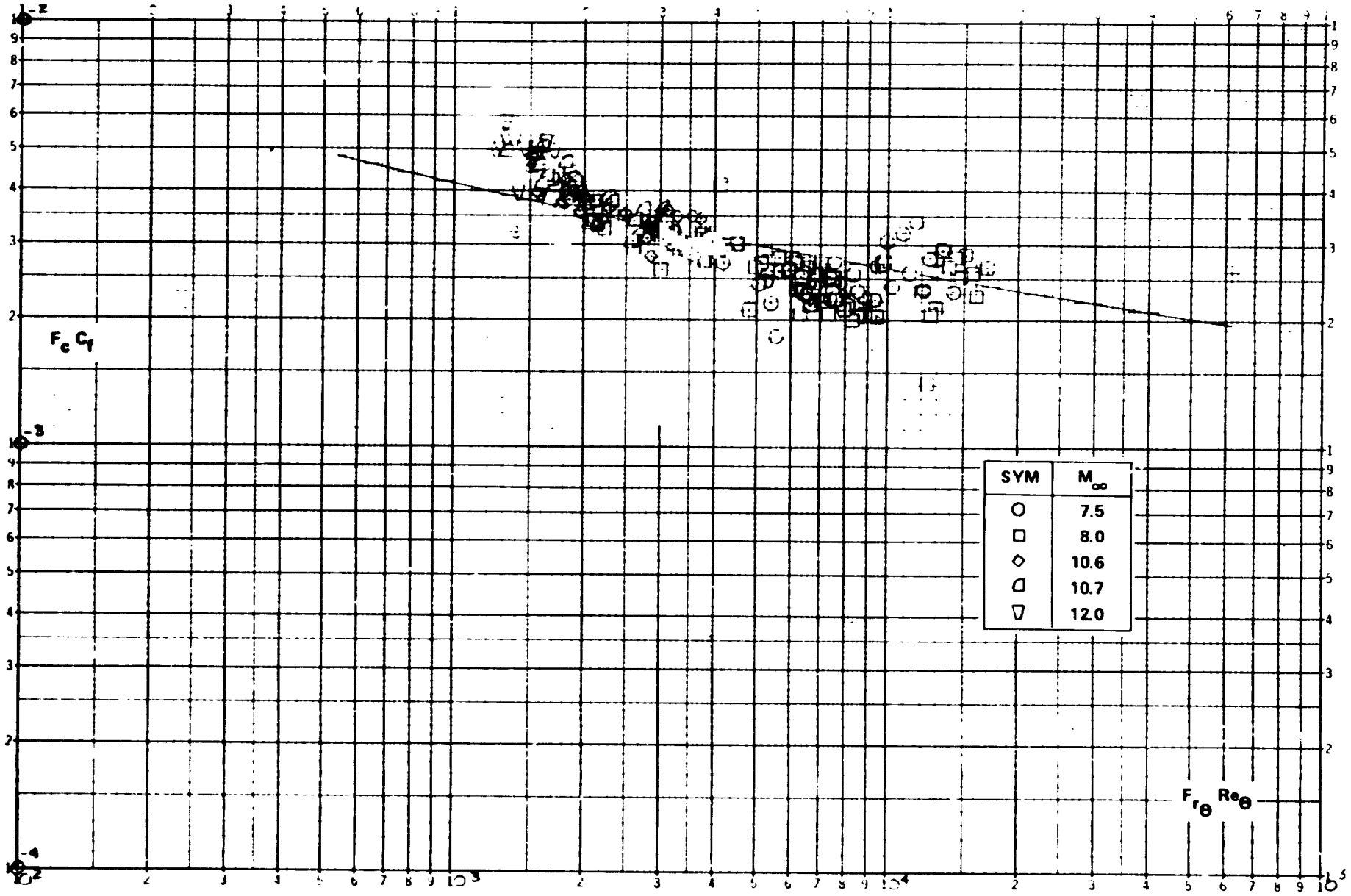

Figure 18c COMPARISON BETWEEN THE MEASURED SKIN FRICTION AND THE THEORY OF VAN DRIEST

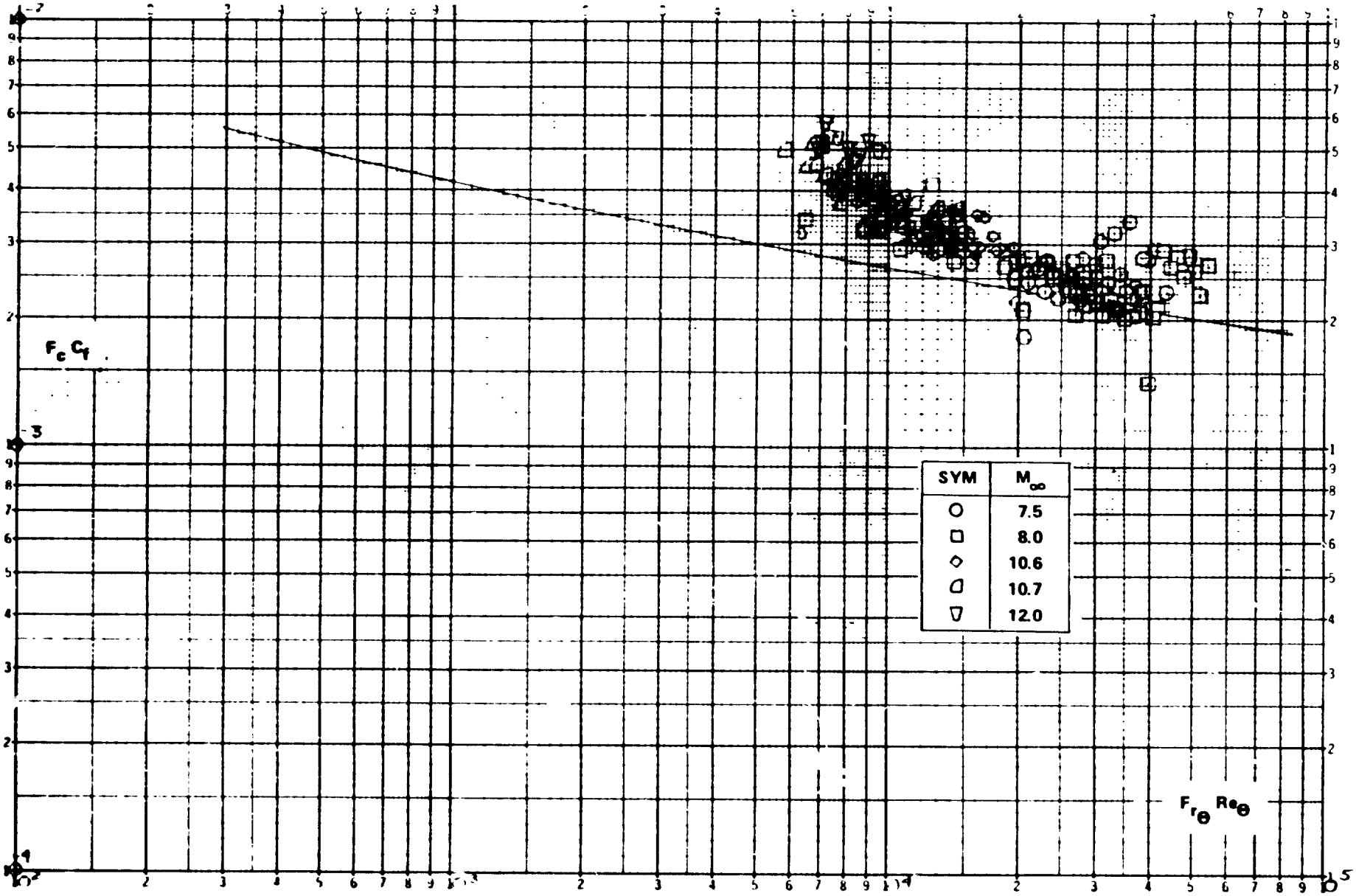

Figure 18d COMPARISON BETWEEN THE MEASURED SKIN FRICTION AND THE SPALDING-CHI THEORY

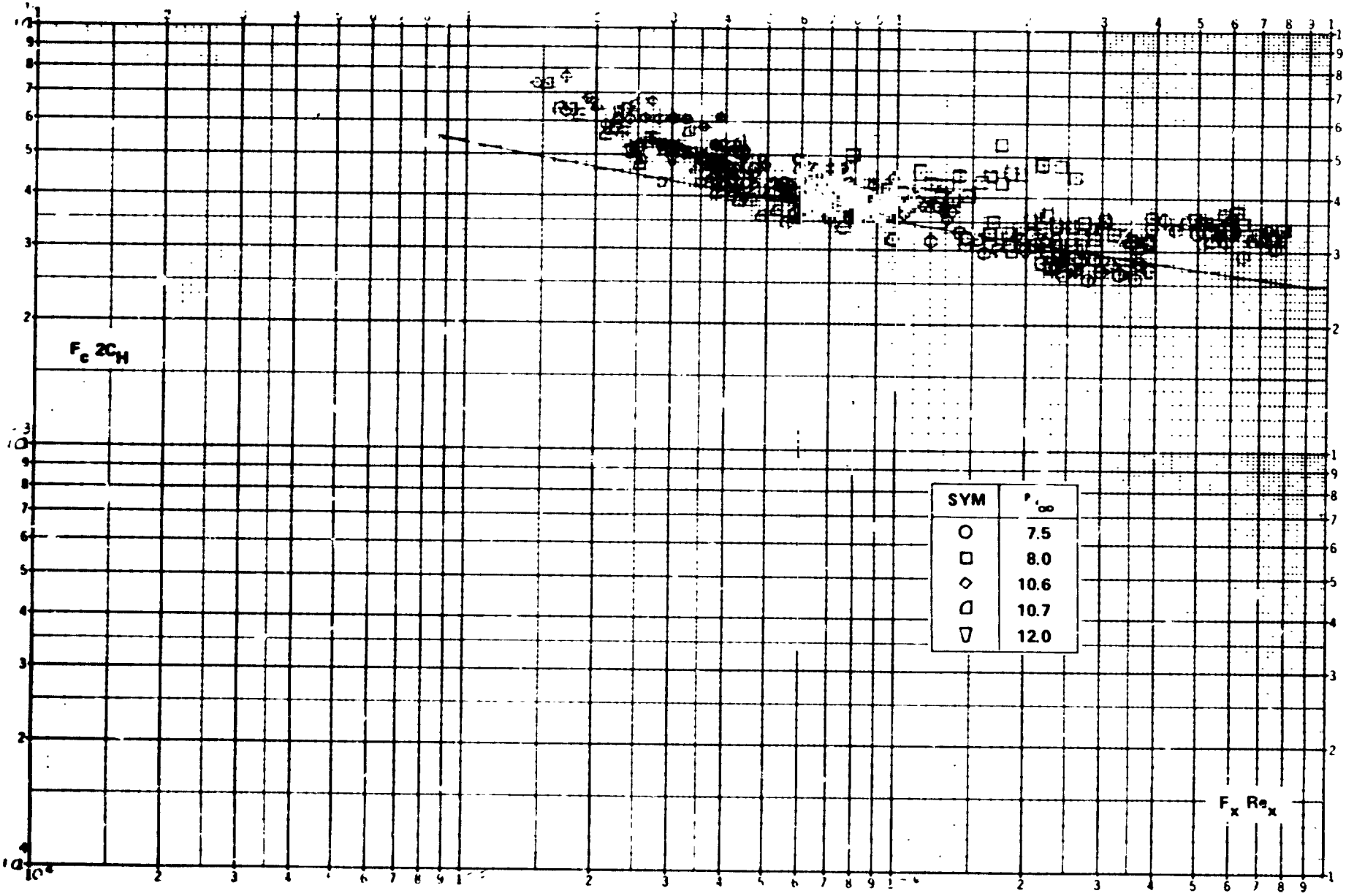

Figure 19a COMPARISON BETWEEN THE MEASURED HEAT TRANSFER AND THE THEORY OF ECKERT $(\Theta_V - \Theta_B + \Theta_{BE})$

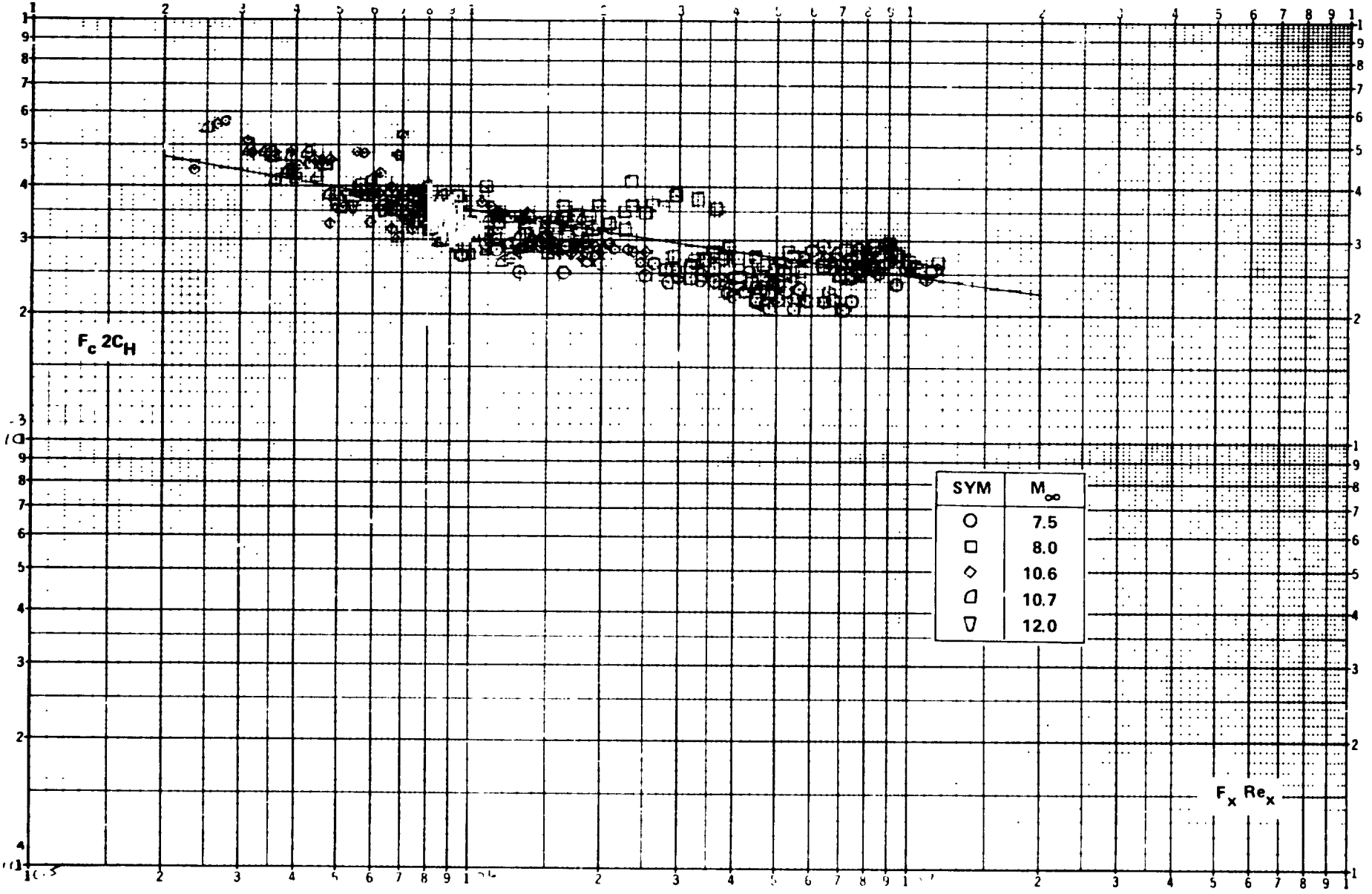

Figure 19b COMPARISON BETWEEN THE MEASURED HEAT TRANSFER AND THE THEORY OF VAN DRIEST ($\Theta_V = \Theta_B + \Theta_{BE}$)

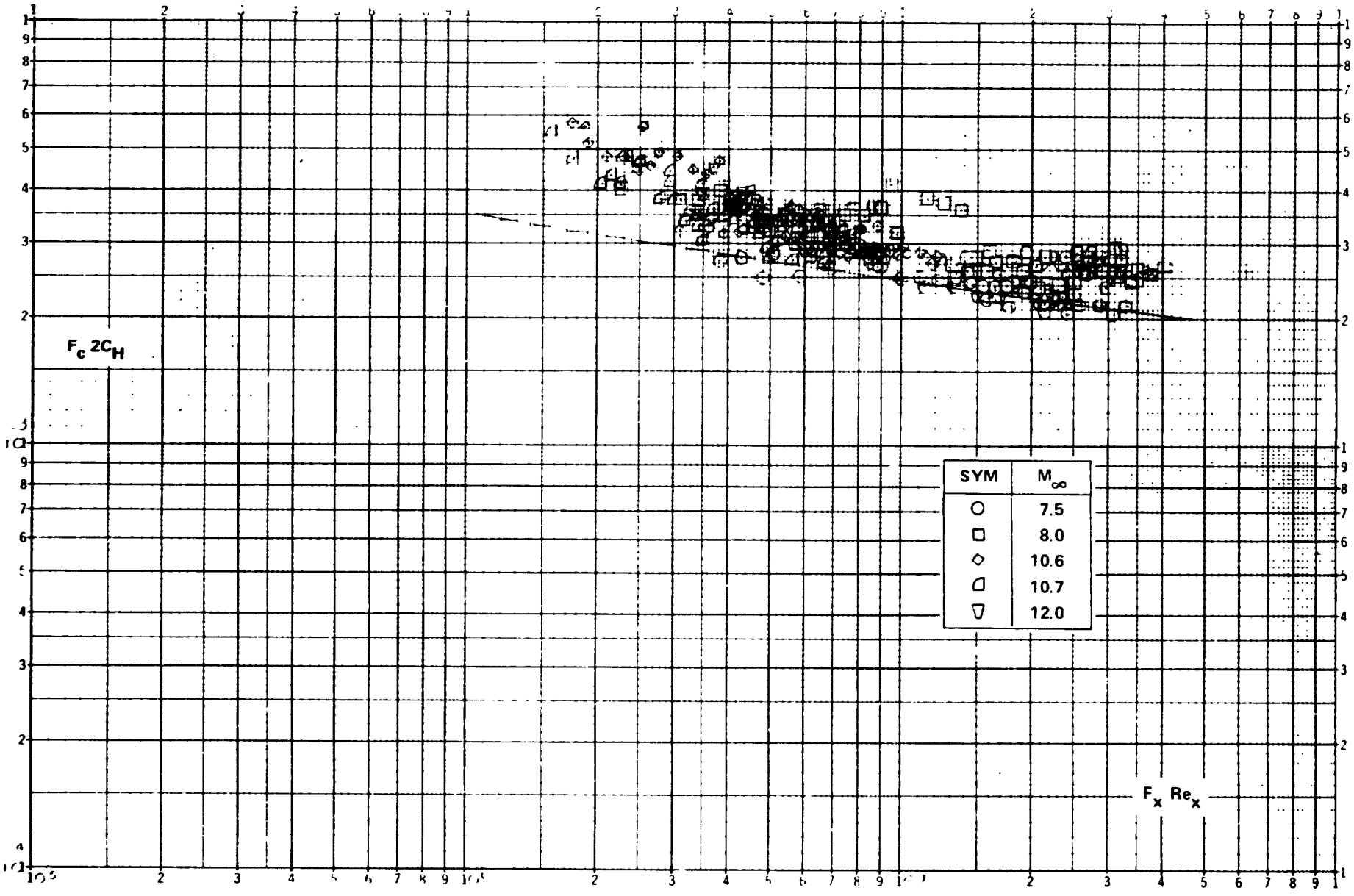

Figure 19c COMPARISON BETWEEN THE MEASURED HEAT TRANSFER AND THE SPALDING-CHI THEORY ($\Theta_V = \Theta_B + \Theta_{BE}$)

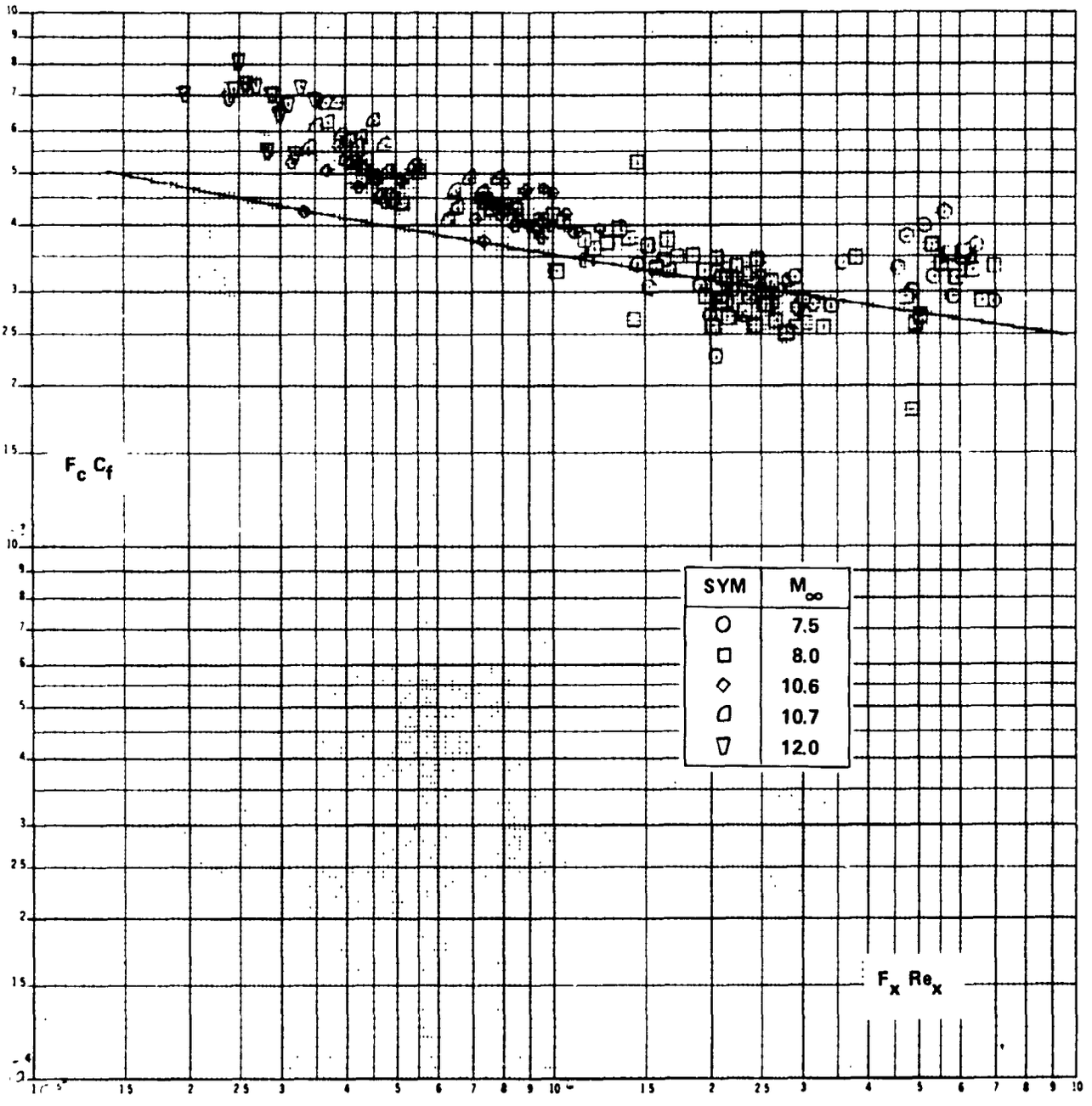

Figure 20a COMPARISON BETWEEN THE MEASURED SKIN FRICTION AND THE THEORY OF ECKERT ($\Theta_V = \Theta_B + \Theta_{BE}$)

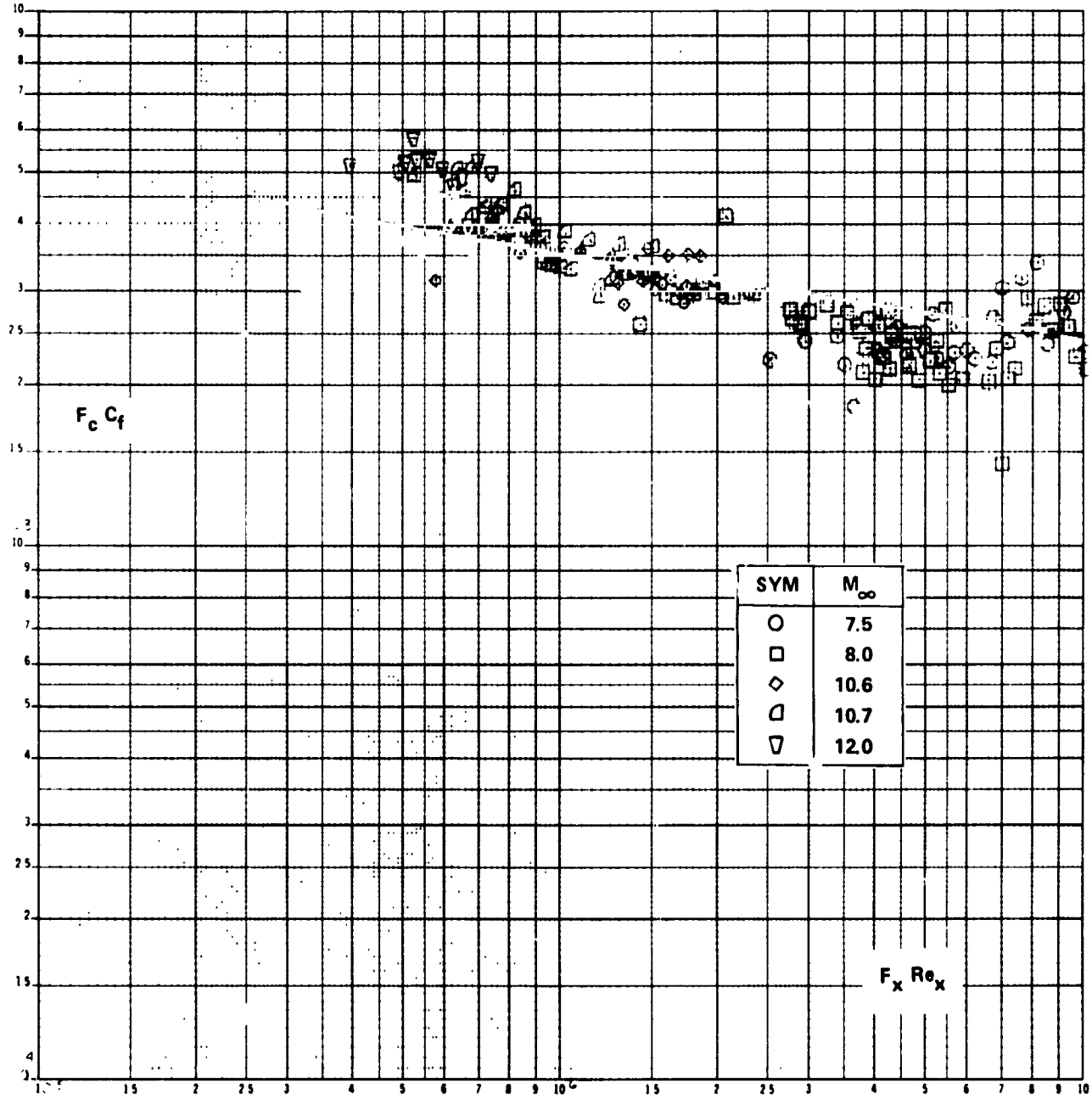

Figure 20b COMPARISON BETWEEN THE MEASURED SKIN FRICTION AND THE THEORY OF VAN DRIEST ($\theta_V = \theta_B + \theta_{BE}$)

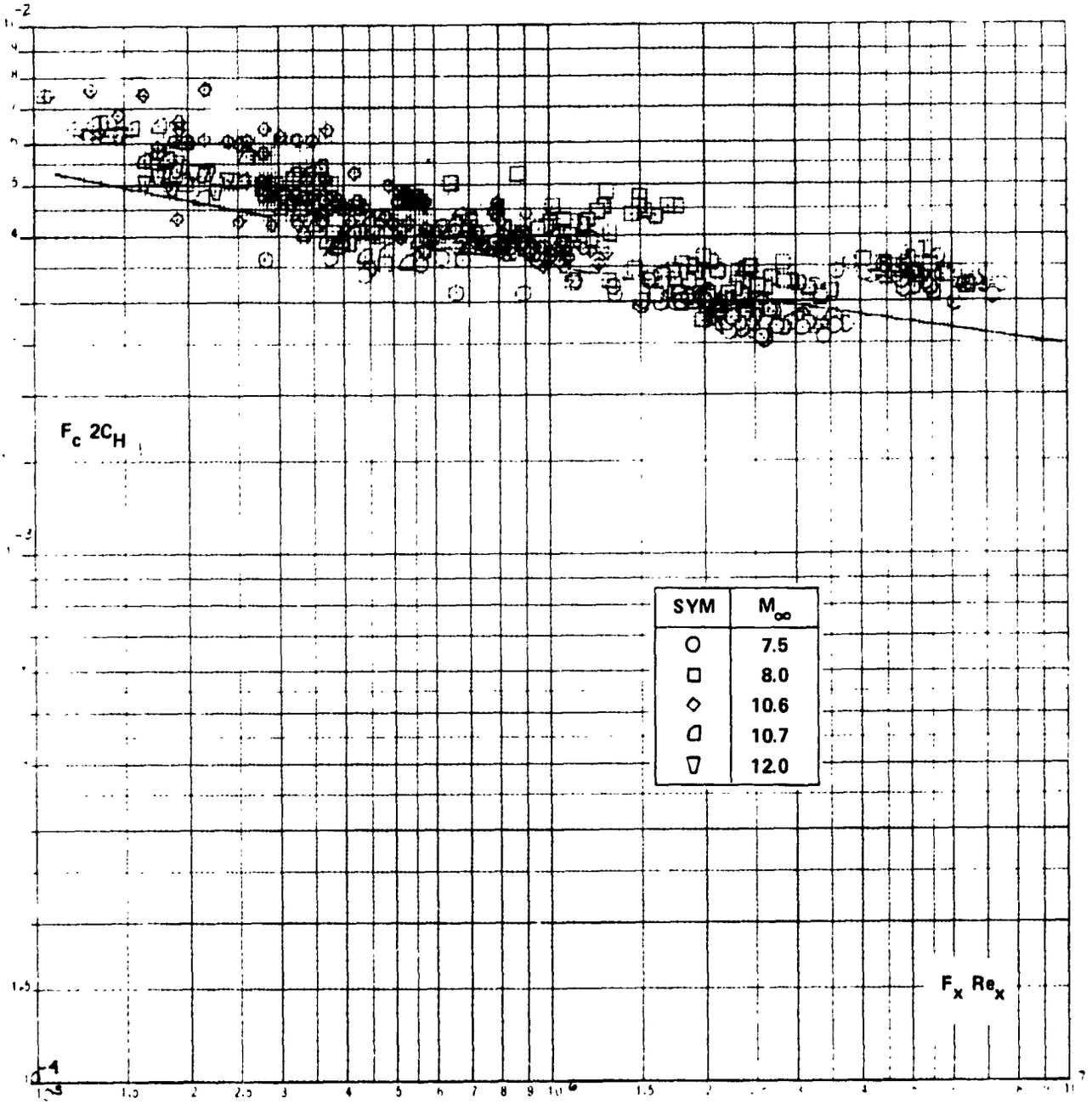

Figure 21a COMPARISON BETWEEN THE MEASURED HEAT TRANSFER AND THE THEORY OF ECKERT $(\Theta_V = \Theta_B + \Theta_{BE/2})$

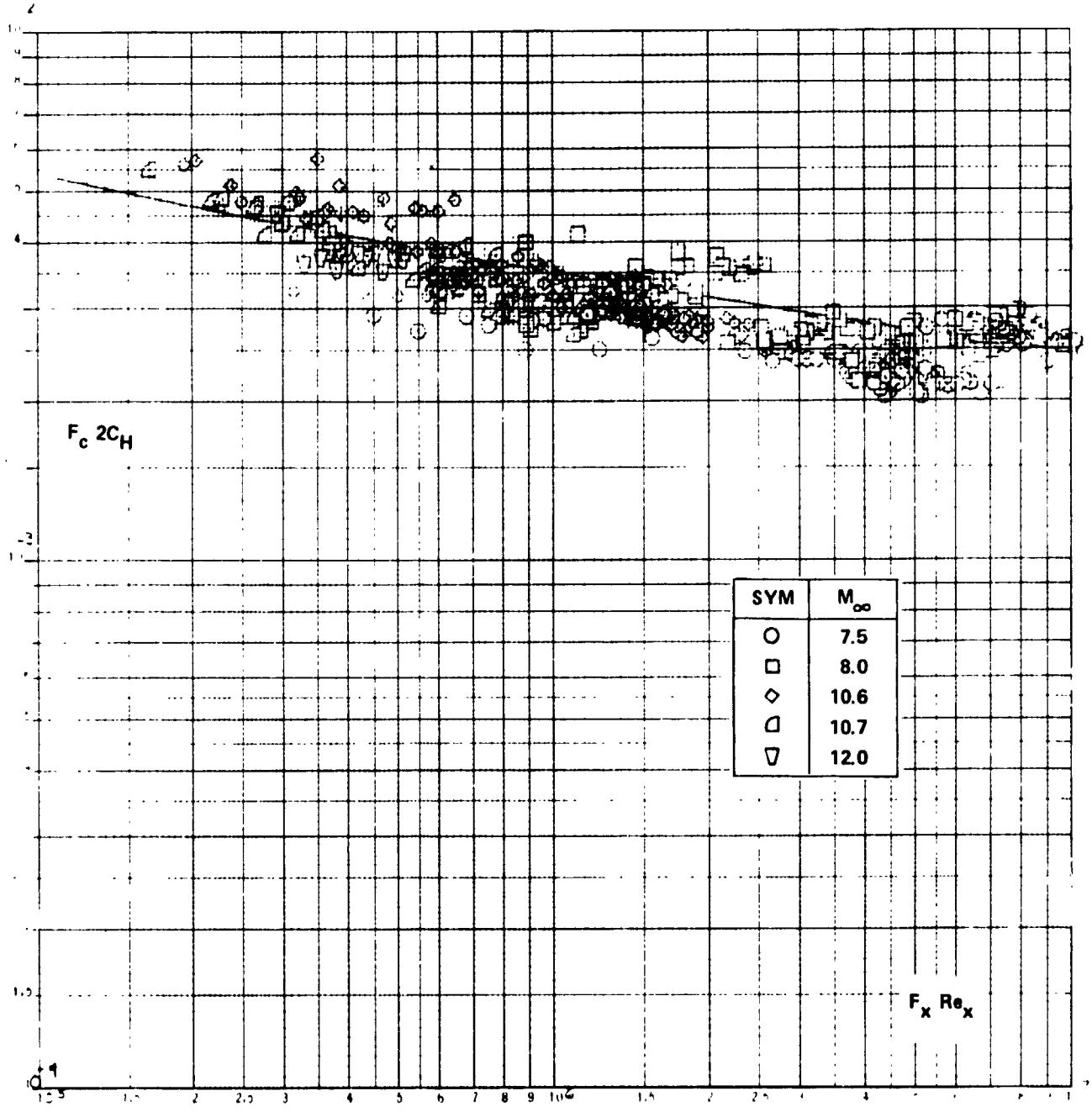

Figure 21b COMPARISON BETWEEN THE MEASURED HEAT TRANSFER AND THE THEORY OF VAN DRIEST $(\theta_V = \theta_B + \theta_{BE/2})$

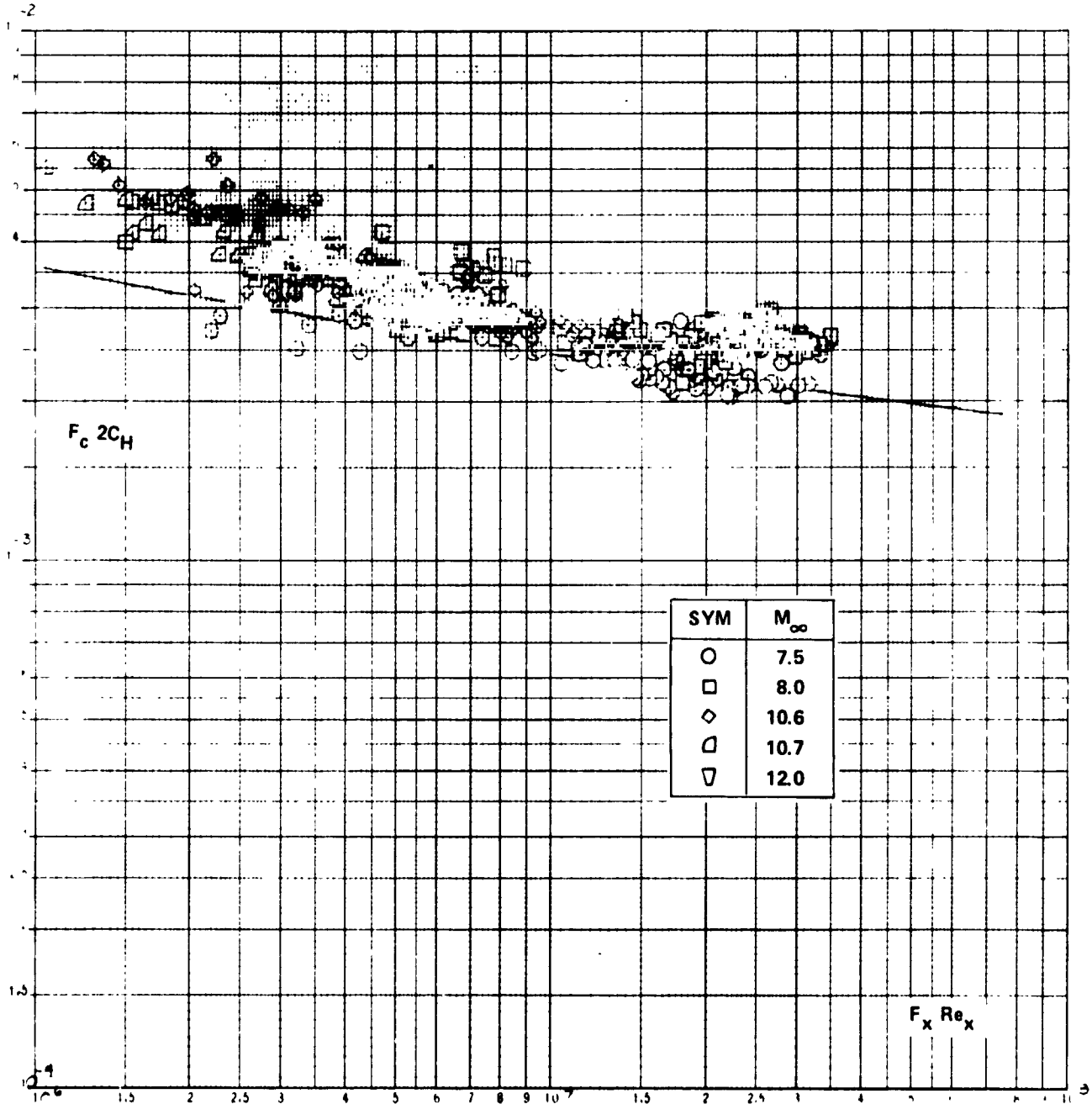

Figure 21c COMPARISON BETWEEN THE MEASURED HEAT TRANSFER AND THE SPALDING-CHI THEORY $(\Theta_V = \Theta_B + \Theta_{BE/2})$

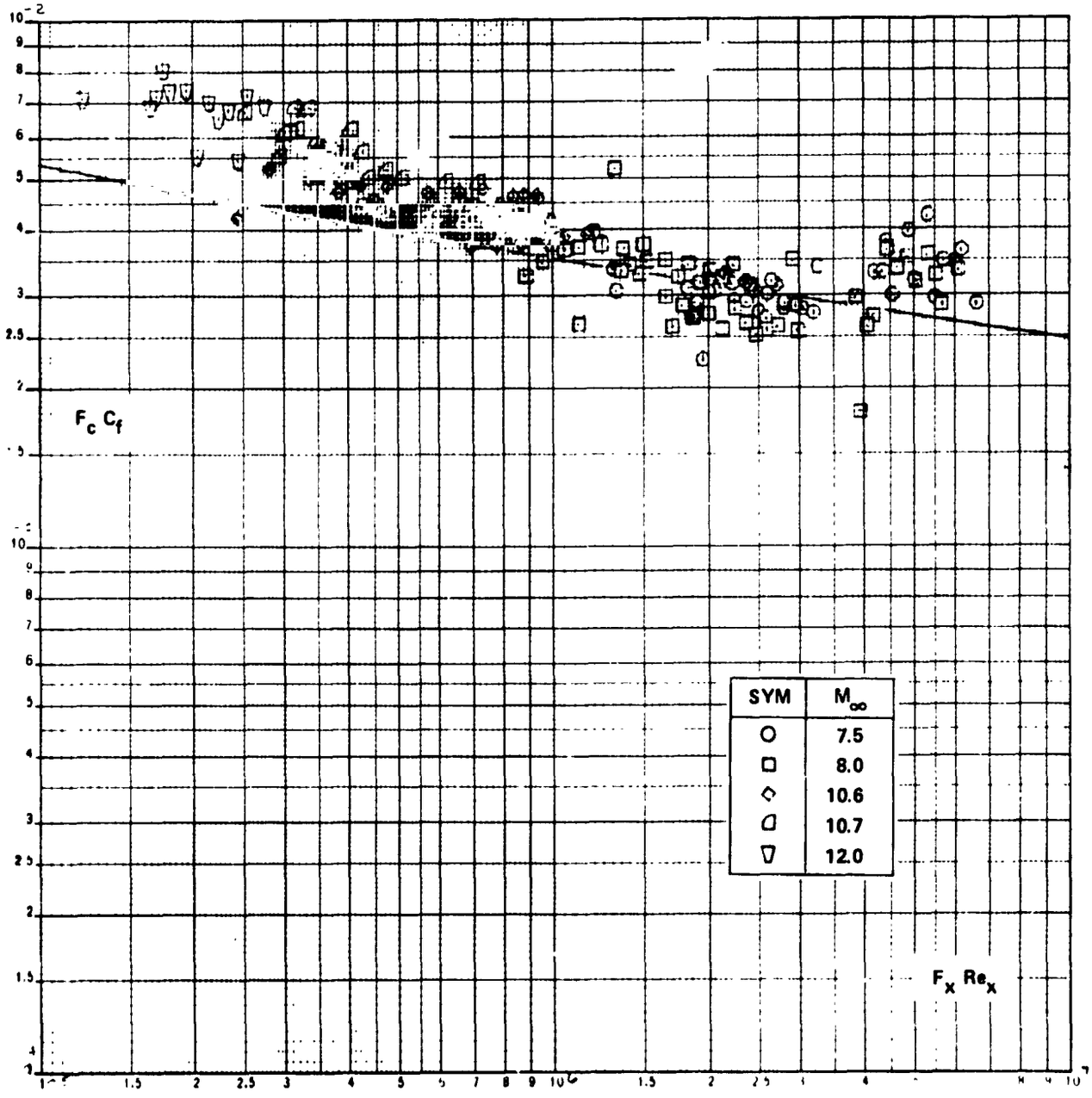

Figure 22a COMPARISON BETWEEN THE MEASURED SKIN FRICTION AND THE THEORY OF ECKERT $(\Theta_V = \Theta_B + \Theta_{BE/2})$

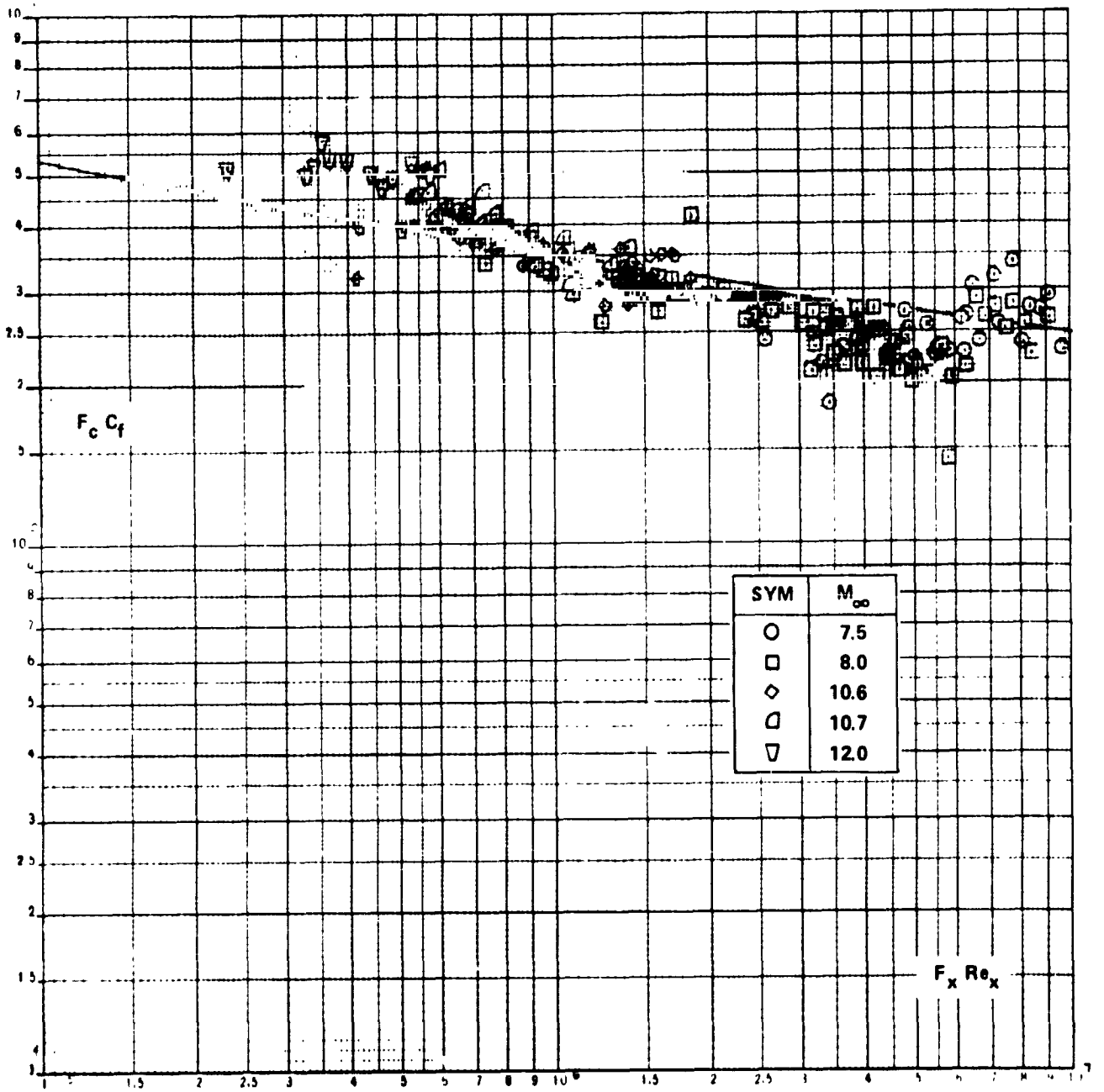

Figure 22b COMPARISON BETWEEN THE MEASURED SKIN FRICTION AND THE THEORY OF VAN DRIEST ($\Theta_V = \Theta_B + \Theta_{BE/2}$)

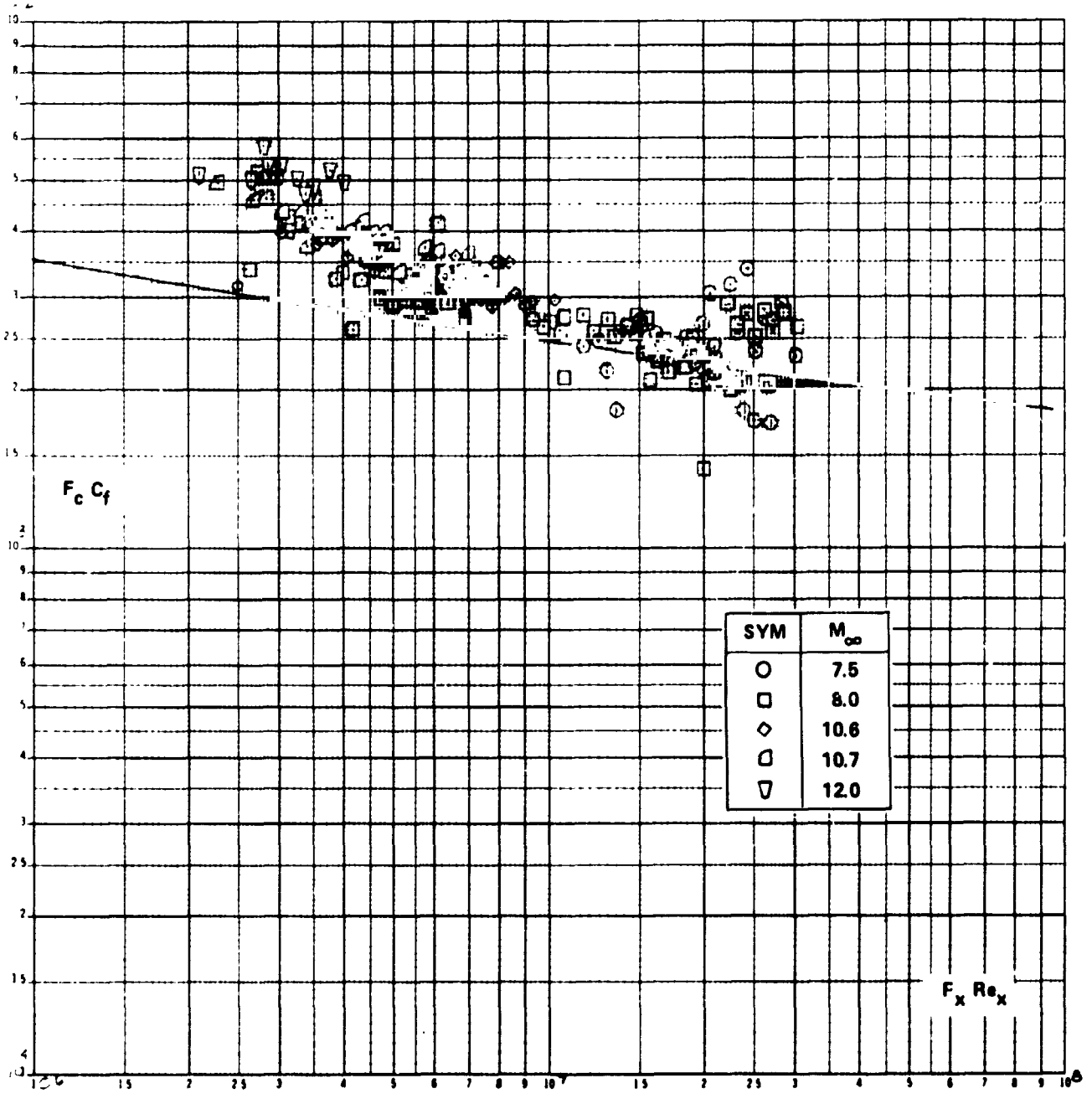

Figure 22c COMPARISON BETWEEN THE MEASURED SKIN FRICTION AND THE SPALDING-CHI THEORY ($\theta_V = \theta_B + \theta_{BE/2}$)

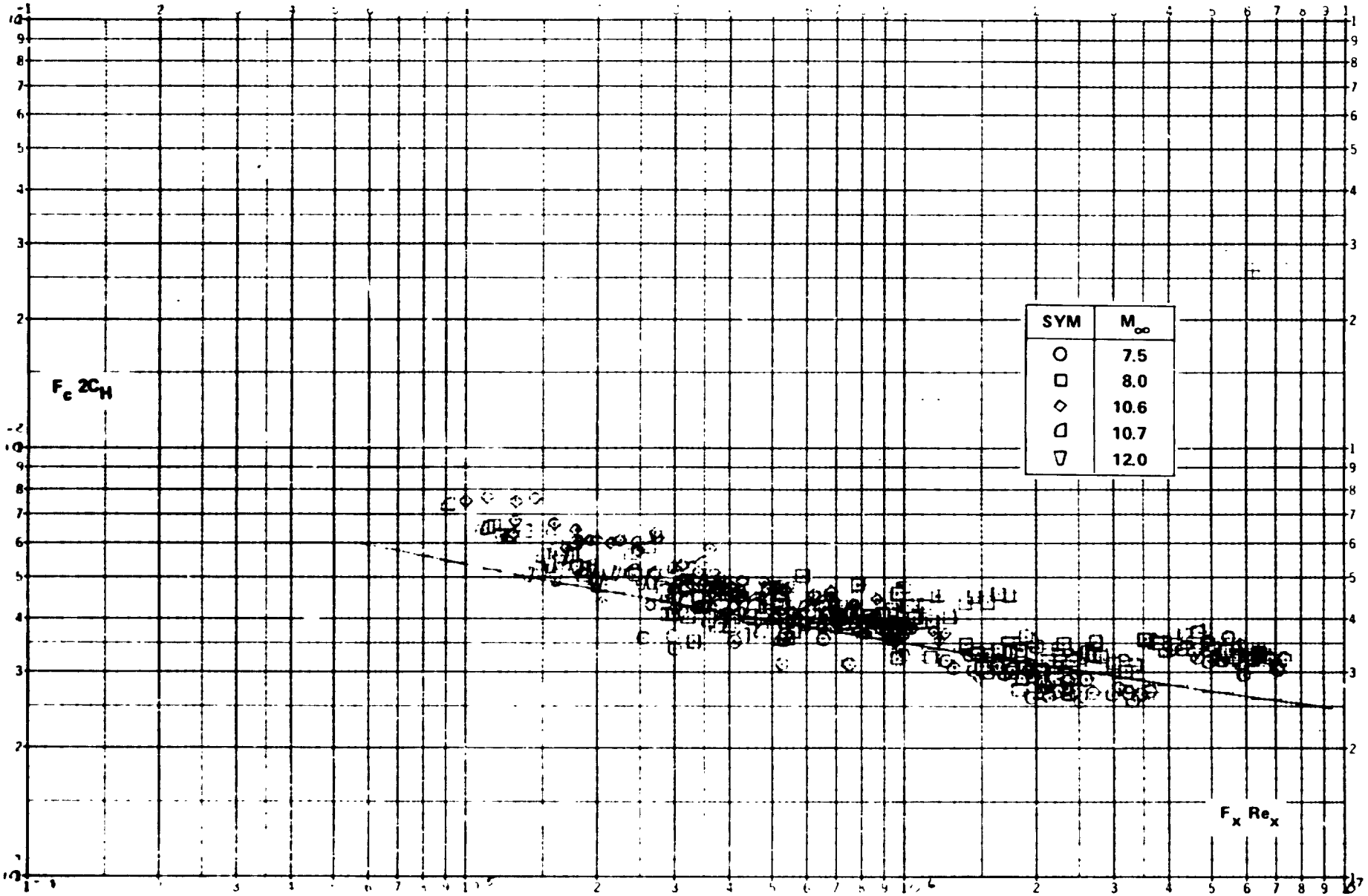

Figure 23a COMPARISON BETWEEN THE MEASURED HEAT TRANSFER AND THE THEORY OF ECKERT ($\Theta_V = \Theta_B + \Theta_{BE\ LAMINAR}$)

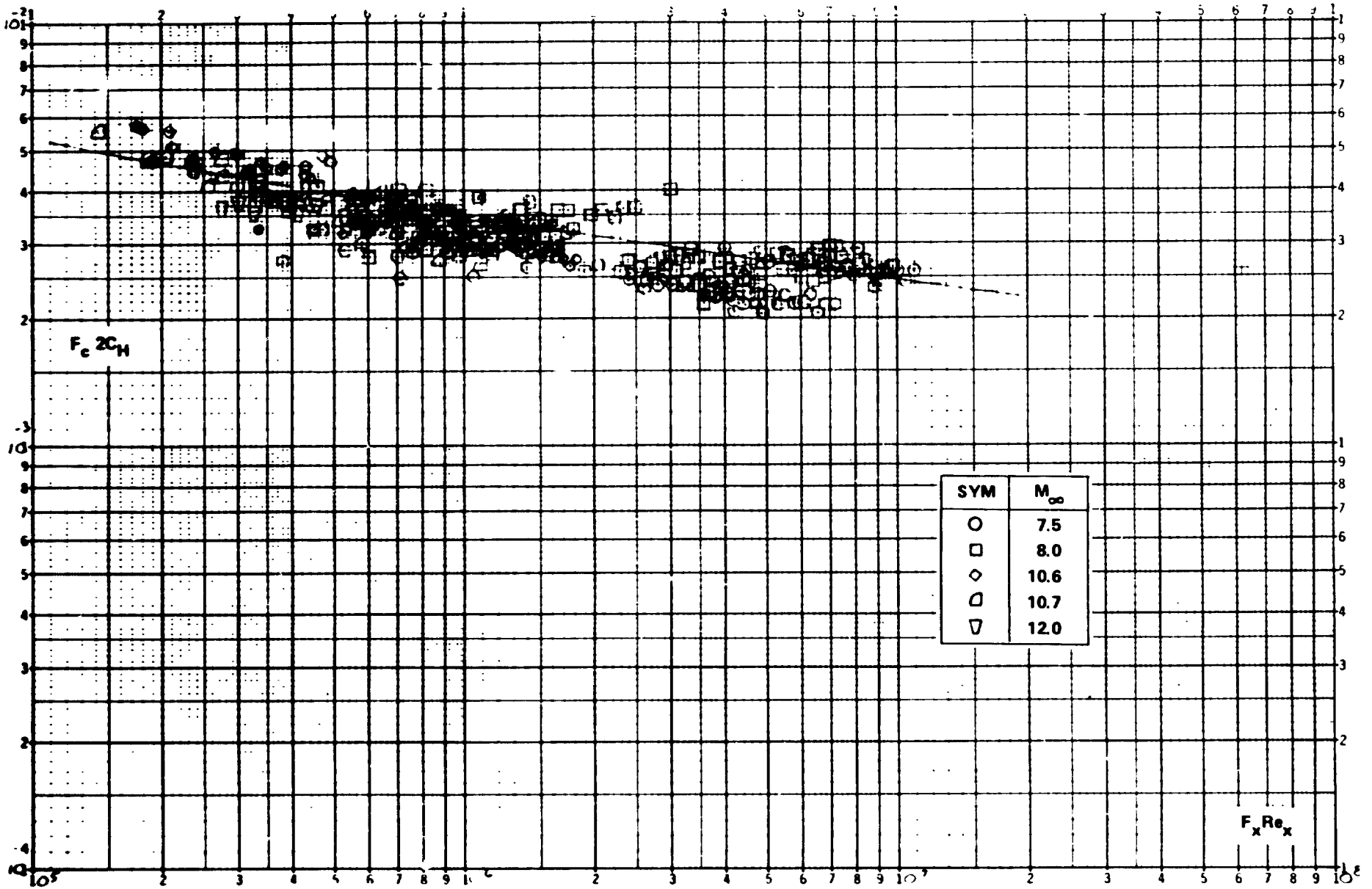

Figure 23b COMPARISON BETWEEN THE MEASURED HEAT TRANSFER AND THE THEORY OF VAN DRIEST ($\Theta_V = \Theta_B + \Theta_{BE\ LAMINAR}$)

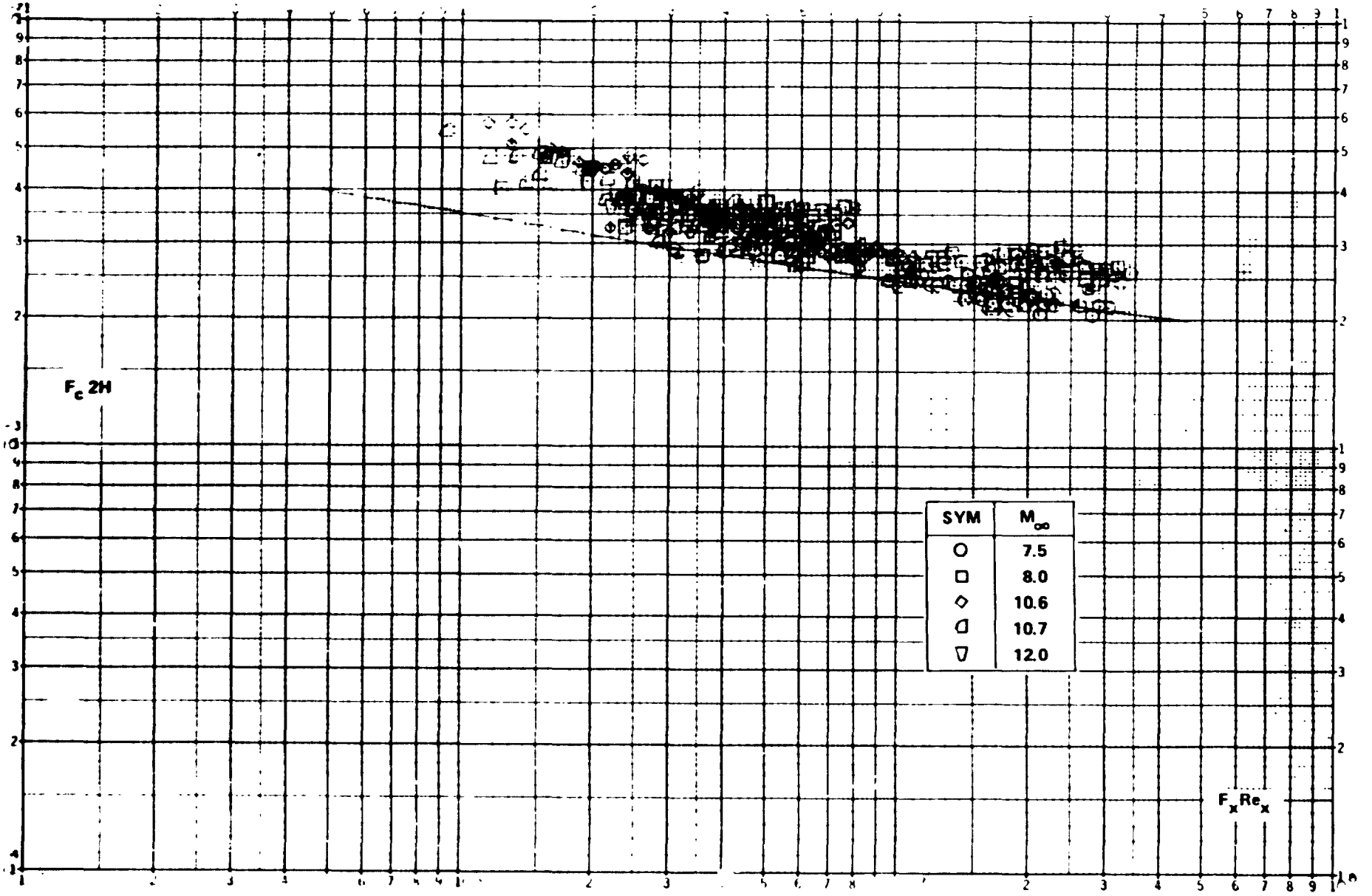

Figure 23c COMPARISON BETWEEN THE MEASURED HEAT TRANSFER AND THE SPALDING-CHI THEORY ($\theta_V = \theta_B + \theta_{BE\ LAMINAR}$)

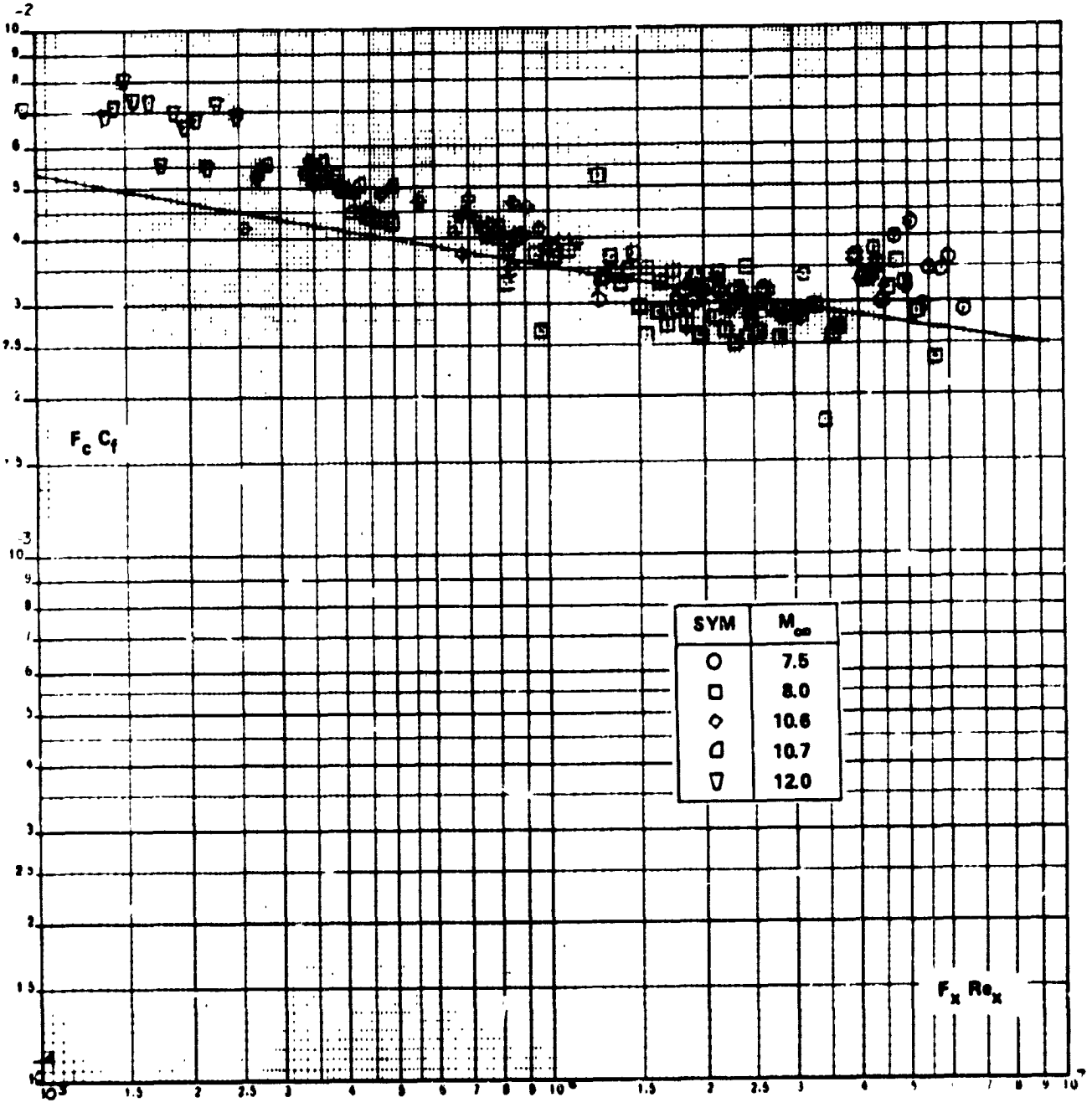

Figure 24a COMPARISON BETWEEN THE MEASURED SKIN FRICTION AND THE THEORY OF ECKERT ($\theta_V = \theta_B + \theta_{BE\ LAMINAR}$)

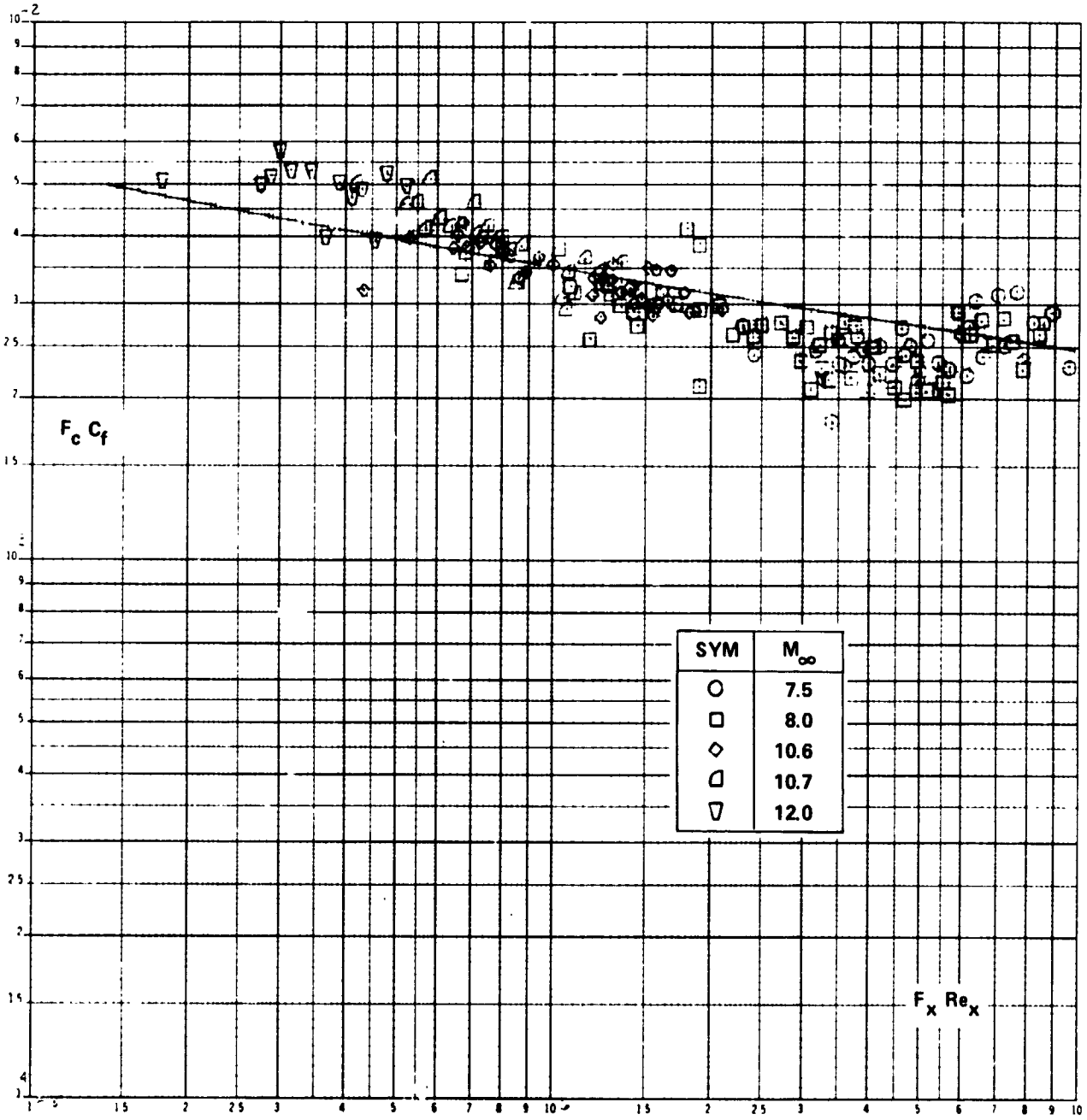

Figure 24b COMPARISON BETWEEN THE MEASURED SKIN FRICTION AND THE THEORY OF VAN DRIEST ($\Theta_V = \Theta_B + \Theta_{BE\ LAMINAR}$)

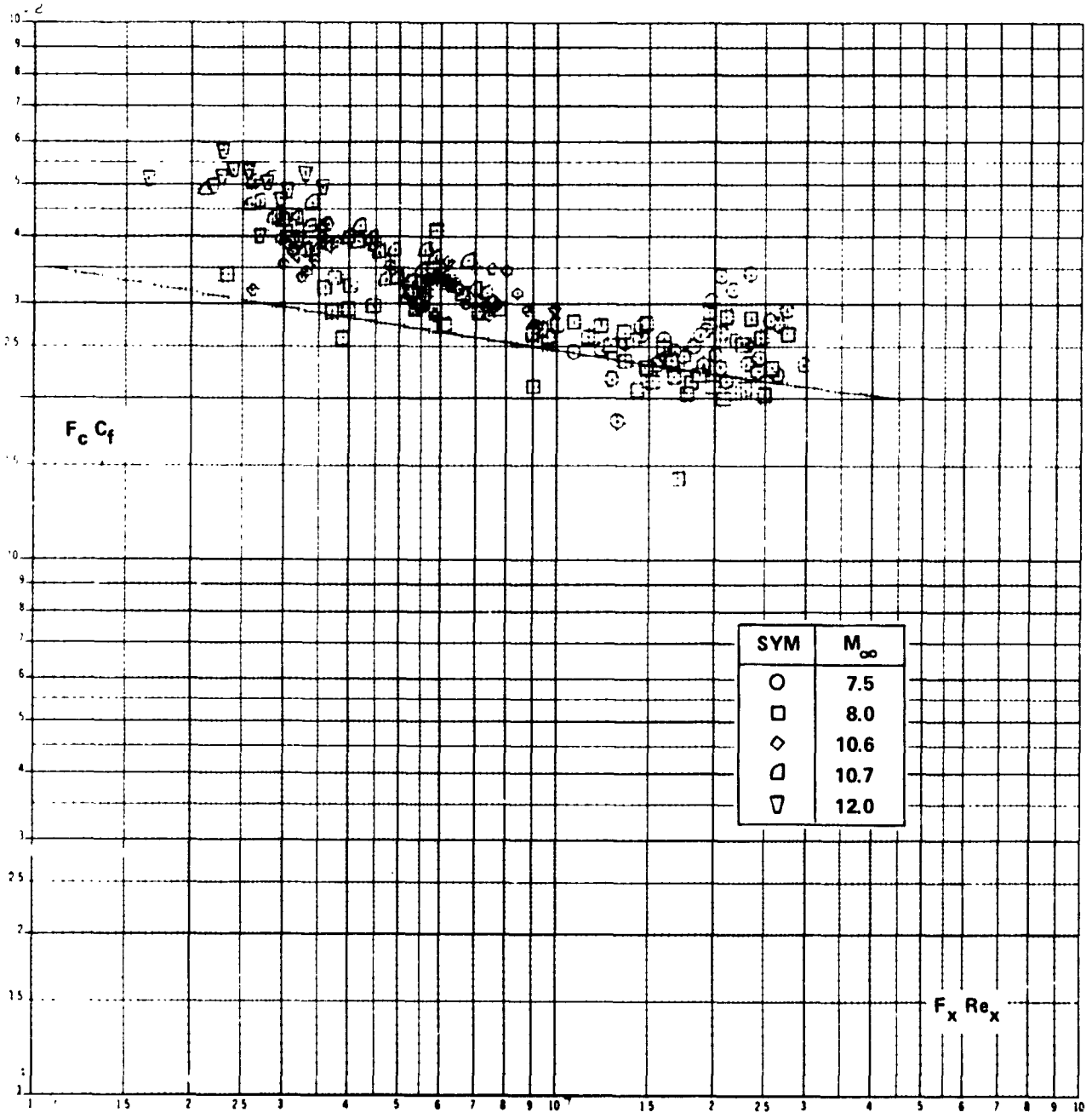

Figure 24c COMPARISON BETWEEN THE MEASURED SKIN FRICTION AND THE SPALDING-CHI THEORY ($\Theta_V = \Theta_B + \Theta_{BE\ LAMINAR}$)

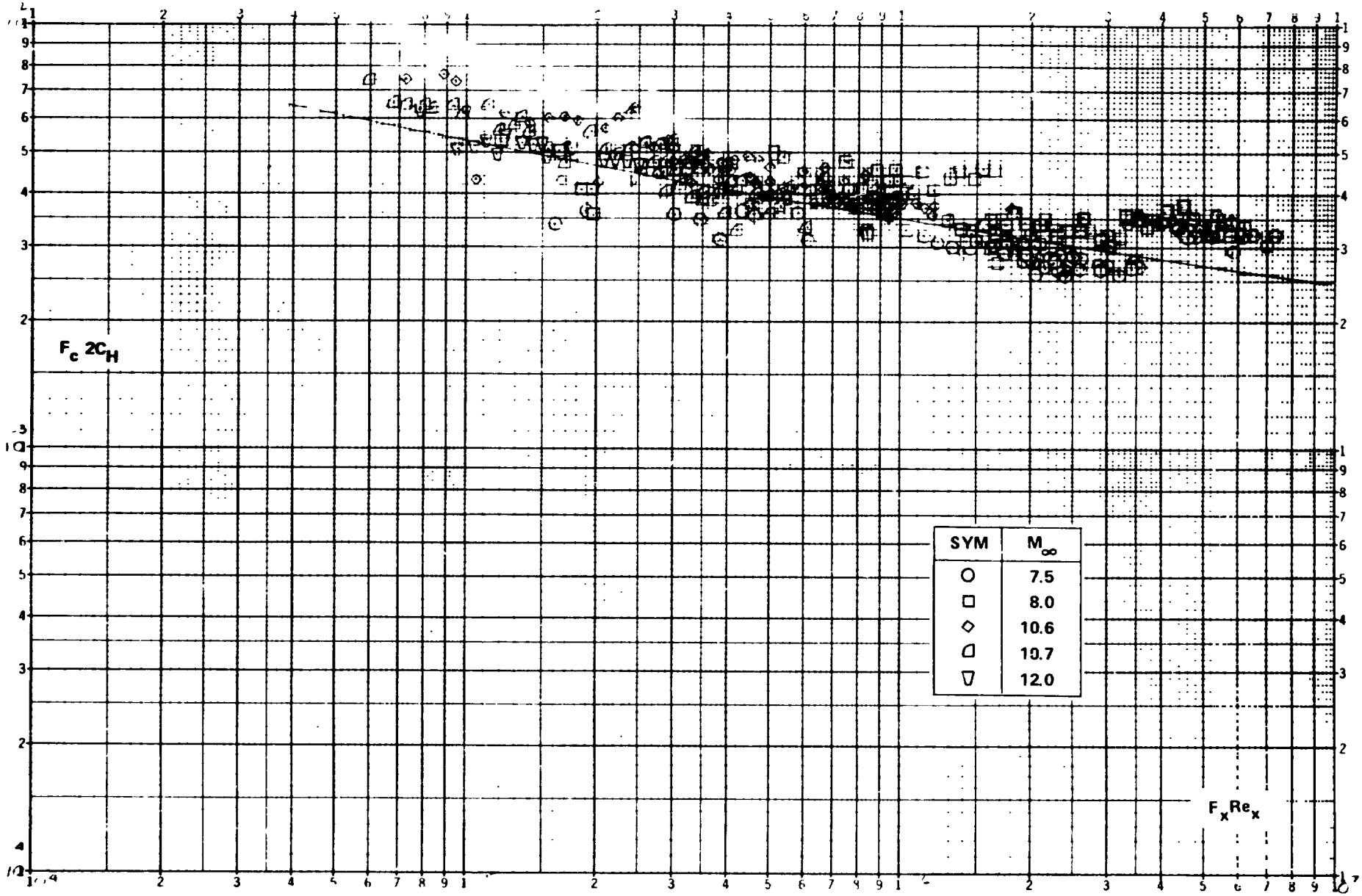

Figure 25a COMPARISON BETWEEN THE MEASURED HEAT TRANSFER AND THE THEORY OF ECKERT ($\Theta_V = \Theta_B$)

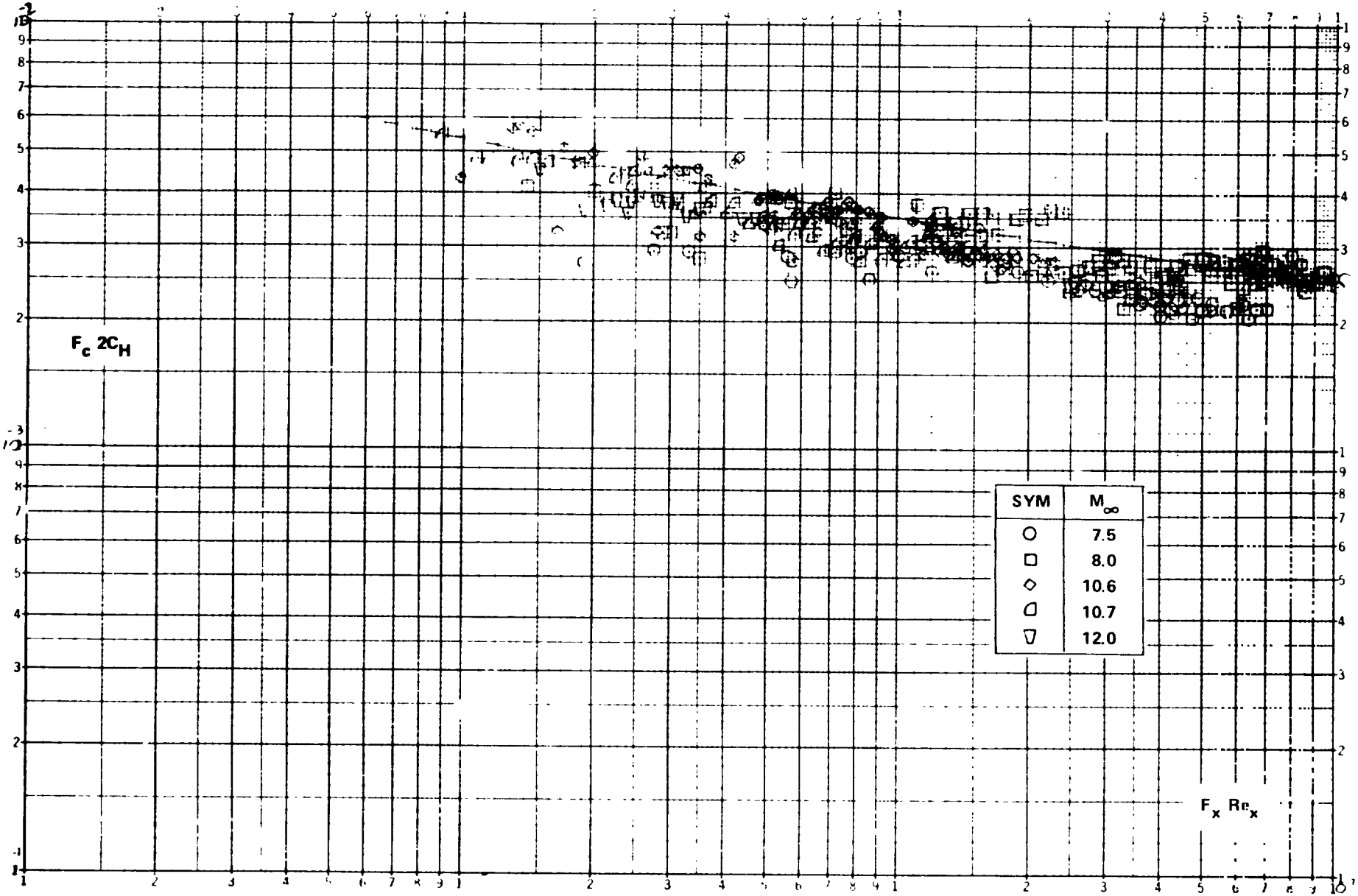

Figure 25b COMPARISON BETWEEN THE MEASURED HEAT TRANSFER AND THE THEORY OF VAN DRIEST ($\Theta_V = \Theta_B$)

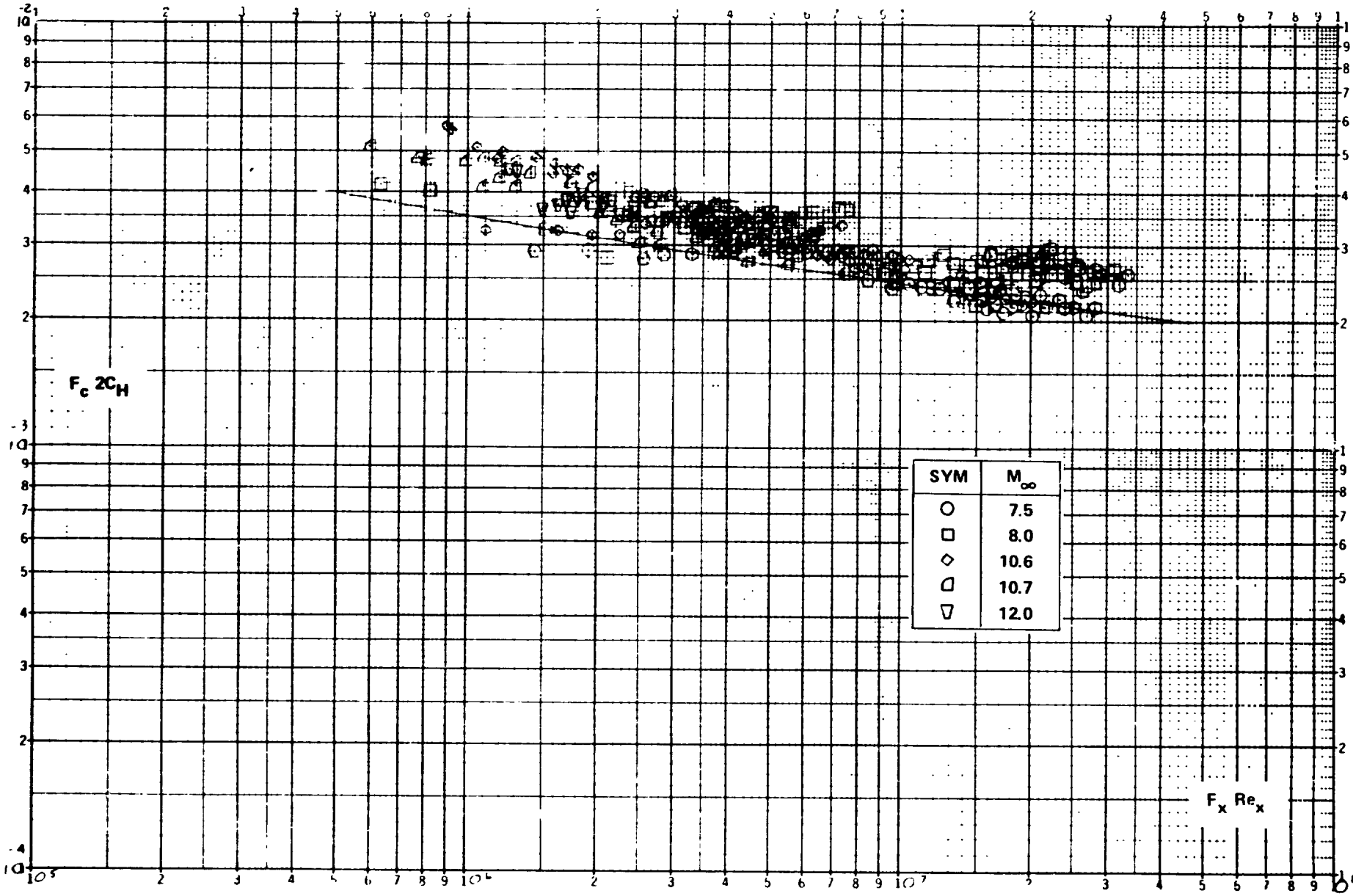

Figure 25c COMPARISON BETWEEN THE MEASURED HEAT TRANSFER AND THE SPALDING-CHI THEORY ($\theta_V = \theta_B$)

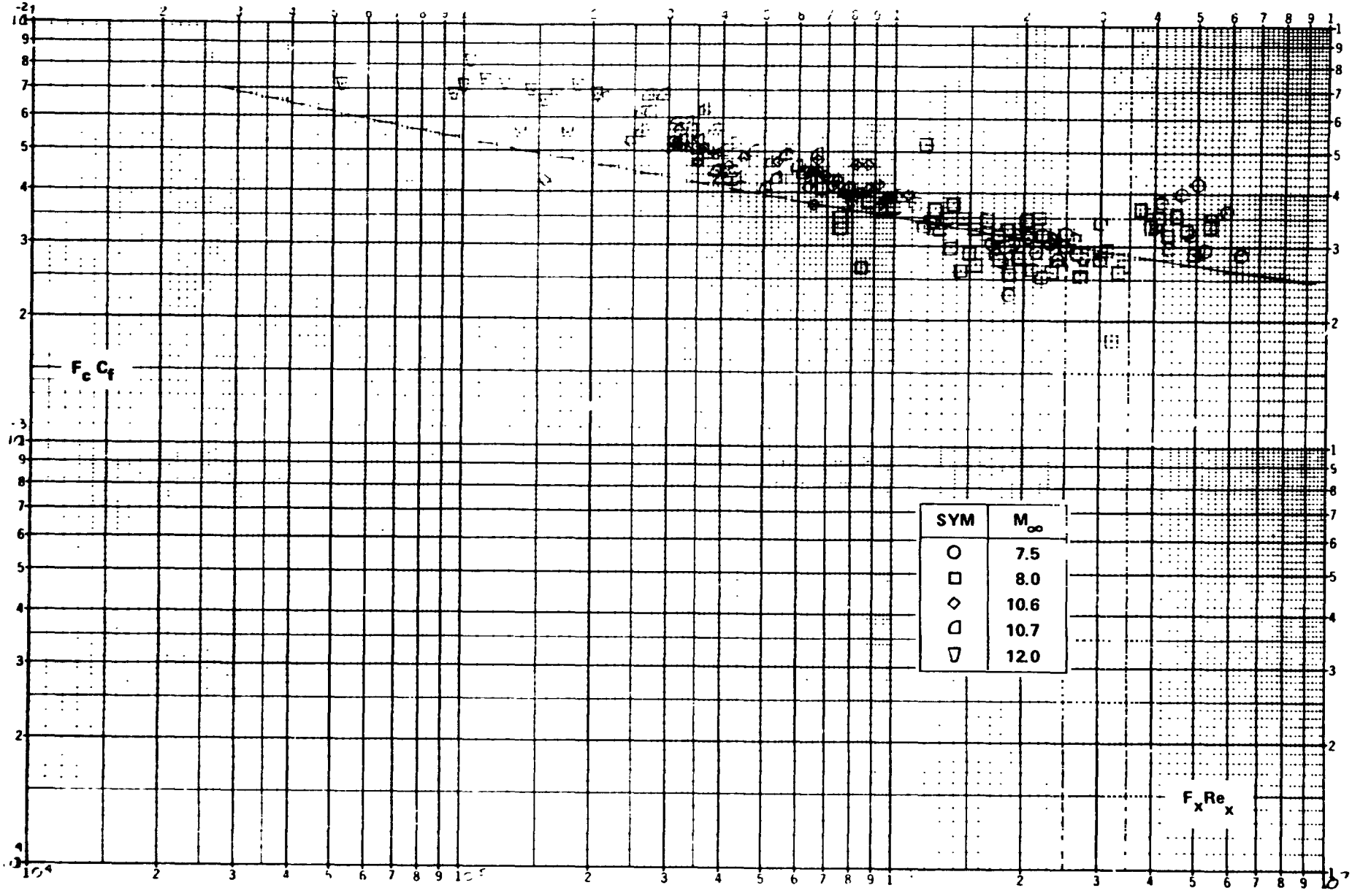

Figure 26a COMPARISON BETWEEN THE MEASURED SKIN FRICTION AND THE THEORY OF ECKERT ($\Theta_V = \Theta_B$)

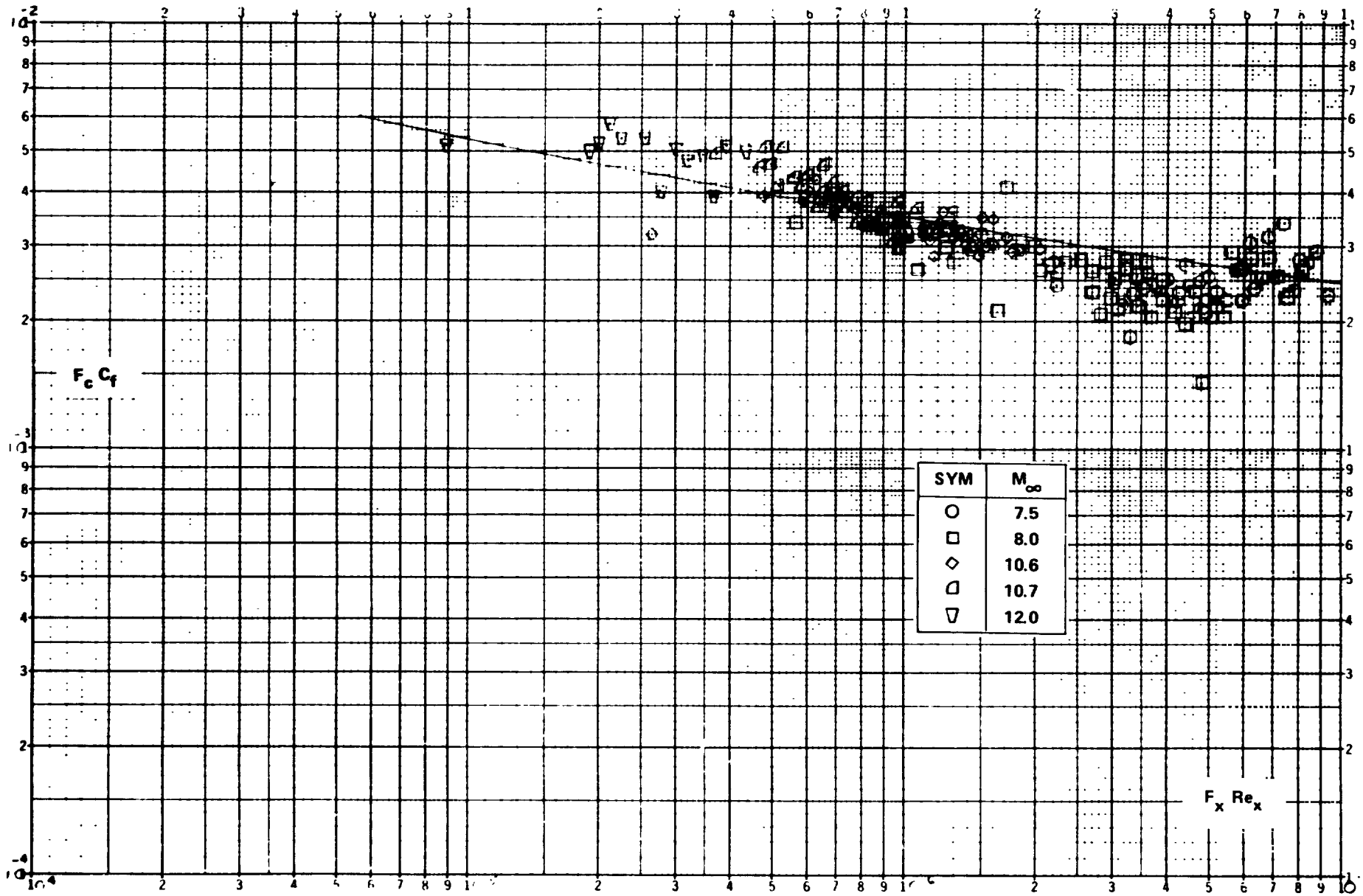

Figure 26b COMPARISON BETWEEN THE MEASURED SKIN FRICTION AND THE THEORY OF VAN DRIEST ($\Theta_V = \Theta_B$)

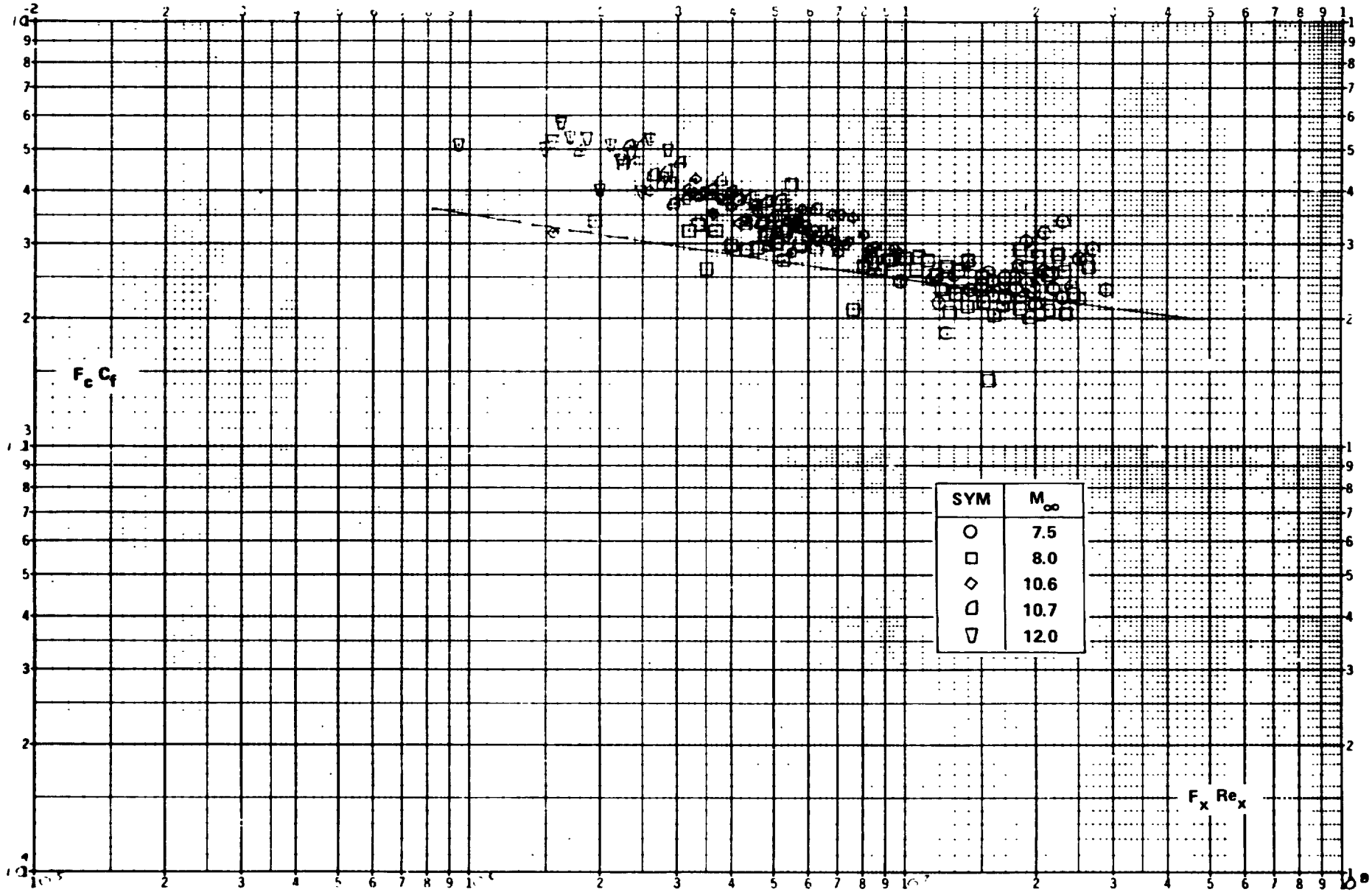

Figure 26c COMPARISON BETWEEN THE MEASURED SKIN FRICTION AND THE SPALDING-CHI THEORY ($\Theta_V = \Theta_B$)

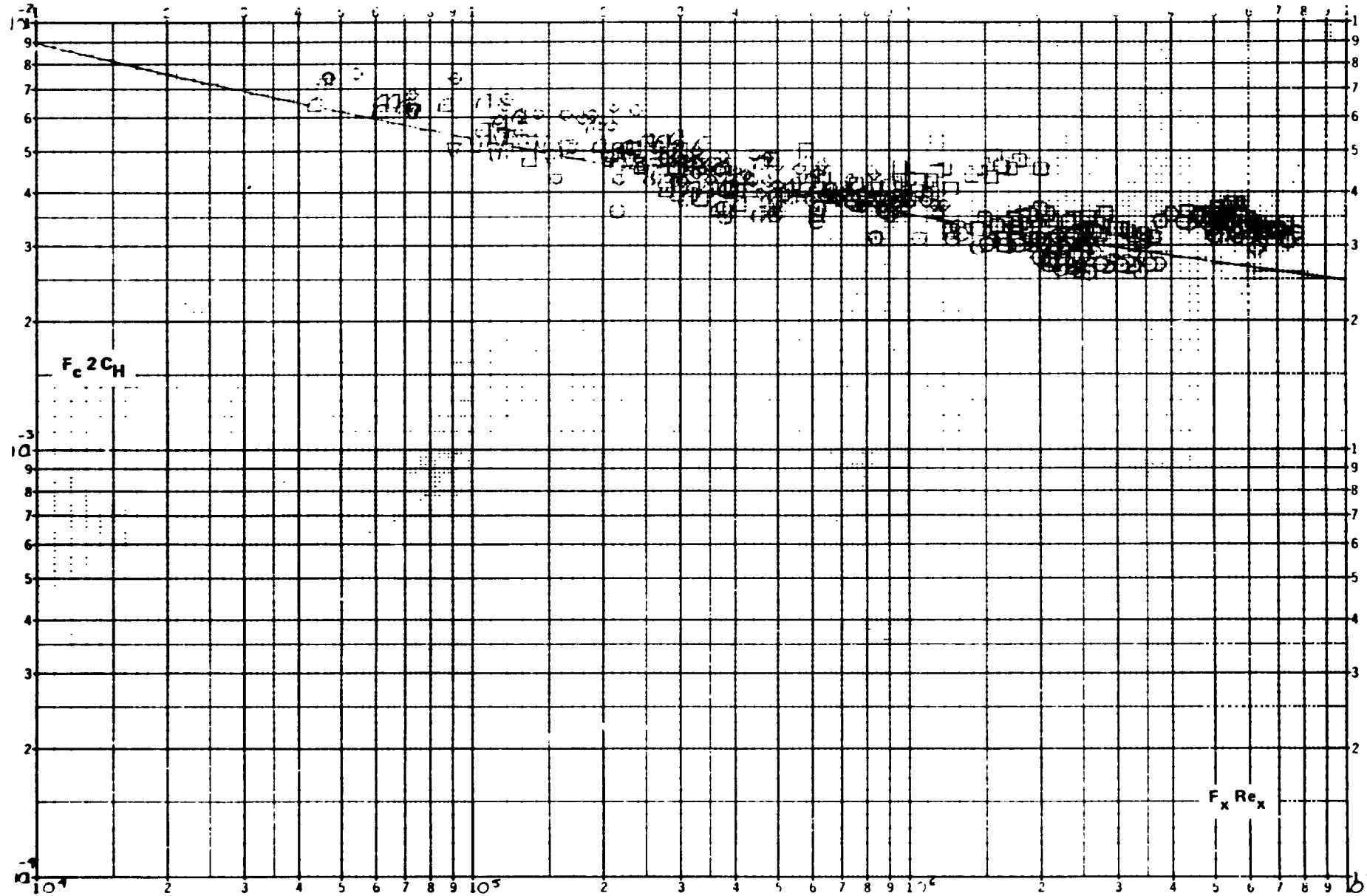

Figure 27a COMPARISON BETWEEN THE MEASURED HEAT TRANSFER AND THE THEORY OF ECKERT (X_V = 0 AT $\Theta_B + \Theta_{BE/2}$)

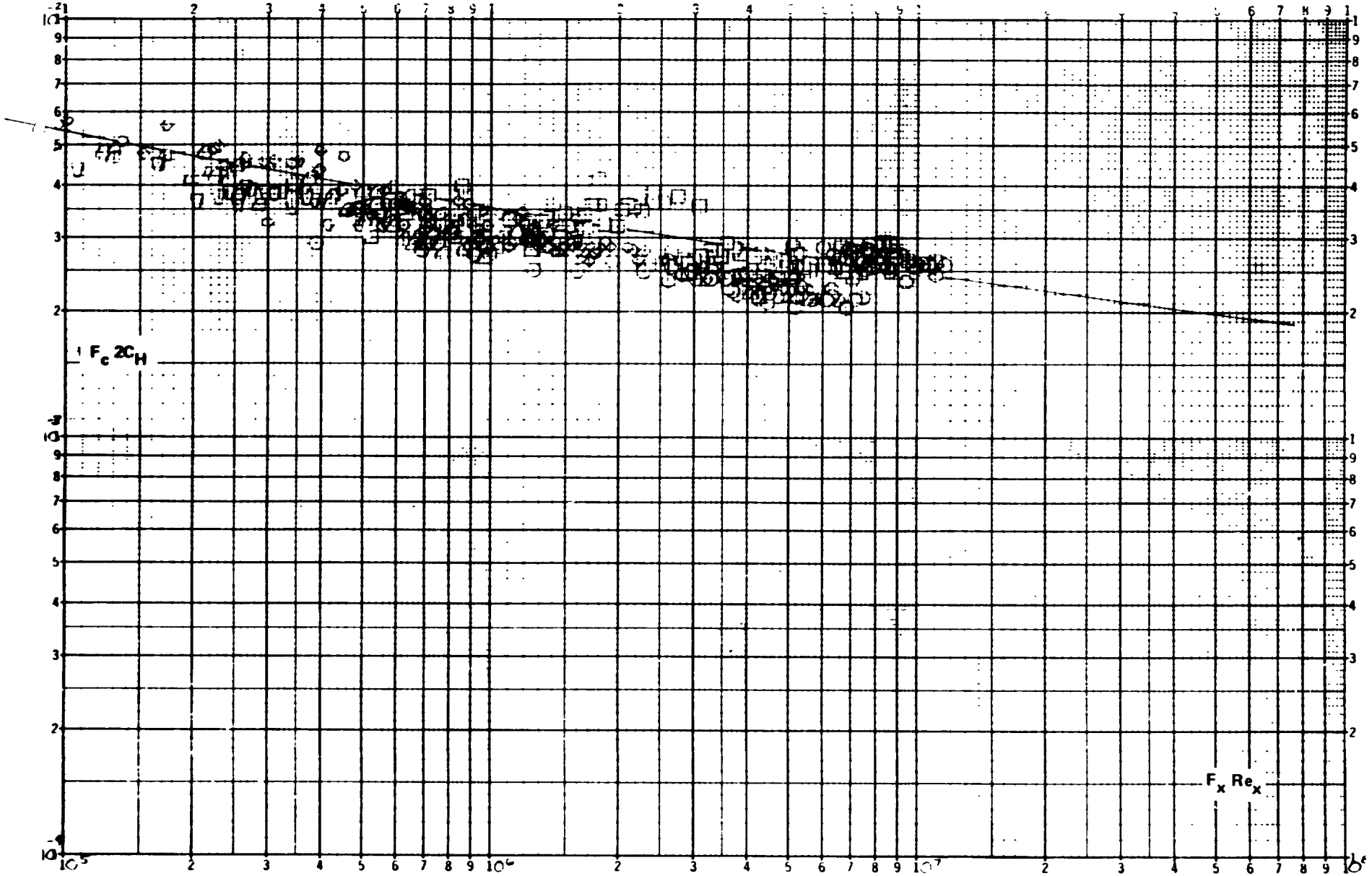

Figure 27b COMPARISON BETWEEN THE MEASURED HEAT TRANSFER AND THE THEORY OF VAN DRIEST ($X_V = 0$ AT $\Theta_B + \Theta_{BE/2}$)

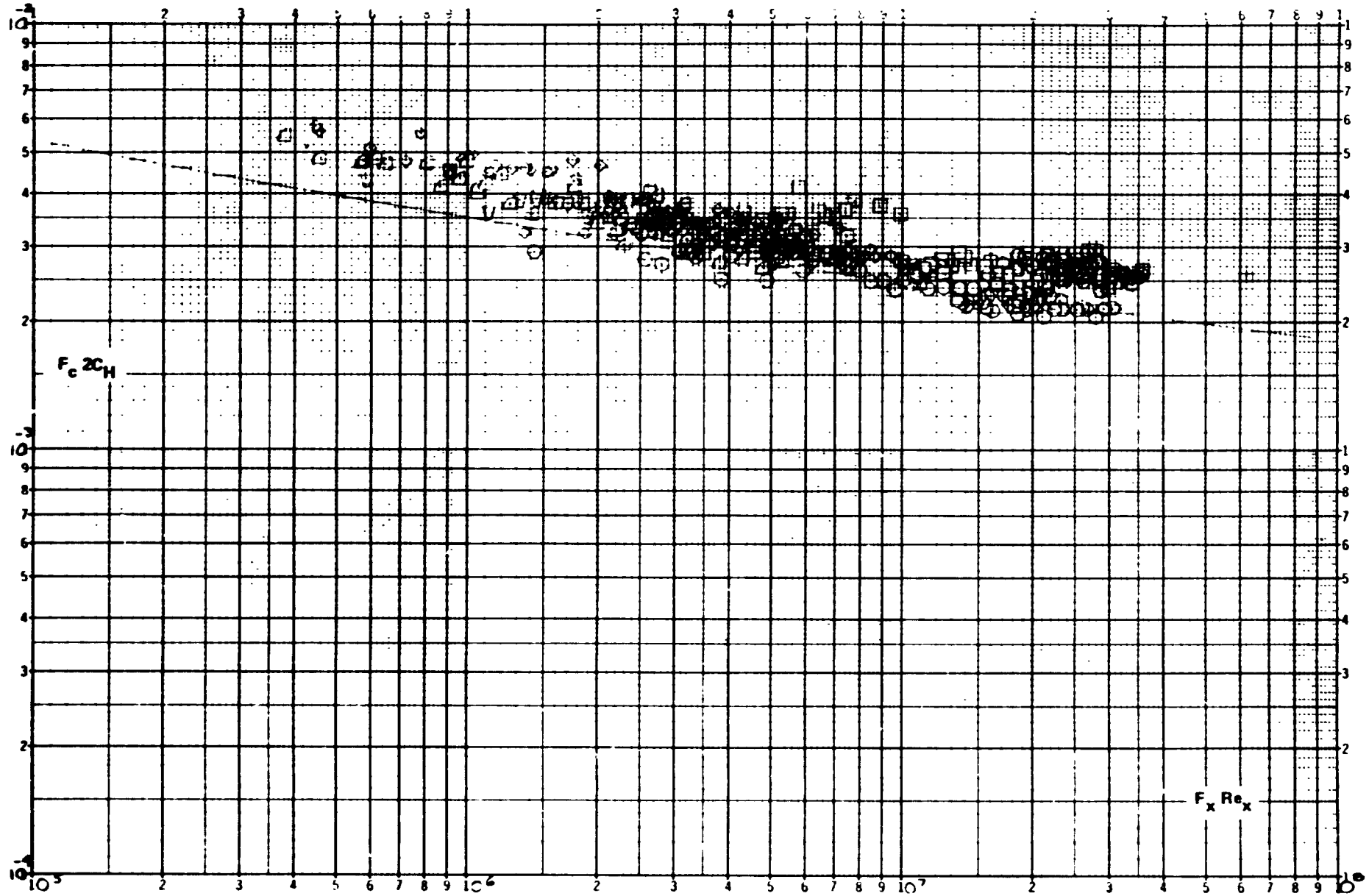

Figure 27c COMPARISON BETWEEN THE MEASURED HEAT TRANSFER AND THE THEORY OF SPAULDING-CHI (X_V = 0 AT $\Theta_B + \Theta_{BE/2}$)

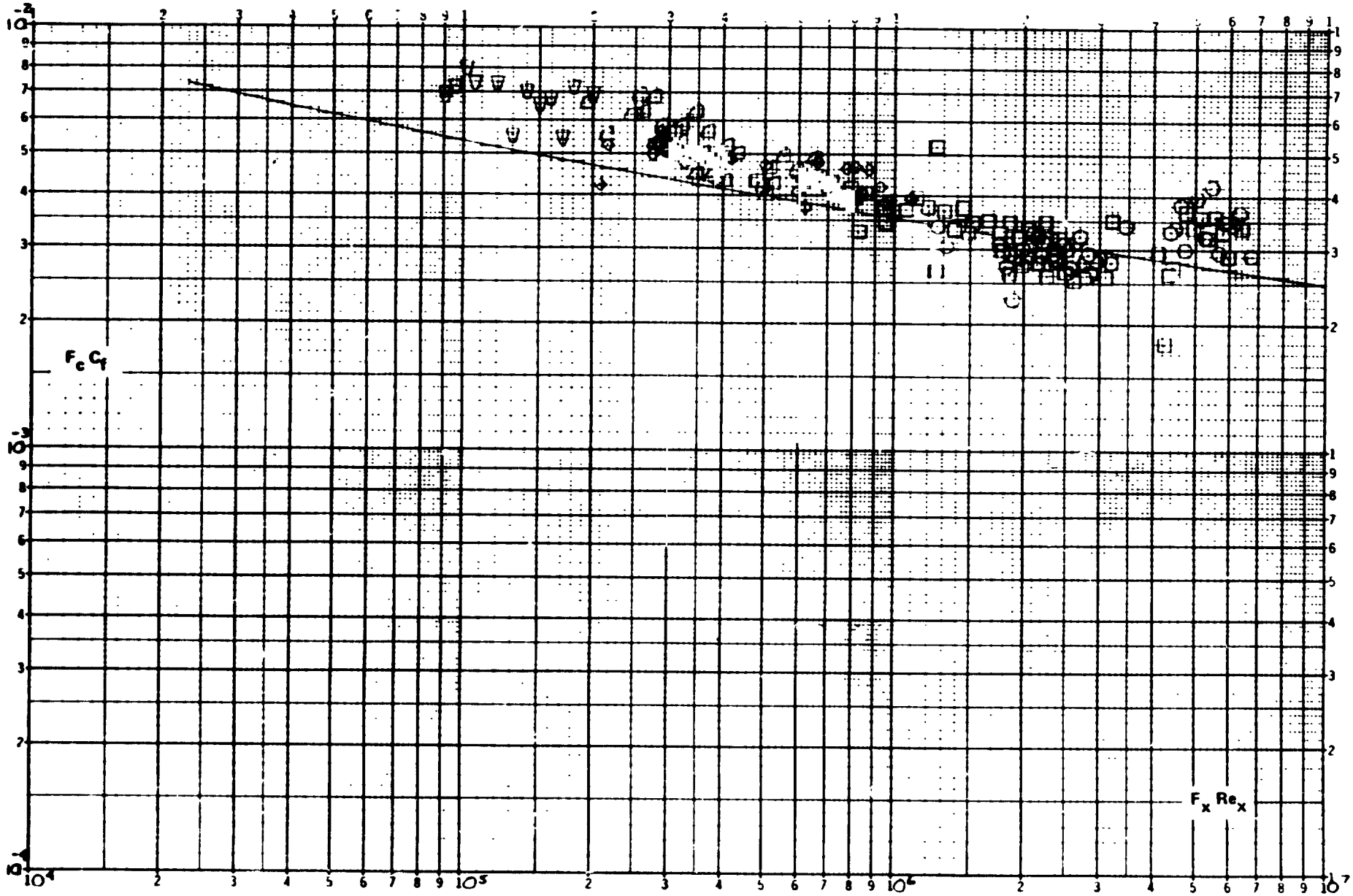

Figure 28a COMPARISON BETWEEN THE MEASURED SKIN FRICTION AND THE THEORY OF ECKERT ($X_V = 0$ AT $\Theta_B + \Theta_{BE/2}$)

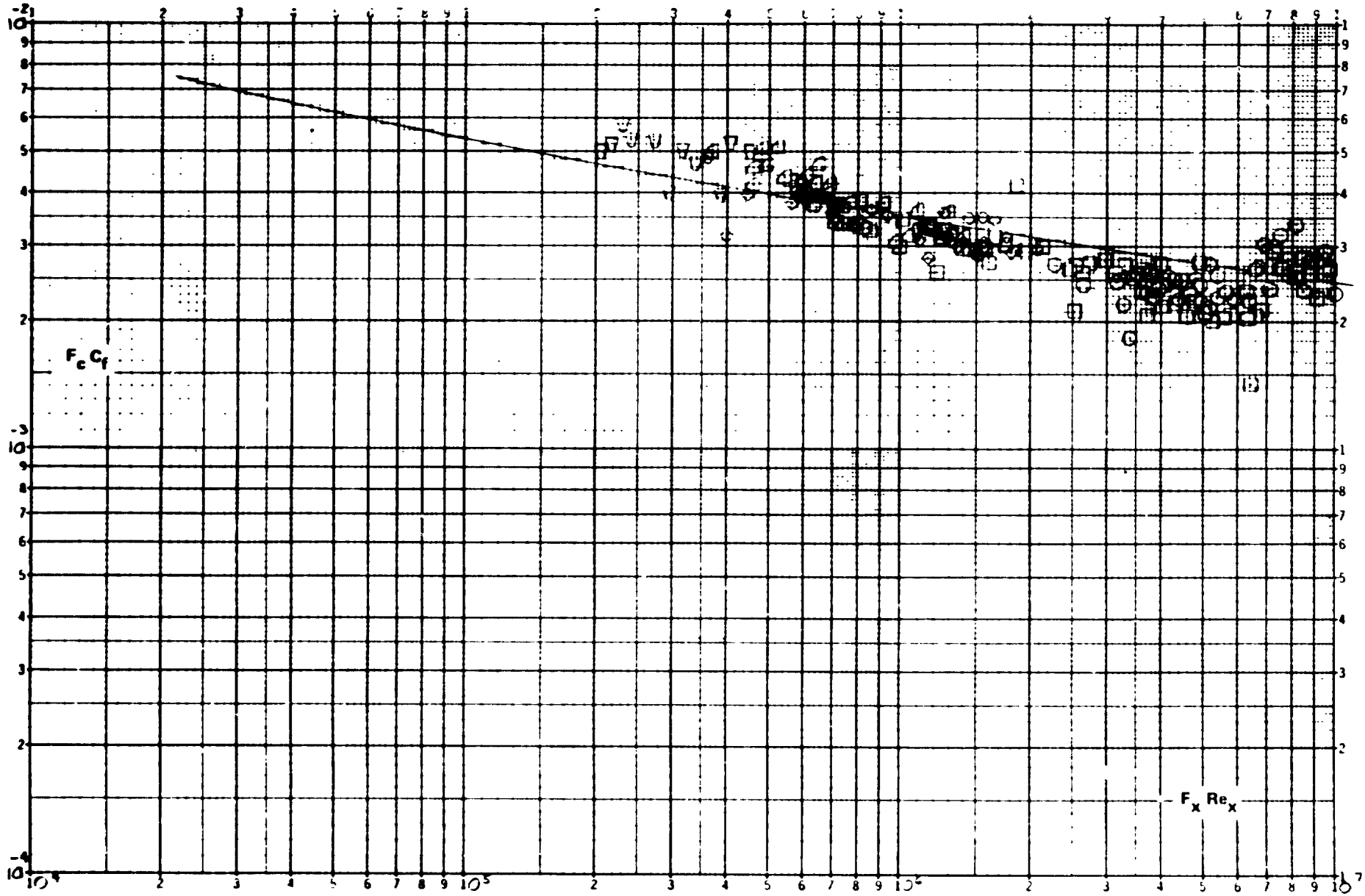

Figure 28b COMPARISON BETWEEN THE MEASURED SKIN FRICTION AND THE THEORY OF VAN DRIEST ($X_V = 0$ AT $\Theta_B + \Theta_{BE/2}$)

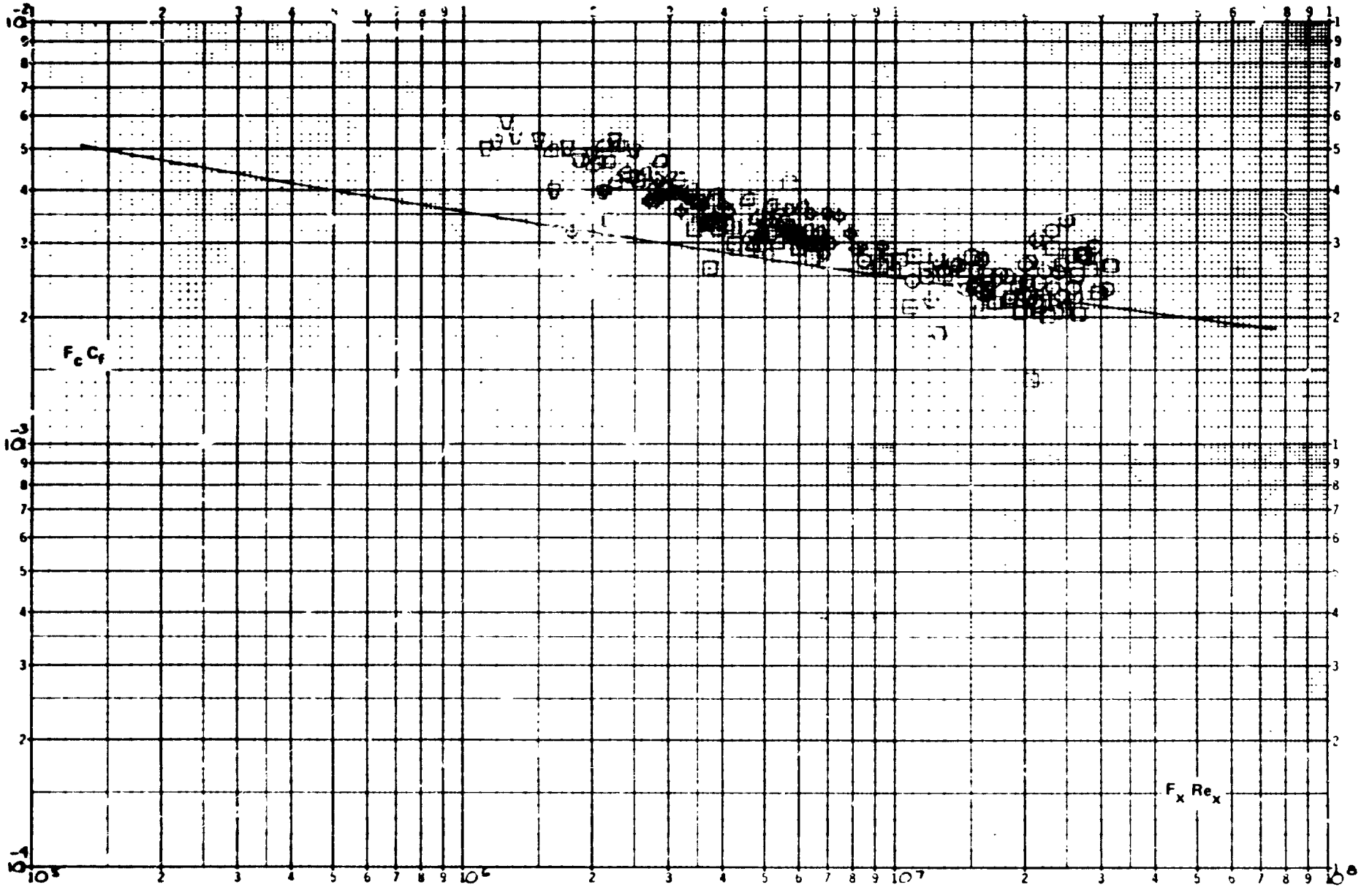

Figure 28c COMPARISON BETWEEN THE MEASURED SKIN FRICTION AND THE THEORY OF SPAULDING-CHI (X_V = 0 AT $\theta_B + \theta_{BE/2}$)